Imaging Fines Migration Induced by Salinity Changes

YU EMMA HARASAWA

Imaging Fines Migration Induced by Salinity Changes

Yu Emma Harasawa

Supervisor: Prof Chris H. Greenwell

Dr Tim Hawkins

Dr Ian R Collins

Durham University

Department of Earth Sciences

Master by Research Thesis

2020

Abstract

This project aims at confirming positive LS-EOR (low salinity enhanced oil recovery) effects with fluorescent microscopy, an unprecedented approach. The fluorescent microscopy employed in this project used a confocal microscope and total internal reflection fluorescence (TIRF); these allowed the acquisition of 3D images using a non-destructive procedure.

For the first part of the project, confocal microscopy was utilised to test the average fluorescent intensity and the scope of 8 different types of clay minerals. Comparing fluorescent features of high and low defect kaolinite, also 3 types of LDH Mg/Al and another 3 types of LDH Mg/Fe were included in this study. Moreover, SEM was applied to analyse the structure of clay minerals, and XRD was applied to determine the impurities within the clay samples. The sample which determined that clay minerals fluoresce on a consistent basis were aged with formation brine and either polar crude oil or non-polar crude oil, these aged clay samples were utilised for the second part of the project, which was aimed at observing any movement of clay by lowering the salinity. AFM and TIRF were employed for the latter section. Based upon the attained results, the following is notable: firstly, that the presence of iron in clay minerals diminishes the fluorescent intensity, also high defect clay minerals do not exhibit a steady fluorescence intensity. Secondly, testing with SEM and XRD revealed that KGa-1b might be the only clay sample that has the potential of autofluorescence, since the percentage of fluoresced pixels was more than the percentage of impure minerals that would fluoresce at the applied wavelength. Finally, AFM and TIRF confirmed LS-EOR effects even without the presence of polar components in the system, especially after fourfold dilution from the initial ionic concentration caused the clay minerals to move more vigorously; significant clay swelling at the salinity level was also witnessed. In summary, the novel approach of TIRF is deemed well suited in terms of its technique for the study of fines migration. Four-fold dilution of high salinity brine initiated clay swelling and dispersion, still salinity higher than generally accepted as the LS-EOR optimal salinity level was given. It can be interpreted that fines dispersion and migration could be initiated at a higher salinity, while the emulsion phase form and the oil molecule surface release may require a much lower ionic concentration in order to enable residual oil recovery. LS-EOR effects observed under the TIRF and AFM, arising due to the weaker electrostatic forces developed by lowering the system's salinity hence, the generally accepted importance of polar oil components for LS-EOR effects does not hold in these experiments. Positive LS-EOR effects revealed by TIRF, AFM, and FFM consequently concluded that electrical double layer expansion would be the most dominant attribution for LS-EOR.

Acknowledgements

This project would not have been made possible without a myriad of people's support. First of all, I owe my deepest gratitude to Prof. Chris Greenwell for his unwavering support and advice. He has provided to me numerous opportunities throughout this year such as the autonomy as a developing geoscientist whilst at the same time; keeping me humble as a student working under his tutelage. Such examples include: being accepted at a workshop in Germany, and being given an opportunity to go to Cambridge University to participate in a meeting with British Petroleum (BP). Furthermore, he always allowed me to try new experiments or have access to new instruments/equipment, every time I come up with new ideas. I sincerely feel that how has taught me has allowed me to continuously flourish and self-motivate myself to continue which enabled me to learn new things in a short time, this was especially valuable during the corona virus pandemic where self-motivation was a necessary skill.

I would also like to express my gratitude to BP, who as a pioneer of low salinity EOR inspired me to research this project topic, as well as substantially financially supported my laboratory fees. The experience of undertaking the project with BP as a pioneer in this field of science was a huge advantage for me especially as I would soon discover that I would start work for a petroleum exploration company the following the year in Japan. In terms of recognising the scale and type of possibly world-renown projects I maybe working on.

I also extend sincere thanks to all the staff who supported me through my project who I attribute to its success. I am thankful to Prof Jon Gluyas for discussions with me about my research topic and introducing me to the most appropriate professor who would go on help me throughout the remainder of my research project (Prof. Chris Greenwell). In addition, I extend considerable thanks to Prof Andrew Aplin for discussions with me about my research topic as well as preparing for me and recommending me via recommendation letters which allowed me to apply for this master's course, every time I applied for workshops. I would also like to thank Mr Leon Bowen for SEM training and for his support with image processing. I thank Mr Ian Chaplin for creating delicate SEM samples. I thank also Dr Catriona Menzies for being my first reviewer and always encouraging me and giving me meaningful feedback on my progression reports. I thank Dr Julie Prytulak for being my second reviewer and giving me regular support and advice. I also thank Dr Tim Hawkins and Miss Joanne Louise Robson for their confocal microscopy training and for supporting me by providing image processing training. I would also like to extend an extra thank you to Mr Miro Cafolla and Dr Kislon Voitchovsky for their valuable AFM image processing

with proved especially beneficial at a time when their expertise helped me in my research project a great deal.

I also greatly appreciate all my colleagues; Catriona Sellick, Nikolaos Apeiranthitis, Daud Mohammad Hamidi, Christos Vasilopanagos, Ashleigh Cheung, Hector Eduardo Escamilla Garcia, and Mingliang Liang. I had the pleasure of sharing the same working environment with these PhD students. We all had this seemingly perfect opportunity of sharing ideas and learning new concepts and in the field of science. it was as though we were venturing into an even higher level of scientific excellence and discovery together; and I am glad to have had the opportunity and honour to have undergone this journey with all my esteemed colleagues.

Finally, I would like to give special thanks to my parents and to my grandmother who provided me with the opportunity to study overseas. This project would not have even begun without the support from my family.

I have been studying geology throughout my undergraduate studies and I continue to do so to this present day, the knowledge which I have acquired for this project was completely different from that which I first learned during my undergraduate course; thus, I must admit I did experience a fair amount of struggles at the outset. In addition to that, the project was massively impacted by COVID-19, due to the approximate four month lockdown which was imposed here in the United Kingdom. Therefore completion of my proposed project came under a lot pressure due to missed deadlines and changed experiments and other unexpected delays which the COVID-19 pandemic brought about. It was only by virtue of everyone's support that my project was able to be completed successfully.

Thank you.

Table of Contents

Chapter 1 Introduction

1.1 Why Enhanced Oil Recovery is Used

Our society today is understandably concerned with environmental damage arising from climate change. This is caused by the use of extracted petroleum which is utilised for not only fuel but also daily necessities include ink, eyeglasses, telephones, and more (Chisholm, 2015). However, the increase in total energy and fossil fuel demand, when considering the current trajectory, are both set to continue growing each year, while oil reserves and discoveries have been declining (Alvarado and Manrique, 2010). Although renewable energy is the fastest-growing primary energy source and expectations of the ability of renewable energy to resolve environmental issues are very high; it's calculated that by 2040 only 15% of total energy demand will be satisfied under this category, thus the eventual uptake is hard to predict, as shown in Figure 1.1 (BP Energy Outlook 2019 edition, 2019). In addition, the energy industry will still encounter issues with completely phasing out fossil hydrocarbons, due to the fact that carbon-based materials and lubricants cannot be immediately replaced by renewable alternatives. To support the global energy demand and to sustain production of those carbon- based materials and lubricants, yet reduce exploration for new oilfields, scientists and the oil industry are required to develop new exploration and production (E&P) techniques. Enhanced oil recovery (EOR) technologies will play a key role in supporting the future energy and material needs of society, especially in light of the fact that applying EOR technology to the production of additional oil is presently considered more efficient than finding and drilling for further new oil fields, as well as aligning with the "social licence to operated" of oil companies (Al-Mjeni *et al*., 2011; Oxy.com. 2020).

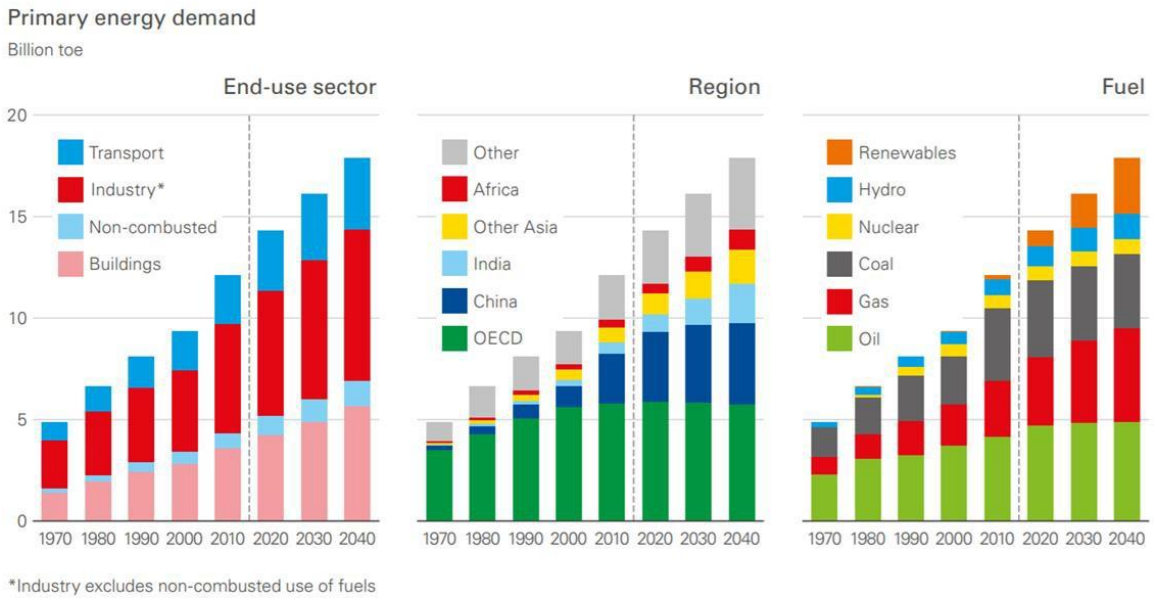

Figure 1.1: Energy transition from 1970 to 2040 in end-use sectors, regions, and fuels; (End-use sector) the industry and buildings require more than 70% of total energy demand by 2040, although energy consumption for transportation is more noticeable in daily life. (Region) The Organisation for Economic Co- operation and Development (OECD), also known as 'developed countries club' (Economic and Social Research Institute (ESRI), Cabinet Office, Government of Japan, 2006), requires 30% of total energy demand in 2040. However OECD's energy demand rose to a steady consistent level since the year 2000. In contrast, energy demand for those developing counties is gradually increasing every year. (Fuel) needs of renewable energy will only account for 15% of total energy demands in 2040 whereas the demand of fossil fuels is predicted to continue to rise and 50% of energy demand in 2040 may still require fossil fuel energy (oil and gas) Taken from (BP Energy Outlook 2019 edition, 2019).

1.2 Stages of Oil Recovery and Types of Enhanced Oil Recovery

There are three main stages in use to recover petroleum hydrocarbons, as shown in Figure 1.2. Originally, the term 'EOR' referred only to tertiary recovery which the third stage of the additional hydrocarbon extraction process followed after primary and secondary recovery processes (tertiary recovery – Schlumberger Oilfield Glossary, 2021) and further details are documented at '1.2.3 Tertiary Recovery'. Improved oil recovery (IOR) denoted both secondary and tertiary recovery (Stosur *et al*., 2003). However, some authors, such as Cockcroft *et al*. (1988), use 'EOR' in a broader sense, for a set of methods that may be deployed during secondary or tertiary phases of reservoir production.

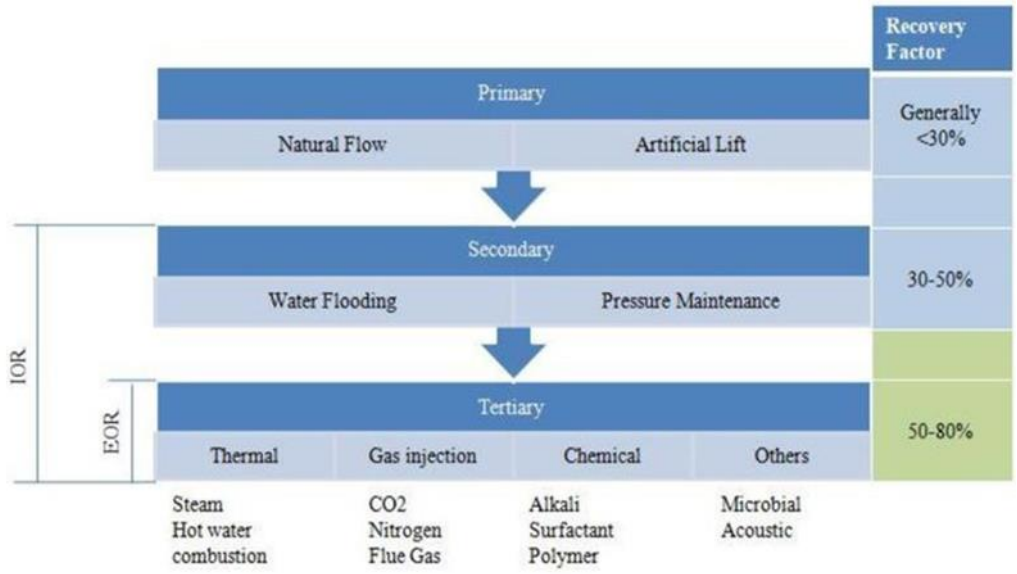

Figure 1.2: Differences between primary, secondary, and tertiary recoveries (taken from Patel *et al*., 2018). Less than 30% of the total hydrocarbons in reservoirs may be obtained without applying any IOR procedures. This secondary recovery process is used to extract an additional < 20% of hydrocarbons (for a maximum of 50% of the total oil recovery). The tertiary recovery process increases by an additional < 30% of oil recovery (maximum of up to 80% of the total oil in place recovered). Hydrocarbons are unlikely to extract more than 80% by applying any recovery procedures.

1.2.1 Primary Recovery

The primary recovery phase of oil production depends on the natural pressure gradient of the reservoir itself (Stosur *et al*., 2003). Therefore, injection of other fluids to maintain a pressure gradient is not required in this step. The primary mechanism of recovery is the expansion of reservoir fluids, such as oil, water, and gas, once a pressure drop is introduced through breaching the reservoir seal.

1.2.2 Secondary Recovery

Secondary recovery is applied when the flow energy from primary recovery is depleted or insufficient for economic oil recovery, as the higher pressure in the reservoir equilibrates with the atmosphere (Stosur *et al*., 2003). This phase of recovery involves injecting either water or gas to re-pressurise the system:

Water flood recovery. Water is injected below the oil leg (Figure 1.3),, within the oil leg, or in limited circumstances into the gas cap (this latter option is very rare) to maintain pressure.

Gas injection recovery. Gas is injected into the gas cap, the top of the reservoir, or down-dip in the oil leg so as to maintain pressure. The most commonly injected gas is methane, but CO_2 is likely to become increasingly common.

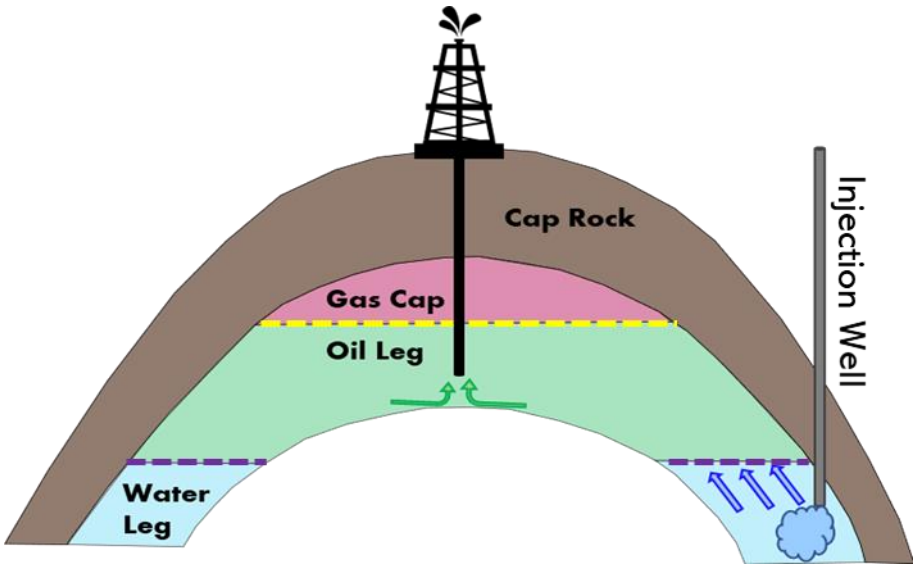

Figure 1.3: The figure is evidence of schematic properties which the typical petroleum reservoir possesses as adopted from Aminzadeh and Dasgupta (2013). Due to the differences in density which cause groundwater, oil, and gas respectively to accumulate; the lighter gas is placed near the surface and the groundwater is located in a deeper section of the reservoir (Marshak, 2007). The diagram also depicts the waterflood recovery mechanism, which requires injecting water below the oil leg. The boundary between gas cap and oil leg is known as Gas/Oil contact (GOC), whereas the boundary between oil leg and water leg is known as Oil/Water contact (OWC) ((Dennis *et al*., 2000; Mjaavatten *et al*., 2008; Aminzadeh and Dasgupta, 2013).

Both mechanisms involve sweeping the oil from the injecting well of the introduced fluid towards the primary phase production wells. The application of secondary recovery methods are relatively inexpensive and straightforward, however there are some fundamental limits. Such limits include the retentive effects of the capillary forces in the reservoir, which result in unrecoverable or residual oil saturation. Tertiary recovery helps overcome this issue by taking into consideration the miscible and chemical that would reduce or eliminate capillary forces between oil and those injectant, as well as the application of heat which would reduce viscosity of oil to achieve high in oil recovery. (Cockcroft *et al*., 1988).

1.2.3 Tertiary Recovery

The significant difference of tertiary recovery compared to primary and secondary recovery, is that tertiary recovery alters the oil properties, or the mass transfer between the injected fluid and the reservoir oil through the injection of heat or chemicals, as shown in Figure 1.2 (Stosur *et al*., 2003). The fundamentals of applying tertiary recovery are shown in Figure 1.4.

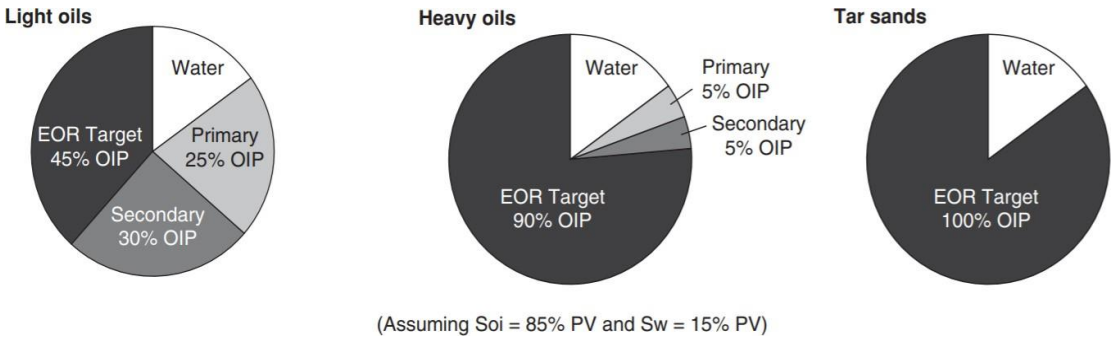

Figure 1.4: Fluid saturation and the target of EOR for light oils, heavy oils, and tar sands (taken from Thomas, 2007). The pie chart also shows why tertiary recovery, which is also referred to as EOR, is important to study and develop. EOR is applicable after the second recovery process for light-oil reservoirs, and the EOR target is ~ 45% of the original oil-in-place (OOIP). Nevertheless, as one transitions from light oils to heavier oils to tar sands; it gets becomes more difficult to produce oil. Eventually, tar sand cannot be produced at all unless enhanced oil recovery methods are used (Thomas, 2007). Soi and Sw refer to Oil saturation and Water saturation respectively.

These methods are loosely termed physical, chemical or thermal methods, though in practice, there are elements of each of these in all the methods. Figure 1.5 shows a plot of incremental recovery above a baseline recovery to show how the tertiary oil recovery is different from primary and secondary recovery, which also emphasises its effectiveness.

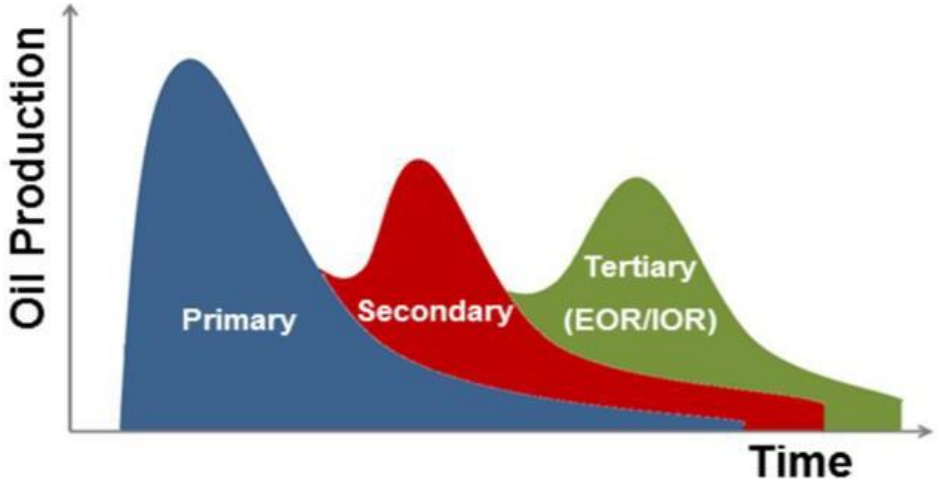

Figure 1.5: Plot of oil recovery phases, taken from Pershad (2012)

Water Alternating Gas (WAG) – Rather than injecting only water, or only gas (CO2), both water and gas are alternately added for periods of time. WAG results in better sweep efficiency by restraining gas channelling (WAG - Schlumberger Oilfield Glossary, 2019).

Chemical Methods – In general, injecting chemicals changes the interfacial tension between the two fluids (oil/water) and/or changes the rock wettability from oil/gas-wet to water-wet (Gbadamosi *et al*., 2019). Polymers may be added to alter the viscosity of the injected water and to reduce the viscosity difference between the injected water and the oil. Surfactants work like detergents in that they are used to reduce the interfacial tension (IFT) of trapped ganglia and droplets of oil.

Alkaline chemicals, such as hydroxide and carbonates, might be injected in an aqueous solution. These alkaline chemicals react with long chain acids in the oil to immediately form surfactants in situ (Samanta *et al*., 2011). Alkaline surfactant polymers (ASPs) are injected in sequences or as a mixture to improve the mobility and reduction of IFT. The significant disadvantages of using chemical methods are that they may be high-priced and can potentially result in the contamination of groundwater, from chemical spills or leaks (Millemann *et al*., 1982).

Steam Flood/Injection – Steam is injected rather than water to reduce oil viscosity (Zerkalov, 2015), thus this method is mostly utilised in shallow reservoirs that contain high-viscosity crude oil. The disadvantages of this method are steam override and excessive heat loss (Thomas, 2007).

In-Situ Combustion – Air or oxygen is injected and starts a fire inside the reservoir. It forms a burning front, and the front burns through the reservoir. The temperatures generated are extremely high and can vary between 450 °C–600 °C in a narrow zone. Similar to the steam flood, the viscosity drops and thus hydrocarbons can easily and quickly escape. However, in order for this method to be acceptable for commercial use, adopting it must be financially viable. Meeting this criteria has prevented this method from being advanced to commercial use stages. (Shen, 2002; Thomas, 2007)

1.3 Low-Salinity Enhanced Oil Recovery (EOR)

1.3.1 What is Low-Salinity EOR?

Low-salinity enhanced oil recovery (LS-EOR) is one of the most versatile secondary/tertiary production techniques used to extract additional hydrocarbons from producing oil fields by applying a flood of economic and environmentally-friendly diluted seawater of the range between 1000 mg/L to 3000 mg/L (Table 1.1). The idea of LS-EOR emanates from the

investigation conducted by Martin (1959), in which the effectiveness of injecting freshwater into a sandstone reservoir to better enable the recovery of highly viscous crude oil was demonstrated; this research was the first time that the injection of fluid other than reservoir formation brine and, based upon these initial studies, researchers started to become aware of the link between water salinity and composition and oil recovery rates (Rezaeidoust *et al*., 2010). Recently, LS-EOR has become of increasing interest in both the secondary and tertiary phases of oilfield production (Winoto *et al*., 2012; Takeya *et al*., 2019). Though a number of mechanisms for LS-EOR have been proposed, and implementation at field-scale is under way, there still remain areas of uncertainty that require further research in order to constrain the underpinning mechanisms at work in LS-EOR.

1.3.2 Conditions Displaying Low Salinity Effects

Based upon investigations undertaken by Tang and Morrow (1999a) and researchers from BP (Lager *et al*., 2007; Lager *et al*., 2008), certain conditions are considered as required for LS-EOR to display a positive result (Austad *et al*., 2010). Although the robustness and general applicability of some of the conditions tends to be controversial (Jackson *et al*., 2016), these conditions are the foundation of recent studies, such as those of Xie *et al*., (2016) and Morishita *et al*., (2020), and the following conditions are widely acknowledged as a basis for observing LS-EOR effects:

1) The inclusion of clay minerals in the reservoir rock unit is a requirement (Tang and Morrow, 1999a; McGuire *et al*., 2005; Pu *et al*., 2010; Austad *et al*., 2010; Jackson *et al*., 2016; Al-Saedi *et al*., 2018; Katende and Sagala, 2019).

- Clay is more susceptible to swelling, which leads to wettability alteration in the presence of multivalent ions (Mugele *et al*., 2015).
- The significance of clay minerals in the system has been widely acknowledged (Tang and Morrow, 1999a).

2) The presence of polar oil components is required, hence non-polar oil show no LS-EOR effect. (Austad *et al*., 2010; Jackson *et al*., 2016; Katende and Sagala, 2019).

- polar components in crude oil are required to bond to negatively charged clay surfaces by bridging multivalent ions and which will alter to water-wet when low salinity water is injected, thus polar components play a role (Mokhtari and Ayatollahi, 2018; Chavan *et al*., 2019).

3) The presence of a formation brine containing divalent cations is required in the initial system (Lager *et al*., 2008; Austad *et al*., 2010; Sharma and Filoco, 2000; Bartels *et al*., 2017;

Al-Saedi *et al*., 2019; Katende and Sagala, 2019).

- Divalent cations in the formation brine act as bridges between the interface of clay minerals and oil; changes to this bridge consequently helps to alter the wetting state of both positively and negatively charged polar components in crude oil hence offering the prospect of higher desorption of oil when low salinity brine rich in monovalent cations is injected (Austad *et al*., 2010; Katende and Sagala, 2019).

4) The effects of temperature variation have not yet been reported, however most of the studies undertaken have been conducted under 100 °C (Austad *et al*., 2010).

- The petroleum reservoir temperature depends on the depth of where the reservoir is found and its local geothermal gradient (Lovering and Goode, 1963; Kargarpour, 2016) however, in general, most oils generate in the range of between 100 °C and 150 °C (Quigley and Mackenzie, 1988; Ma, 2016), then migrate upward; in addition to that oil cracking will usually begin to occur at 150 °C (Ma, 2016). Therefore, considering the reservoir temperature as below 100 °C would be the general approach.

5) Low salinity flood water brine was required at a significantly lower salinity than the formation brine (Jackson *et al*., 2016).

- Further information about the relative composition of different water salinities is presented in Table 1.1

1.3.3 Average Recovery Rate and Salinity of 'Low-Salinity' Water

Although tests and researchers have not all used exactly the same salinity, the scope of what can be considered 'Low-Salinity' water and formation water, has been explored in previous studies, (such as Tang and Morrow, 1999a; Tang and Morrow, 1999b; Webb *et al*., 2005a; Webb *et al*., 2005b; Zhang and Morrow, 2006; Zhang *et al*., 2007; Lager *et al*., 2007; Austad *et al*., 2010), and all concur that performing tertiary oil recovery with salinity between 1000 mg/L and 2000 mg/L is the most effective method, as referred to in Table 1.1.

Lager and Austad (Lager *et al*., 2007; Austad *et al*., 2010) have also reported that the average additional recovery rate, after application of the LS-EOR process is ca 14% in sandstone reservoirs.

Table 1.1: Parameters for saline water (adopted from USGS, 2020); 1000 mg/L to 3000 mg/L of low salinity water is 12× to 35× diluted as compared to average ocean water.

Fresh Water	<1,000 mg/L
Slightly Saline Water	>1,000 mg/L to 3,000 mg/L
Moderately Saline Water	>3,000 mg/L to 10,000 mg/L
Highly Saline Water	>10,000 mg/L to 35,000 mg/L
Ocean Water	Approximately 35,000 mg/L

1.4 Evidence for and Effectiveness of Low-Salinity Enhanced Oil Recovery

Although the dominant mechanism for creating a LS-EOR effect is still unclear, (Al-Saedi and Flori, 2018; Jackson *et al*., 2016; Chavan *et al*., 2019) there is mounting evidence to support LS-EOR from research that has been conducted in a number of field and laboratory experiments (Takeya *et al*., 2019), not only in sandstone reservoirs but also in carbonate reservoirs (Shariatpanahi *et al*., 2010; Austad *et al*., 2011; Yousef *et al*., 2011; Alameri *et al*., 2015; Mahani *et al*., 2017; Maskari *et al*., 2019; Honarvar *et al*., 2020).

Clair Ridge a giant oil field located on the United Kingdom continental shelf, is also known as the site of the world-first employment of BP's breakthrough LS-EOR technique (Robbana *et al*., 2012). BP, over the last ten years, (Robbana *et al*., 2012) have conducted research using a variety of methods to test oil recovery, and the unit of measurement changes depending on the types of test administered.

These tests include core flooding tests using a scale of up to several centimetres, field-based single-well chemical tracer tests using a scale in the order of meters, and field tests in inter-well studies measured in kilometres (Robbana *et al*., 2012). These tests, using these three differing scales, were conducted in order to provide significant evidence for effectiveness to support the use of low salinity water for EOR (Robbana *et al*., 2012)

1.4.1 Coreflooding Test

At Clair Ridge, Robbana *et al* (2012) applied low salinity floods to core samples from the main field area, and tested these under the full reservoir conditions of temperature and pressure. De-gassed fluids (recombined Clair oil) were used to saturate the cores obtained and these were aged for three weeks (each week the residual oil was refreshed). The results

show that 9.0% and 13.1% of incremental oil were observed from the two cores after flooding with 1500 mg/L of diluted sea water in the secondary mode.

1.4.2 Field Tests of Low Salinity Enhanced Oil Recovery

At the Endicott field on the North Slope of Alaska, Seccombe *et al* (2010) conducted an inter-well field trial to demonstrate whether the LS-EOR process also works at field scale (Figure 1.6). The trial was undertaken in a single reservoir zone, saline water was then produced and injected prior to low-salinity water also being injected. At a distance of 317 m, the producer well was monitored for a change in watercut and ionic concentration. The results show that the oil rate was enhanced after the initiation of low-salinity water injection. In addition, the increment of the oil rate was recorded alongside the reduction in the watercut. The reduction of the watercut for a certain period and consequently back to predicted watercut fraction, is evidence that the oil increase was produced due to the injection of the low-salinity water. It is also worth mentioning that approximately 13% of oil recovery owing to the injection of low salinity brine was confirmed by comparing the pilot recovery profile and the scaled core-flooding recovery profile (Seccombe *et al.*,2010).

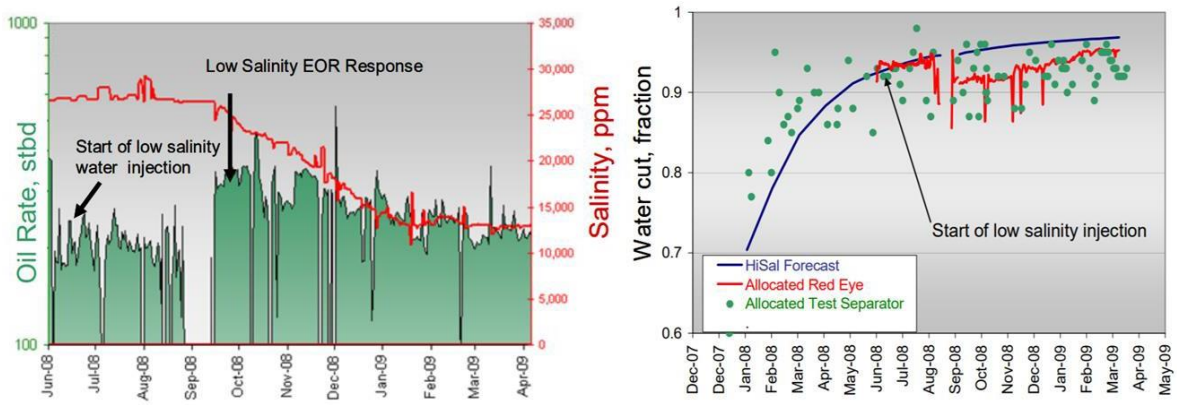

Figure 1.6: [Left] The pilot producer recorded that oil rate was increased as the arrival of low-salinity brine. Produced saline water was injected in December 2007, after that low-salinity water started injecting in June 2008. [Right] (Blue) The watercut fraction which predicted for the case of injecting high-salinity water alone, (Red) watercut at the well head measured by watercut meter, (Green dots) Flow rate assessed from the Endicott test separator and watercut measured by separator shake-out samples. Both the red curve and green dots show that watercut dropped from approximately 95% to 92% and it continued for around five months. The result indicates that the oil bank was produced by the function of injection low salinity water. In addition to that, their result was anticipated based on their coreflooding test and single-well chemical tracer tests (taken from Seccombe *et al.*, 2010)

1.5 Understood Low Salinity Enhanced Oil Recovery Mechanisms

Numerous mechanisms have been postulated to explain the LS-EOR effects, including fines migration and consequent reduction in permeability redirecting the floodwater, multi-component ion exchange (MIE), electric double-layer (EDL) effects, pH effects, mineral

dissolution, osmotic effects, desorption of polar components, micro dispersion formation, viscoelasticity, wettability alternation and the effect of emulsions (Takeya *et al*., 2019;Morishita *et al*., 2020). Although the dominant mechanisms vary dependent upon the research performed and their methodologies, the most commonly agreed mechanisms of LS-EOR, such as pH effects, MIE, EDL, and fines migration are introduced and briefly explained in the following sections. Furthermore, generation and stabilisation of the oil/water emulsion is also introduced as a propitious mechanism. Although oil/water emulsion stability has hardly ever been mentioned, a positive LS-EOR result was recently observed and ascribed to formation and stabilisation of an oil/water emulsion (Morishita *et al*., 2020).

1.5.1 pH Effects

The idea behind the pH effect is that the flooding low-salinity water mingles with the acidic-formation water, in which mineral surface adsorbed Ca^{2+} was substituted by H^{+}, leading to an increase in local pH due to the generation of hydroxide ions (OH^{-}), as shown in Figure 1.7.

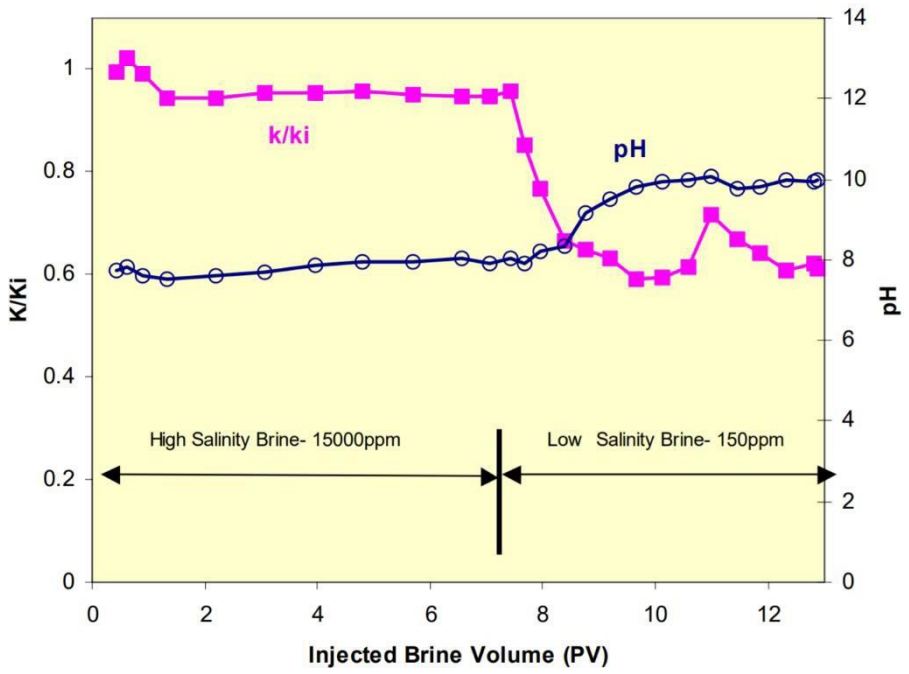

Figure 1.7: Shows how the injection of low-salinity water resulted in the increments of pH values up to 10 (taken from McGuire *et al*., 2005;. One of the first reactions to more alkalinity is the desorption of organic material from the clay. The detachment of clay particles is one of the mechanisms (Austad *et al*., 2010). [k/ki] ; BP-operated North Sea Field rock/ BP-operated North Sea Field brine system.

The formation water tends to be acidic – approximately pH 5 due to the dissolution of acidic gases, such as $CO_2$and H_2S. Clay minerals within the formation act as cation exchange

materials and thus adsorb acidic and protonated basic components, and especially divalent cations such as Ca^{2+} from crude oil (Austad *et al*., 2010; Pinerez T *et al*., 2016).
As McGuire (2005) also showed the LS-EOR mechanism is similar to those found in alkaline flooding, where more alkalinity leads to the generation of surfactants from residual oil, thus the water wettability of the reservoir increases, and the oil-water IFT decreases.

$$(RCOO)_3C_3H_5 + 3\,NaOH \rightarrow 3(RCOONa) + C_3H_5(OH)_3 \qquad \text{Equation 1}$$

Fat + Alkali → Soap + Glycerol

Equation 1 shows the general reaction of saponification. Through generating surfactants, this activity modifies the interfacial and surface tensions, which control the strength with which the oil is held in the pore space of the reservoir (McGuire *et al*., 2005). Furthermore, McGuire *et al*. (2005) suggested that flooding high-salinity water, which contains more divalent cations, had the effect of precipitating surfactants and, therefore, preventing increase of oil recovery (Equation 2), whereas a very low concentration of divalent cations and softer low-salinity water functioned more effectively to induce surfactant formation and LS-EOR.

$$2(\text{RCOONa}) + Ca(HCO_3)_2 \rightarrow (RCOO)_2 + 2(NaHCO_3) \qquad \text{Equation 2}$$

Soap + 'hardness' (=divalent cations) → insoluble soap curd
Numerous authors have previously observed elevated pH values during low-salinity water injection (Jackson *et al*., 2016). Santha *et al* (2019) focused on wettability alternations driven by the pH and chemical composition of model formation water; the study concluded that the pH of the formation water is an essential element for adhesion of oil at kaolinite surfaces. A lower pH was observed to lead to more oil-wet surfaces and a higher pH more efficiently increases oil recovery. In addition, a higher Ca^{2+}concentration leads to lower contact angle of oil, suggesting a more oil wetting surface. Therefore, using a lower concentration of Ca^{2+}during EOR operations would cause the clay minerals in the formation to become more water-wet and increase oil recovery. However, Zhang *et al* (2007) pointed out that the occurrence of saponification requires pH > 9 and, also, oil with high acid levels (> 0.2 mg KOH/g) would be required in order for saponification to occur.

1.5.2 Multi-component Ion Exchange (MIE)

The idea of MIE is that by injecting low-salinity water containing an excess of sodium cations relative to divalent cations, substitution of divalent cations and their associated bonding with polar components of crude oil in the system occurs, leading to oil release and a more water-wet surface, which then induces oil recovery. Lager and colleagues (Lager *et*

al., 2008) documented MIE while analysing effluent from coreflooding experiments, and showed that the concentration of Ca^{2+} and Mg^{2+} in the injected low salinity water initially decreased sharply. From this result, they hypothesised that the presence of divalent cations are essential in the formation brine in order for the clay surface and the polar components in the crude oil to bridge and then form complexes in the system. In addition, some of the organic polar compounds may have a direct adhesion to the clay mineral surface. Different types of adhesion mechanisms are shown in Figure 1.8 (Lager *et al*., 2008). The principal mechanisms of MIE are based on the balance water geochemistry and the mineral interface affinity for different ions. MIE occurs as a natural phenomenon, as cations with different affinity enthalpies are attached on the mineral surface, with the affinity from low to high tending to be $Li^+ < Na^+ < K^+ < Mg^{2+} < Ca^{2+} < H^+$ (Shariatpanahi *et al*., 2010; Austad *et al*., 2010). Injecting low salinity water into the formation water, i.e. water with different electrolyte concentration to the formation water, destabilises the thermodynamic equilibrium and leads to a redistribution of ions in the bulk and at surfaces. Alternation of ionic concentration leads to substitution of divalent cations by monovalent cations and, consequently, a modification to a more water-wet clay mineral surface and enhanced oil recovery (Pouryousefy *et al*., 2016). To support the mechanism of MIE and, to further test the relationship between the MIE and LS-EOR, Lager *et al* (2008) removed all the divalent cations from the formation system and then flooded with high-salinity and low-salinity water. As a result, LS-EOR was not observed in either case. However, a low-salinity injection into the sample with the originally presented divalent cations yielded an additional 5% recovery (Jackson *et al*., 2016).

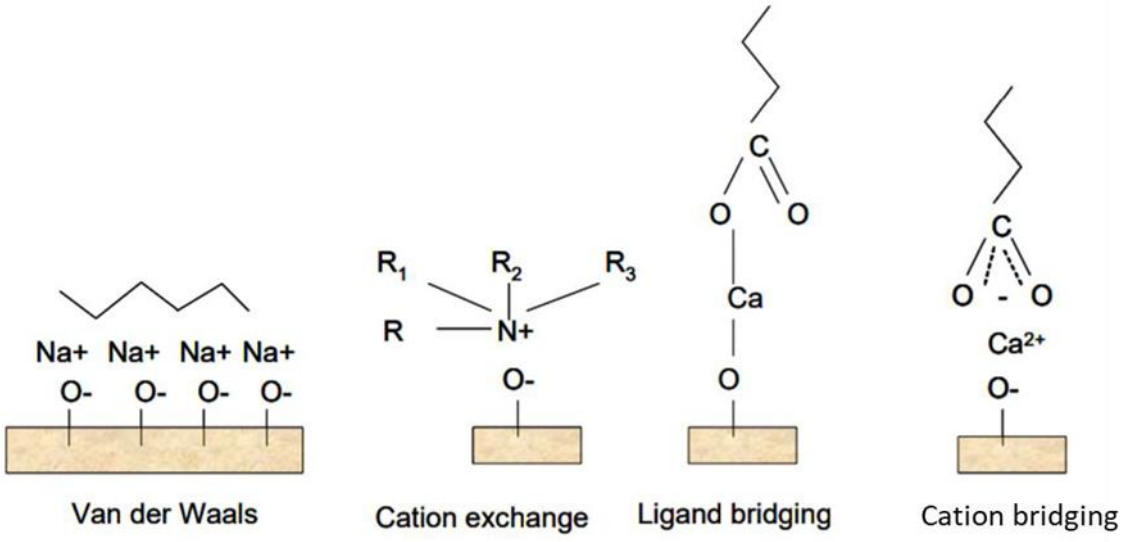

Figure 1.8: Four different types of adhesion mechanisms of clay surface and polar ends of the crude oil, which could be affected by cation exchange (Sposito, 2004). Injecting low salinity water breaks the surface interactions, which releases the oil components. (Lager *et al*., 2008)

1.5.3 Electric Double Layer (EDL) Effects

The idea of the EDL effect is that the 'double layer' comprised of the bulk of the ions close to the surface (Al-Saedi and Flori, 2018), expands after the process of injecting low-salinity water is performed due to a reduction of ionic strength in the system (Figure 1.9). This gives rise to increased electrostatic repulsion between the polar components of crude oil and clay surfaces and thus lower adhesion of oil components. Moreover, the Zeta potential, which is the electric potential at the slipping plane, changes (see Figure 1.9). The slipping plane has a thickness due to the EDL at the interface, as shown in Figure 1.10. The EDL thickness increases further due to the injection of lower ionic strength water. As a result, the clay surface will be altered to become more water-wet when electrostatic repulsion surpasses the bonding forces, which results in the desorption of the polar oil components (Ligthelm *et al*., 2009; Jackson *et al*., 2016).

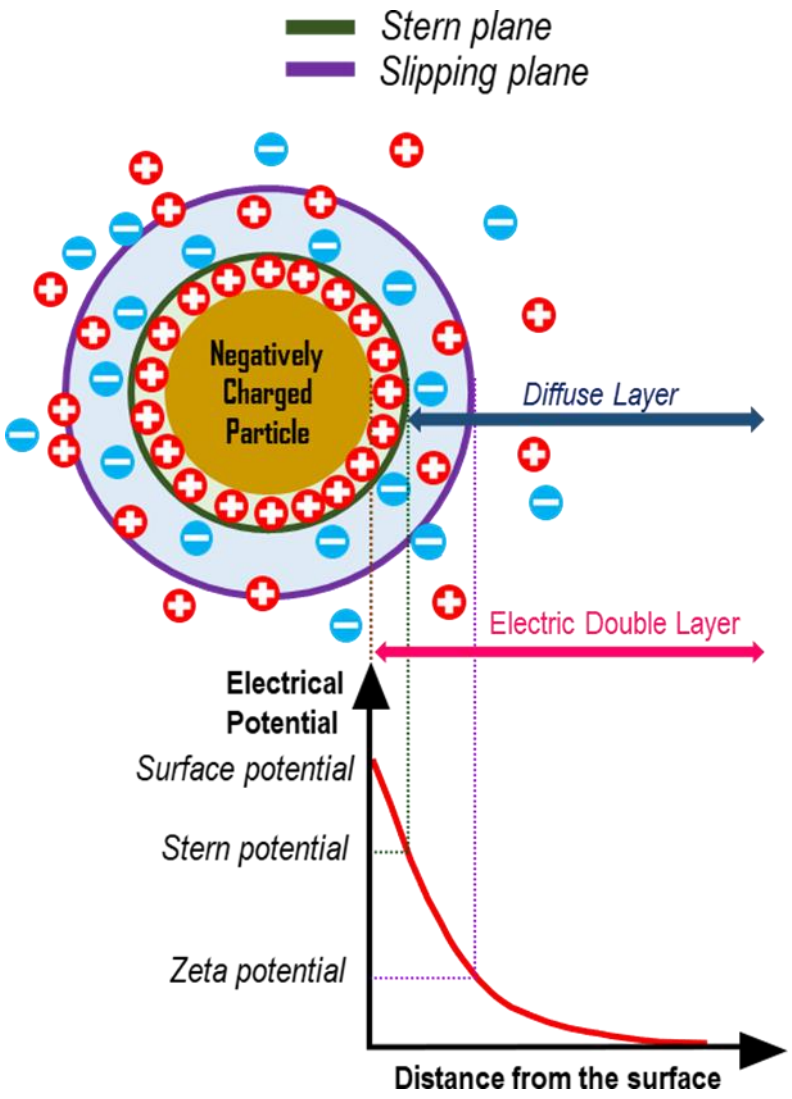

Figure 1.9: Schematic of the EDL, adopted from Nasralla and Nasr-El-Din, 2014

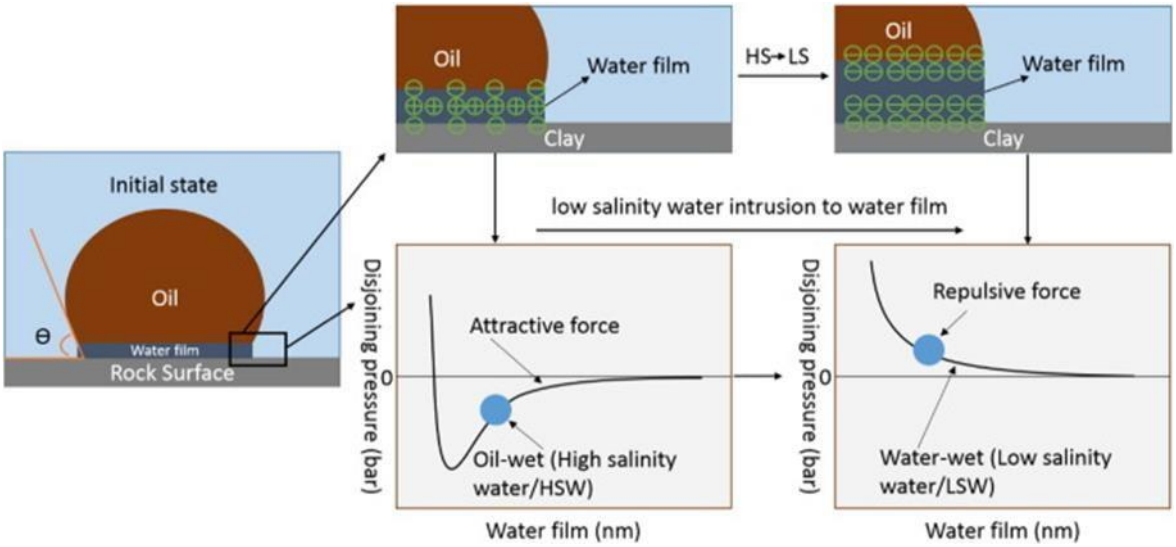

Figure 1.10: The thickness of the double layer positively correlates with the stability of the water film due to electrostatic repulsion, resulting in a more expansive water-wet surface. In contrast, a thinner double layer would have an oil-wet surface, which is not a suitable state by which to increase oil recovery (taken from Xie *et al.*, 2016 ; Wei *et al.*, 2017).

Recent research further justify this proposed LS-EOR mechanism. Wei *et al.* (2017) tested zeta potentials at the brine/solid and oil/brine interfaces with brines of five different salinities. Also Takeya *et al.* (2019), examined the electrical potential distributions of crude oil/brine surfaces with high salinity water and 30× diluted low salinity water (Figure 1.11).

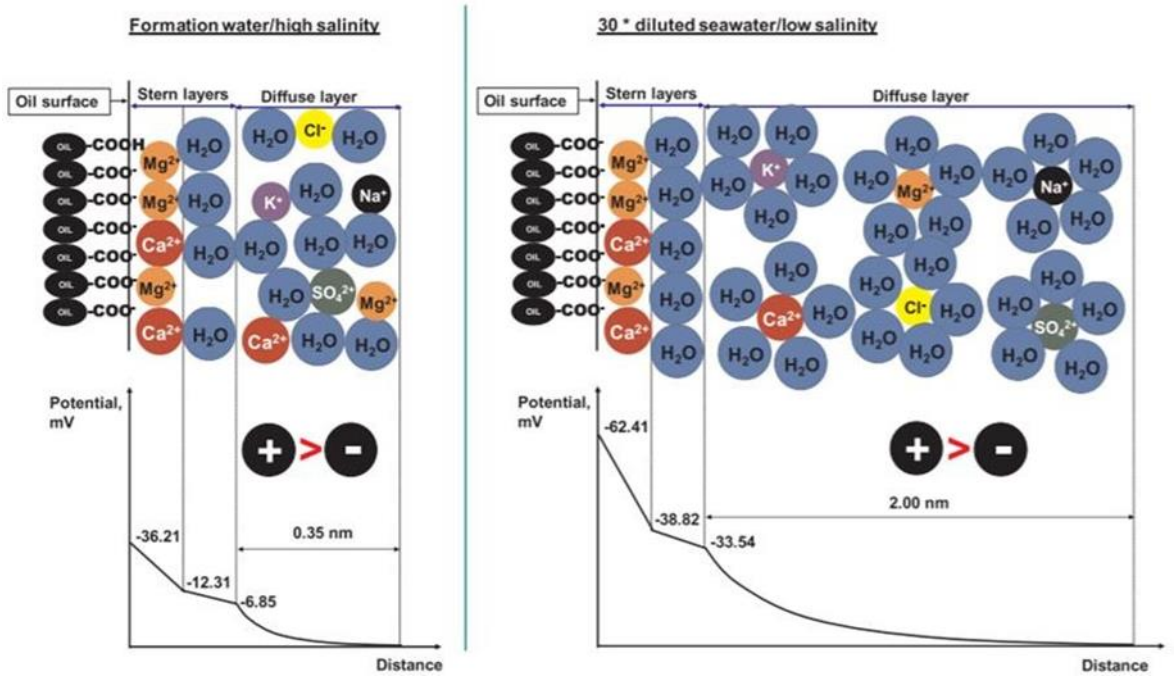

Figure 1.11: Showing the potential and ionic distributions at the interface of crude oil and brine. A highly negative zeta potential and more distributed ions were recorded during the injection of low-salinity water. It led to a more solid water-wet surface and the effect of the force changed from one of attraction to that of repulsion (taken from Takeya *et al.*, 2019).

The research concurred that zeta potentials increased in negative electrostatic repulsion as the salinity decreased. Thus, EDL mechanisms appear fundamental to wettability alteration, although MIE can still arise as a secondary mechanism (Ligthelm *et al.*, 2009). Furthermore,

Wei *et al*. (2017) concluded that the EDL effect is one of the foremost effective mechanisms that enhance oil recovery through injection of low-salinity water. Atomic force microscopy (AFM) data, such as that provided by Hilner *et al* (2015) and Siretanu *et al* (2014), as well as core plug scale measurements by Anderson (1986), support the mechanism of EDL expansion.

1.5.4 Oil/Water Emulsion Alteration and Fines Migration

'Fines' is a comprehensive definition of small mineral fragments which include clays (typically < 4 μm) and silts (between 4 and 64 μm), present within the reservoir rock matrix. (fines migration - Schlumberger Oilfield Glossary, 2020). During water chemistry alteration during a flood event, these fines may become mobilised and migrate with the flood water. Absorbed oil-bearing fines on the rock surface become more water-wet owing to the mechanisms mentioned earlier (pH Effects, MIE, and EDL expansion) and may be transported with the produced oil/water. In terms of stabilisation of the oil/water emulsion, it becomes more stabilised due to the increment of repulsive forces between droplets at low salinity conditions. Those detached fines and stabilised oil/water emulsion work in a similar manner in terms of LS-EOR.

As Figure 1.12 illustrates, in general, pathways in actual reservoirs are non-uniform. Water favourably flows in narrow pathways since capillary force surpasses that of viscous force and also oil is prone to trap in more extensive pathways. However, as detached fines and a stabilised emulsion block pores, it prevents the water from flowing in the narrow pathway, instead it has to flow in the more extensive pathway (Morishita *et al*., 2020). This mechanism is also acknowledged as 'permeability reduction' or 'formation damage' (Sarkar and Sharma, 1990; Souto and Bazin, 1993; Al-Sarihi *et al*., 2018), when it causes deleterious effects to oil production rates and it has been submitted that the subsequent effects of such mechanisms upon oil recovery would be ameliorative. What is more, in the case of emulsions, microdispersion of water would increase the volume of trapped oil in the rock pore pathway, which would enable oil recovery (Morishita *et al*., 2020). For fines migration, some researchers believed that oil is attached via the clay minerals, thus a detachment of clay minerals itself would realise incremental recovery of oil (Tang and Morrow, 1999a). While numerous mechanisms are thought to be the cause of LS-EOR, this research focused on fines migration.

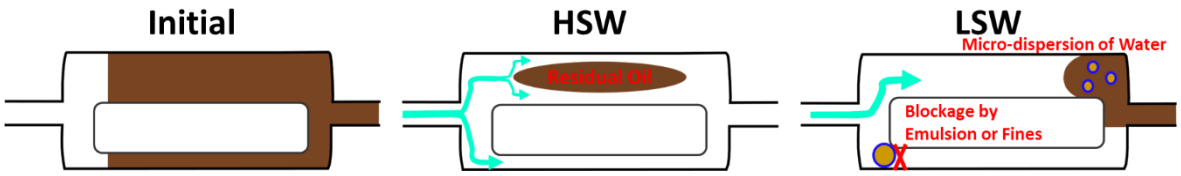

Figure 1.12: The model illustrates how permeability reduction takes place by detachment of fines and generation and stabilization of emulsion. The figures were adopted from Morishita *et al.*, (2020).

1.5.5 Summary

Many mechanisms of LS-EOR have been explored over the last decades. These also overlap with, and agree with, recent findings on wettability alteration, where inter-relating phenomena from all of the above mechanisms may be at work. Injecting low salinity water results in: (1) expanding the EDL between the clay surface and crude oil, and increases the possibility of cation exchange; this is also called (2) MIE which will release the adsorbed oil. Additionally, (3) the electrostatic repulsion enhances the water-wet surface (Takeya *et al*., 2019; Wei *et al*., 2017). Furthermore, injecting low salinity water automatically alters (4) the local pH to higher alkalinity, which in turn generates surfactants, which consequently increases water-wettability as well as transport of oil through the porous media (McGuire *et al*., 2005). (5) The detachment of clay particles which occurs when the surface is changed causes a water-wet result and is known as fines migration (Jackson *et al*., 2016). (6) Those detached clay particles and stabilization of emulsion subsequently blocks narrower pathways which allows water to flow consequently in more extensive pathways, thus sweeping residual oil that had become trapped in the more extensive pathways.

1.6 Methods for Studying Enhanced Oil Recovery at Mineral Surfaces

Though many experiments on LS-EOR have been undertaken, the earlier experiments, and many of the more recent, rely on comparing effluents from core flood experiments and inferring the changes occurring that arose due to changes in the floodwater. However, using techniques from surface science, myriad research has now been conducted utilising methods from the surface science community in order to understand the fundamental mechanisms and effectiveness of low-salinity water floods. Here, the principle instruments used thus far are introduced, including contact angle measurement (CAM), scanning electron microscope (SEM), environmental scanning electron microscopy (ESEM), atomic force microscopy (AFM), chemical force microscopy (CFM), and micro computed tomography (Micro CT).

1.6.1 Contact Angle Measurements (CAM)

Contact angle measurement is the straightforward and streamlined methodology to measure the angle where liquids, gases, and solids are encountered, and the contact angles reflect the wettability of that liquid on a surface (Figure1.13) (Wei *et al*., 2017; Kakati *et al*., 2020). For example, if the wetting liquid is water, the higher contact angles indicate the surface sheds the liquid, thus hydrophobicity for water, while lower contact angles suggested that the surface is more likely to wet with the liquid, thus exhibit hydrophilicity (Law, 2014; Huhtamäki *et al*., 2018).

The majority of aforementioned-promising mechanisms of LS-EOR effects, such as pH effects, MIE, and EDL increase the recovery rate of hydrocarbons through altering wetting state and ability to detach oil droplets from the rock surface. Figure 1.14 depicts three different wetting states: water-wet, oil-wet and mixed-wet. In the water-wet state, oil is displaced by water from the rock surface (Kareem, 2016) whereas, in the oil-wet state, oil is visibly adsorbing on the rock surface in that it does not look easy to desorb from the rock surface within the water sweep. Hence, it is believed that in-depth study of reservoir rock wettability alteration will be required in the future in terms of enhancing the production of hydrocarbons, through understanding the surface changes occurring as the wetting state of reservoir rock becoming more water-wet (Moghadam and Salehi, 2019).

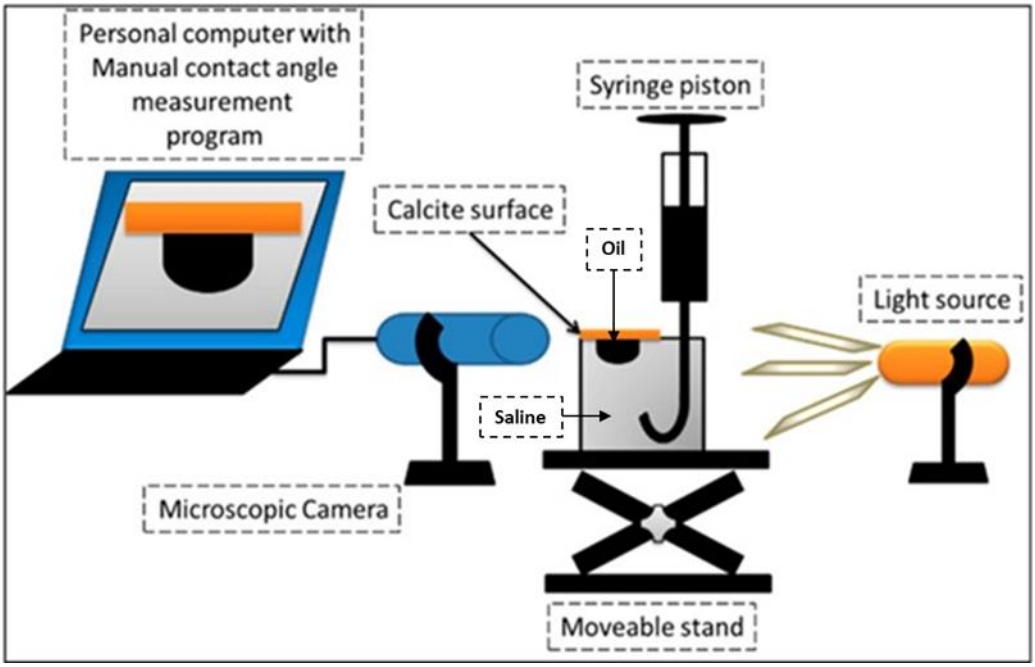

Figure 1.13: Schematic diagram of the CAM system, taken from (Al-Nofli *et al*., 2018). the surface of the rock sample needs to be at the top of the test cell and in contact with the water because the density of oil is lower than that of the surrounding salinity water. The camera next to the rock sample takes photos and enlarges the droplet image in order for this to be displayed on the connected computer. The average contact angles can be used for the entire experiment

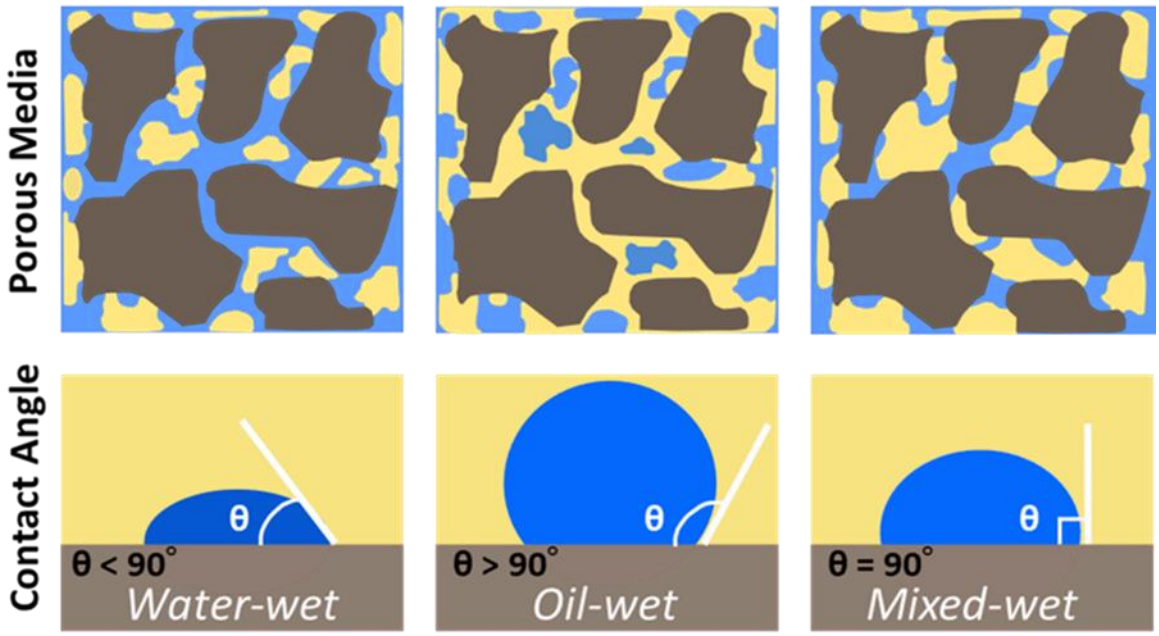

Figure 1.14: Schematic images of three types of wetting states, adopted from Moghadam and Salehi (2019).[Yellow] Oil [Blue] Water and [Brown] Rock.

Figure 1.15 shows that CAM conducted by Mahani *et al*., (2015), and the left-hand side of the image is demonstrating positive LS-EOR effects. Mahani *et al*., (2015) used a glass substrate covered by Na-Montmorillonite to model a typical sandstone rock surface, and added crude oil and observed contact angles during the system shift from high-salinity to low-salinity conditions. Under the high-salinity condition, the contact angle after 46 hours is almost identical to the initial state though noticeable contact angle change was witnessed even after 9 hours under the low-salinity condition. By the time 70 hours was reached after the system shifted to the low-salinity condition, the crude oil droplet was nearly detached from the surface. It is also worth noting that oil droplets start to detach from the surface when the contact angle alters to a critical value at around 40 to 50° (Mahani *et al*., 2015).

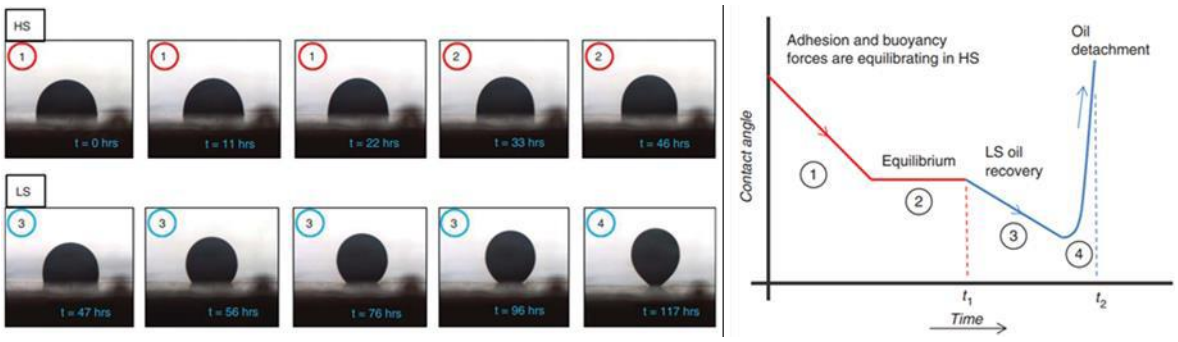

Figure 1.15: On the left-hand side of the image is n wettability alteration under high-salinity conditions and low-salinity conditions; the top-left numbers indicate each stage of the oil detachment process. On the right- hand side of the graph, describe the typical process of oil detachment during LS-EOR test; the red line indicates high-salinity condition, whereas the blue line is low-salinity condition. Both image and graphs are taken from Mahani *et al*., (2015).

1.6.2 Scanning Electron Microscope (SEM) and Environmental Scanning Electron Microscopy (ESEM)

SEM is a beneficial tool to view the topography of a rock sample at the nanoscale. For geoscientific studies, the pore space, composition, and paragenesis of sedimentary rock samples are often observed by SEM (Kareem, 2016).

Bhui and Sanyal (2017) confirmed wettability alteration by looking at the topography of crude oil-treated kaolinite, using SEM microphotographs. Bhui and Sanyal (2017) have observed edge loss of crude oil-treated kaolinite following low salinity treatment, as shown in Figure 1.16. The authors have concluded that the edge loss is to be ascribed to the diffusion of surface grains due to crude oil being replaced by low salinity brine.

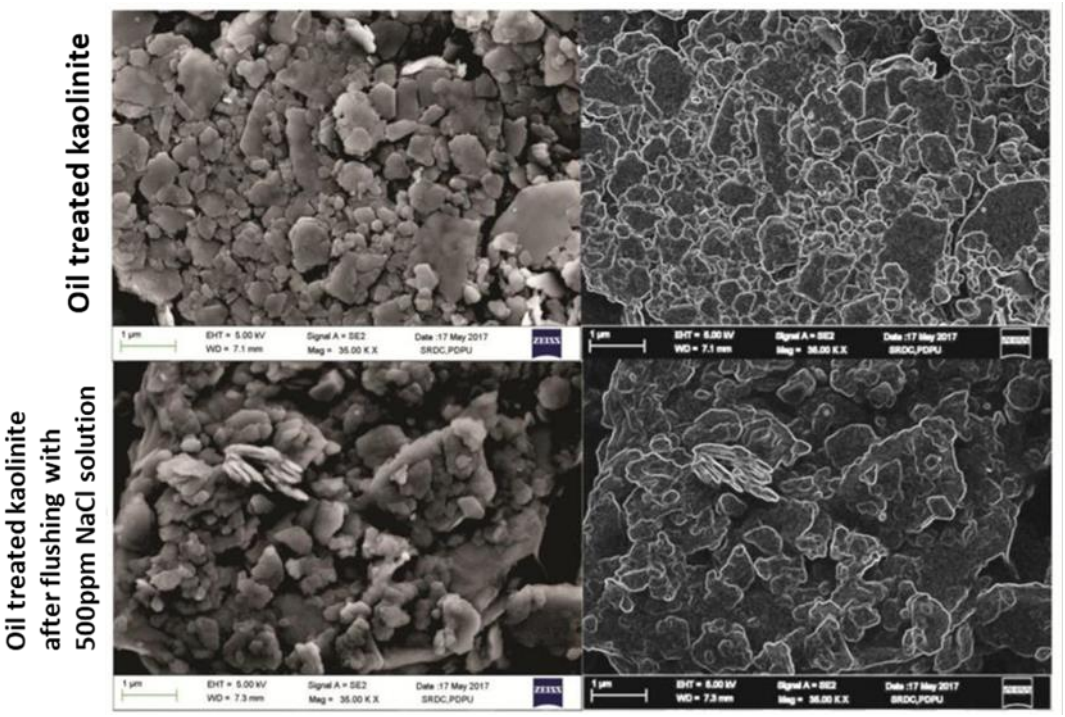

Figure 1.16: The field emission scanning electron microscope (FESEM) image captured by Bhui and Sanyal (2017). On the right-hand side the images are edited by IMAGEJ software to detect edges more distinctly. Oil treated kaolinite after flushing with 500 mg/L NaCl solution shows fewer edges as compared to oil treated kaolinite before being flushed with low salinity brine (Bhui and Sanyal, 2017).

Kareem (2016) observed the wettability alteration for the first time on detrital mineral porous media in aged Berea sandstone. Figure 1.17 illustrates ESEM micrographs of different wettability states on quartz surfaces in Berea sandstone prior to being aged with crude oil. The surface of (a) & (b), and then of (c) & (d) have been zoomed in upon at the same section respectively; (a) and (b) were treated with 0.01 M NaCl, whilst surfaces (c) and (d) were treated with 1.0 M NaCl. Water droplets shown in (b) indicate lower contact angles as compared to the water droplets in (d); thus the surface which was initially treated with low salinity brine shows more water-wet contact angles. Upon further study undertaken with ESEM, it has been revealed that applying lower ionic concentration of NaCl brine solution

has shown more water-wet states compared to that of $CaCl_2$ brine solution. It is also worth mentioning that based upon SEM photomicrographs of quartz overgrowth, quartz surfaces are generally coated with clay minerals such as kaolinite. The presence of these clay minerals on the quartz surface would have modified the wettability alteration since the clay minerals are associated with the hydrocarbon residues (Kareem, 2016).

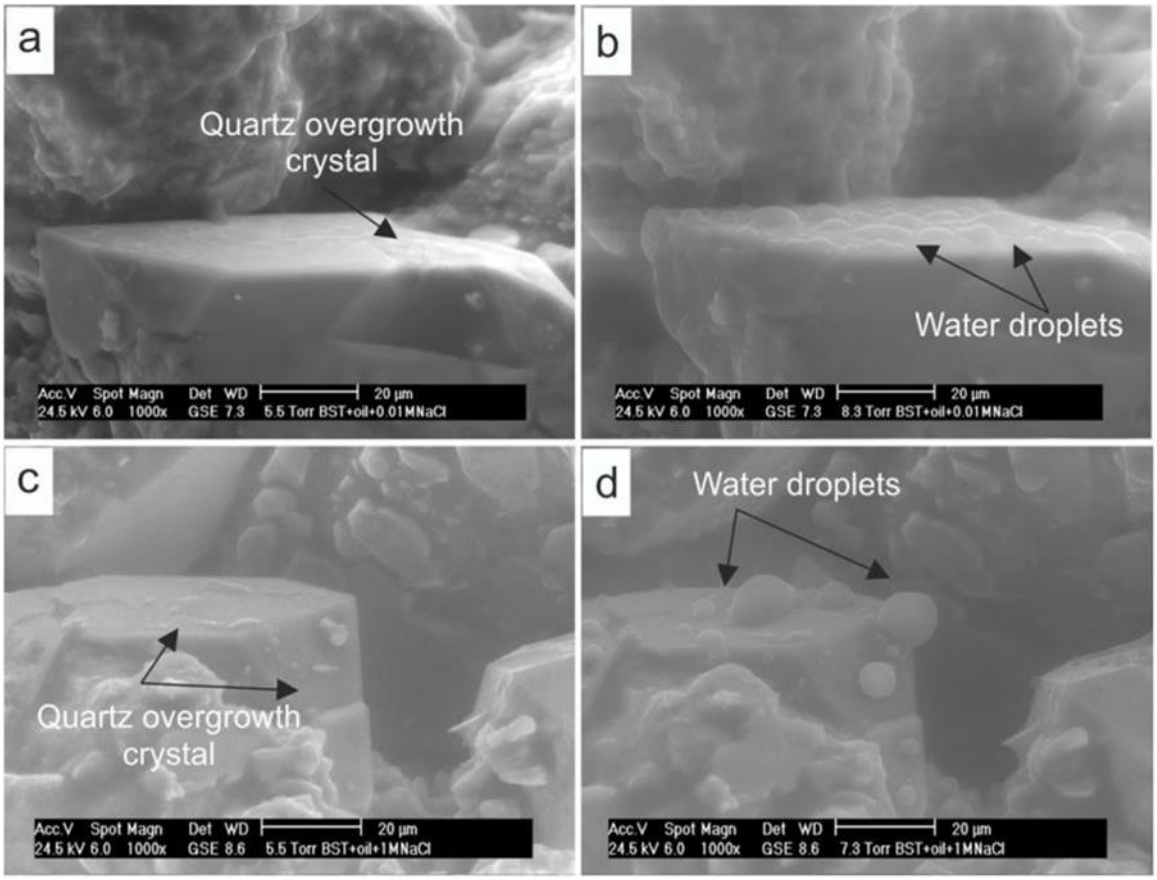

Figure 1.17: ESEM micrographs showing different wetting states. a) and b) are initially treated with 0.01 M NaCl, c) and d) are initially treated with 1.0 M NaCl. Water droplets in b) and d) are observed under 5 °C and 8.30 Torr and 5 °C and 7.3 Torr respectively. Taken from Kareem (2016).

The basic operation of the SEM is shown in Figure 1.18. Based on the conventional SEM, an advanced imagining technique called environmental scanning electron microscopy (ESEM) was created. ESEM can be applied to wet or non-conductive samples, whereas dried samples are required for operating the conventional SEM owing to the high vacuum required. As wet/hydrated samples can be imaged by ESEM, and dynamic experiments can be performed, thus a unique opportunity to study wettability is then garnered (Buckman *et al.*; 2000; Santha, 2019). Kareem conducted application of ESEM to LS-EOR study (Kareem, 2016), imaging wettability alteration of rocks and minerals as a fundamental step of understanding LS-EOR.

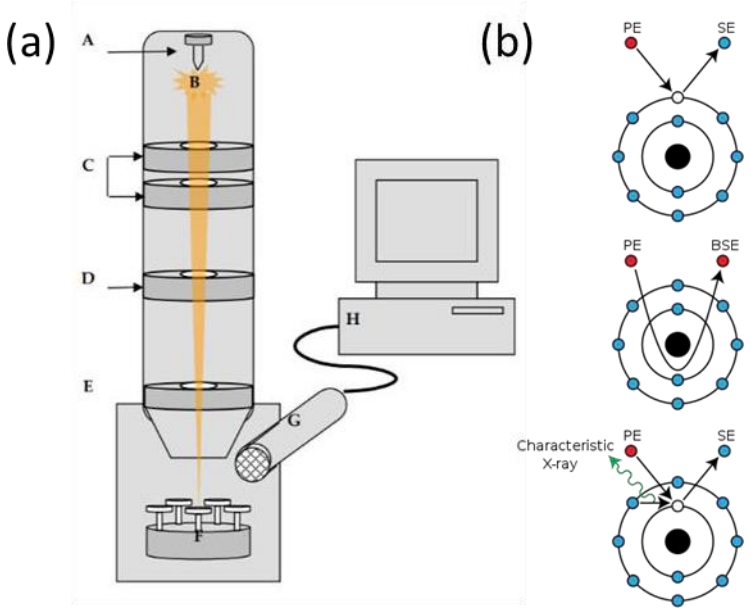

Figure 1.18: (a) The simplified schematic diagram of the SEM. A: The electrons are generated from the electron gun. B: Generated electrons are formed into a beam and then passed through the lenses to the sample. The beams are more concentrated and directed as they proceed through the electromagnetic lenses (C, D, and E). When the beam reaches the sample, electrons are knocked loose from the surface of the sample (these electrons are called secondary electrons). G detects these secondary electrons, and the signal is sent to monitor H. Taken from (Cpb-us-e1.wpmucdn.com, 2019). (b) The electron beam from the SEM, known as the primary electron beam, interacts with samples in different ways and emits different types of signals, including secondary electrons (top), backscattered electrons (middle), and X-rays (bottom). Taken from (Hurt, 2016; Santha, 2019).

1.6.3 Atomic Force Microscopy (AFM) and Chemical Force Microscopy (CFM)

Scanning tunnelling microscopes, (STM) investigate the surface topography of a sample at extremely high resolution by scanning an atomically sharp tip attached to a cantilever across a sample. Invented by Gerd Binnig and Heinrich Rohrer in 1981, unprecedented resolution images of individual surface atoms were captured by detecting the tunnel current between the sample and the probe (Rugar and Hansma, 1990). However, STM only applies to conductive surfaces and the atomic force microscope (AFM), which is also able to investigate surfaces of insulators was devised by Binnig *et al*., (1986), as shown in the schematic in Figure 1.19. Chemical force microscopy (CFM) has the same underlying instrument principle as AFM, though CFM uses chemically functionalised tips (e.g. carboxylic acid, alcohol, methyl) in the force spectroscopy, whereas standard AFM uses silicon or silicon nitride tips. As such, CFM measures the molecular interaction between a functionalised tip and a sample (Noy *et al*., 1997).

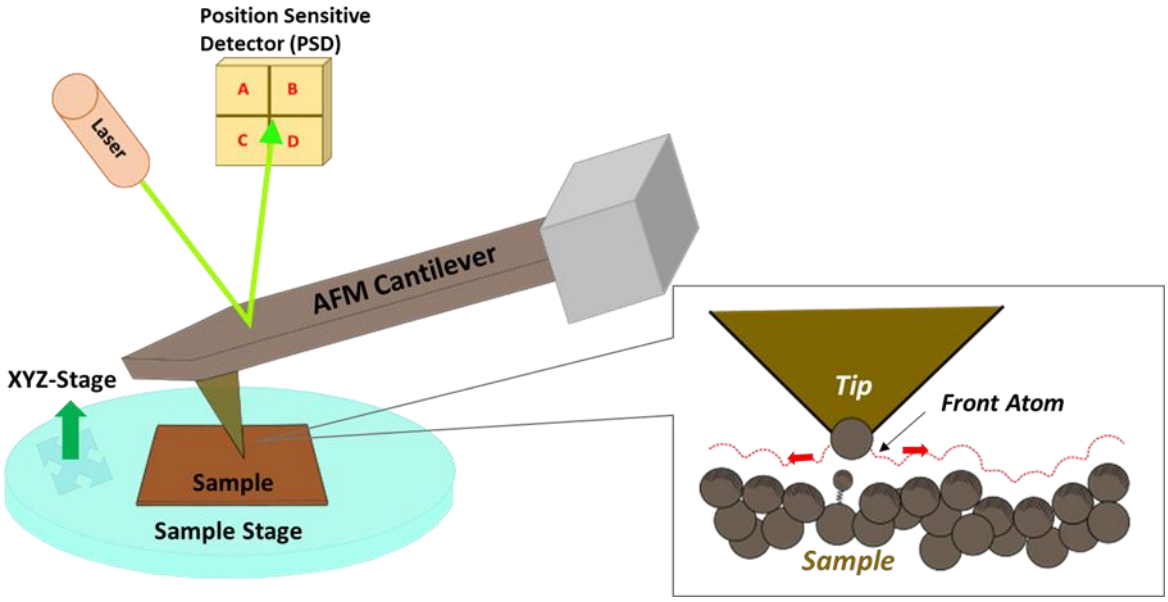

Figure 1.19: The principal operation of AFM: A flat top cantilever receives lasers, and it reflects these lasers, which will then be detected by position sensitive detector (PSD); cantilever deflection is caused by intermolecular attractive and repulsive forces found between the surface of samples and the tip, consequently this changes the data that PSD receives, also PSD monitors these changes (Pierce *et al.*, 1994). The tip of the AFM follows the contour, shown with the red dashed line, in order to persist the force between tip and sample (Binnig *et al.*, 1986). The figures were modified from (Binnig *et al.*, 1986; Kristian, 2013).

Yang *et al.*, (2015) studied the application of AFM to LS-EOR by injecting various concentrations of NaCl brine to the asphaltene-coated surface to observe the morphology of the films changes by absorption and desorption. Figure 1.20 illustrates the morphology of an original asphaltene-coated surface (as shown in histogram a), the morphology of an asphaltene-coated surface flushed with water (as shown in histogram b) and, the asphaltene-coated surface flushed with various concentrations of NaCl brine (as shown in histograms c-h). The original asphaltene-coated surface is shown in histogram (a), the surface is then shown after having been flushed with water in histogram (b). However, the differences between the two do not appear to be significant in terms of morphology whereas notable changes in morphology appear after the surface has been flushed with 1 mM NaCl; these differences were detected and therefore indicate that a more extensive amount of asphaltene molecules were detached after being flooded with low salinity brine. In addition to the AFM morphology investigation, Yang *et al.*, (2015) also coupled this with quartz crystal microbalance with dissipation (QCM-D) to scrutinize mass loading and asphaltene film thickness, also CAM was engaged to observe the wettability alteration. Based upon the combination of these three types of data, AFM, QCM-D, and CAM, Yang *et al.*, (2015) summarised that mass loading and asphaltene film thickness were decreased, also that more water-wet states were observed with the flushed water between 1 and 10 mM. In contrast, mass loading and asphaltene film thickness were increased, and more oil-wet states were

observed while flushing of water between 10 to 1000 mM.

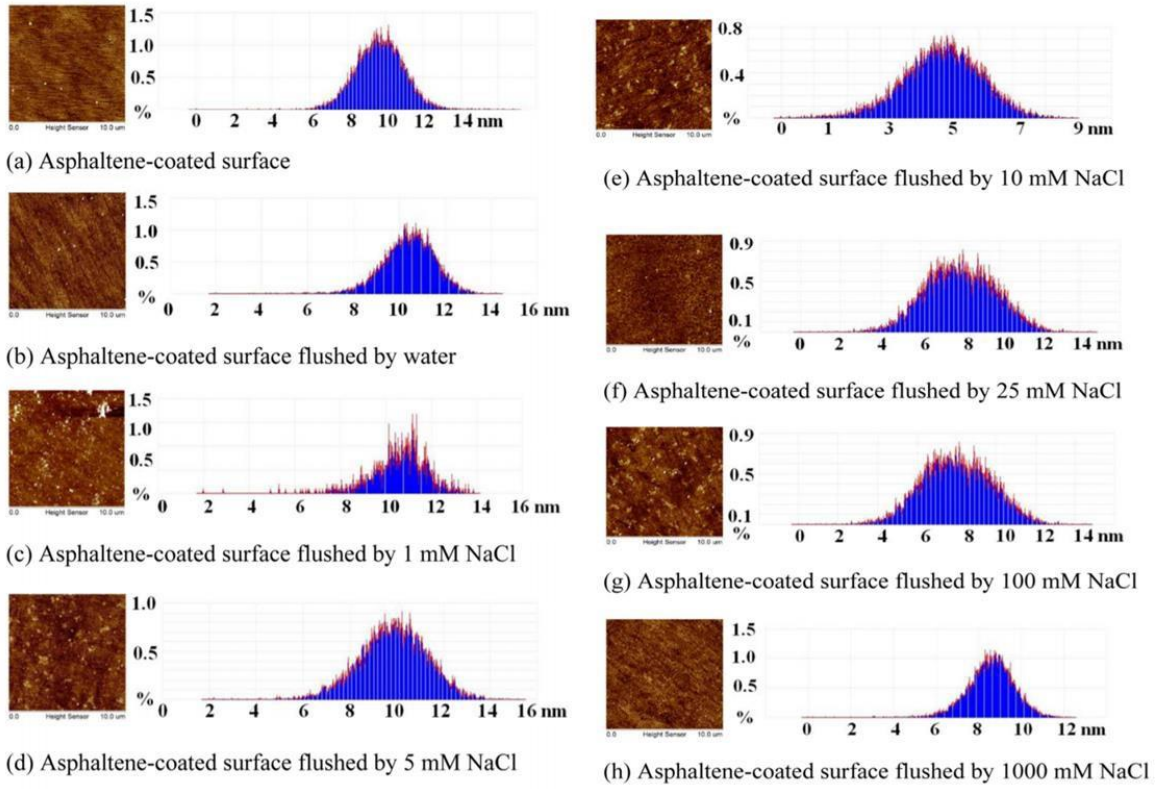

Figure 1.20: Topography images captured by AFM and the histograms represent the height of the samples. Histogram (c) depicts post-treatment with 1mM NaCl, clearly disarrayed as compared to histogram (a) and histogram (b), which indicates large amounts of asphaltene molecules were detached. Taken from Yang *et al.*, (2015).

In order to further understand unsolved-LS-EOR mechanisms, Desmond *et al.*, (2017) utilised CFM to illuminate the role of Ca^{2+}. As shown in Figure 1.21, the adhesion force of positively charged alkylammonium to silica in $CaCl_2$ is excessively stronger than the other electrolytes tested: NaCl, KCl, and $MgCl_2$. Moreover, the adhesion force of positively charged alkylammonium in $CaCl_2$ is also controlled by the concentration of the solution; higher ionic concentration in solution empowers the adhesion force. NaCl and KCl also showed slightly higher adhesion force in higher salinity solution, however, the difference in adhesion force between high salinity and low salinity is not distinct as with $CaCl_2$. In addition to that adhesion force of alkylammonium to silica in NaCl, KCl, and $MgCl_2$ are much lower than $CaCl_2$. By an integrated approach of CFM and molecular dynamics (MD) simulations, Desmond *et al*. (2017) successfully observed positive LS-EOR effects, concluding that the wettability alteration on a silica surface is controlled by electrolyte concentration.

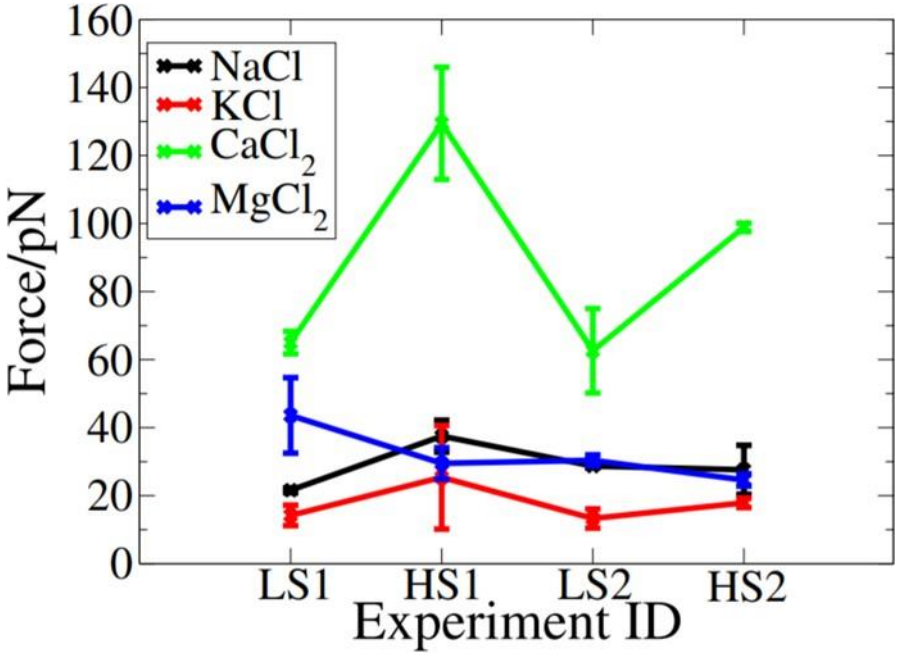

Figure 1.21: CFM force mapping data showing the average adhesion force of ammonia functionalised tip in each electrolyte. LS refers to low salinity brine, and HS is high salinity brine. 1 and 2 refer to the number of experiments undertaken. Taken from (Desmond *et al.*, 2017).

1.6.4 Micro Computed Tomography (Micro CT)

The micro CT uses X-ray imaging and density contrast to provide an image of the interior structure of samples at the micron scale (typically with a voxel resolution of *ca* 2 μm^3), thus the pore geometries, surface area, hydraulic radius, and aspect ratio of the core samples can be observed, while fluid flow takes place. Micro CT is one of the most powerful tools available to capture 3D and high-resolution images by applying non-destructive technologies (Akin and Kovscek, 2003). As such, CT scanning is often used in the medical field as well as, increasingly, within the geosciences (Boerckel *et al.*, 2014; Warwick, 2017). A schematic illustration of micro CT is shown in Figure 1.22 (Bagnell, 2018).

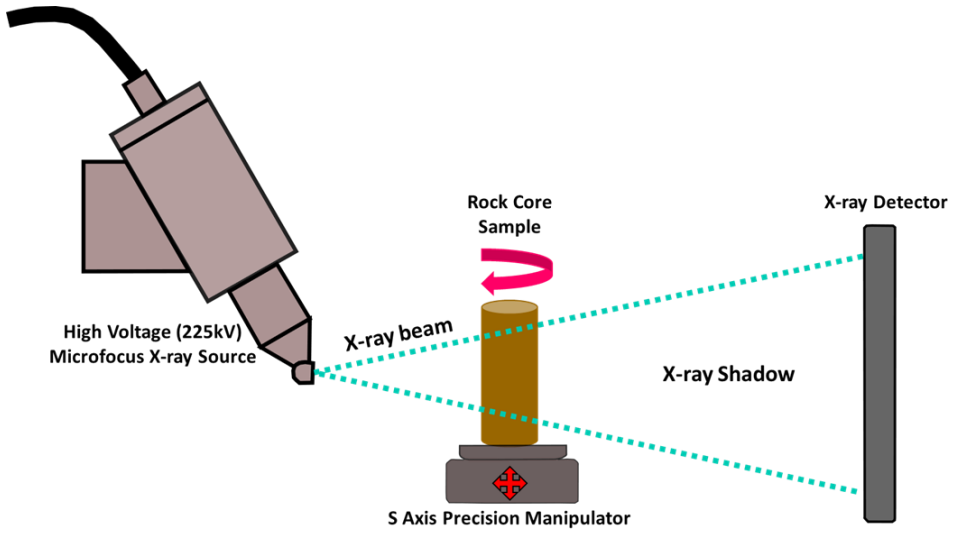

Figure 1.22: Schematic diagram of micro CT, modified from (Digimsolution.com, 2019). First, the X-ray is formed by directing electrons produced in a cathode, such as tungsten and copper. The X-ray is transmitted from the source towards the rock sample; the detector receives the shadow and then projects 2D images. Next, the sample is rotated 180 degrees or 360 degrees, and more S-ray projection images are taken. The cross-section images are made by those X-ray projection images, which are called reconstruction. Moreover, those 2D images are going to be the base of the 3D models (Bagnell, 2018).

Bartels *et al.*, (2016) and Bartels *et al.*, (2017) pointed out that the evidence supporting the aforementioned LS-EOR mechanisms are often indirect and inferred from standard LS-EOR investigations since most of the tests are undertaken either at sub-pore scale or on the scale of coreflooding. However, the wettability alteration in the pore and sub-pore scale as an influence to additional oil production at Darcy scale (pore network scale) is scarcely ever investigated. For that reason, Bartels *et al.*, (2016) and Bartels *et al.*, (2017) utilized micro CT (Synchrotron-based X-ray Microtomography) to focus on testing Darcy scale to link wettability alteration that was observed at sub-pore scale, and detachment of oil configuration as observed at the scale of coreflooding. Figure 1.23 shows a 3D rendering of a slow pore-filling event after high salinity brine was injected in the carbonate system.

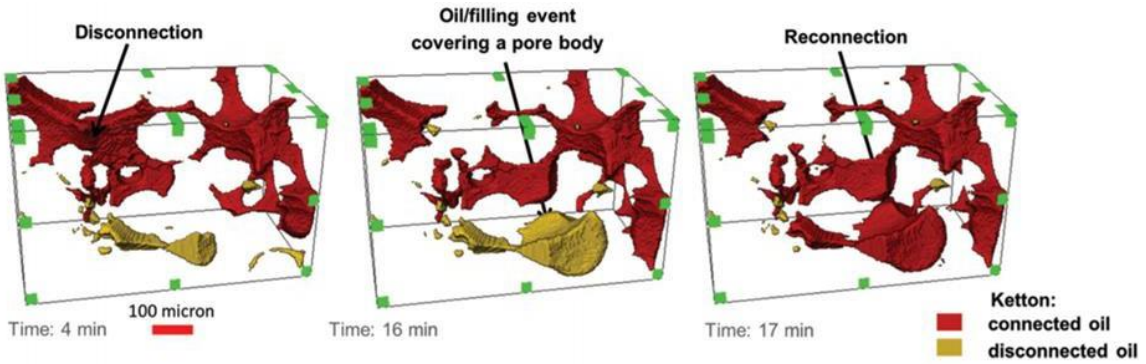

Figure 1.23:The 3D rendering shows disconnection and connection of an oil-phase cluster at the Darcy scale. The pore-filling event is witnessed within carbonate rock with high-salinity brine. The 3D rendering is taken from Bartels *et al.*, (2016) and Bartels *et al.*, (2017).

Although the study conducted by Bartels *et al.*, (2016) and Bartels *et al.*, (2017) have not yet discovered enough evidence and as a result not provided enough data to substantiate the

direct influence of LS-EOR effects, the 3D rendering clearly shows disconnection and connection of an oil-phase cluster at Darcy scale. Based upon the 3D rendering Bartels *et al*., (2017) concluded that the observance of pore-filling events owing to the flood of high salinity brine would have been distinct to the mixed-wet state, hence, the ageing process might play a key role for an increment of oil recovery.

1.6.5 Limitations of Methods for Probing Low Salinity Effects

Whilst the methods described above can give insight into surface wettability, they have some limitations, which are now described. For CAM to succeed, a clean and flat mineral surface is required. However, obtaining such a surface is difficult, especially in open-air experiments, and with materials such as clay minerals where the particle size is often far smaller than the size of the droplet deposited. The effect of surface roughness on a CAM may be greater than the change in contact angle due to wettability changes, and swelling/dispersing materials such as clay minerals may present varying roughness through an experiment. The requirement of a minimal amount of liquid and a small solid space can also be a disadvantage as this method also increases the risk and impact of impurities; even a small difference in droplet size might cause significant contact angle error. In addition, the camera next to the droplets (Figure 1.13) will be focused on the most extensive meridian section and thus reflect only the contact angle at the point where the meridian plane intersects the three-phase line (Chau, 2009). Kareem (2016) also states that droplets tend to spread across the surface with time, and the volume of the droplets might change due to the evaporation or absorption of moisture. As such, dynamic advancing/receding contact angle measurements are sometimes used, though these can be time consuming.

Owing to the high vacuum required, it is not possible to image phenomena in the SEM though the mineral surfaces can be imaged with high resolution. ESEM can be used to image water droplets at a very high resolution, though it is difficult for other fluids and the sample orientation can be hard to adjudge. Furthermore, an SEM requires expensive sample preparation. In addition, the tailings' chemical structures might be altered by working under a vacuum and a depressed temperature (Russell *et al*., 2001; Shende *et al*., 2016). AFM can be used to calculate changes in roughness and surface-area variations for samples under different fluids and in real time. Also, AFM does not require much sample preparation. However, a key disadvantage of AFM is that it requires a skilled operator to discern artefacts from the experiment and to gain the highest resolution images. A further problem arises with the reproducibility of CFM measurements, with both the sample and the tip altering throughout the experiment.

Micro CT is one of the most practical methods with which to visualise 3D images without destroying samples. However, it has three significant disadvantages; firstly, there is the penetrating ability of the X-rays relative to the density of the material sample. Denser materials are usually easier to visualise than materials of a lighter density thus, there is a high risk of not being able to observe the movement and presence of oil in the sample. Secondly, the image will be very poor when sample phases have substantial differences in X-ray adsorption. Finally, owing to the limited resolution without extremely specialist instrumentation, of ca 2 μm^3, it is hard to visualise fine particles such as clay minerals (Landis and Keane, 2010).

In summary, though many surface imaging methods can allow extremely high resolution imaging of certain surfaces and phenomena, there remains a need to find methodologies and approaches that can image fine particles under solution, in real time, and without the experiment altering the behaviour observed. In this thesis an attempt is made to address this through the use of confocal fluorescence imaging of clay minerals, with supplementary imaging with AFM. For the latter, measurements are made of indirect properties rather than trying to image unique particles, in contrast to approaches used hitherto in the literature.

1.7 Fluorescence Imaging in Mineral Science

Fluorescence images, as well as fluorescence microscopes have been utilised to understand the distribution of a small amount of substances. The high sensitivity of fluorescence microscopy is optimal to the study of the distribution of substances in living cells, thus often drawing on biology and the medical field is necessary, but fluorescence is also favourable in coal petrology (Rost, 1995), petroleum geoscience (Burruss, 1991; Ryder, 2005), and other fields of sciences. Fluorite minerals are famously known as fluorescing minerals, which also became the origin of the name ‘fluorescence’ (King, 2020). Though some of the pure minerals shows strong fluorescence, the following rules are considerate as the occurrence of fluorescent properties (Forster *et al*., 1985; Rost, 1995).

The primary reason for fluorescence is due to impurities within the minerals, and these impurities are quantum isolated defects (Tisler *et al*., 2009), also known as ‘activators’ (Rost, 1995). The samples sometimes required two species of activators to fluoresce due to role distributions; one activator creates an adsorption band for excitation to occur while another activator meanwhile undertakes a role in fluorescence.

Secondly, the samples also fluoresce when fluorescent organic materials are present or infiltrated. Those organic materials include macerals, bituminous compounds and oil. Observing fluorescence of protein is very common for biology and medical applications.

Thirdly, fluorescence of uranium, other actinide, and lanthanide are intrinsic properties. Thus, those uranium minerals can be activators when the samples comprise them.
Another key point of consideration is that elements including iron, cobalt, and nickel are inhibitors. In addition to that, excessive concentrations of activators might be responsible for quenching fluorescence.
Finally, reduction in the degree of hydration is affiliated with diminishing of fluorescence.

1.8 Aim of the Study

The ultimate aim of this research project is to trial new methods in observation of release and migration of 'fines' (small clay mineral and other particles, found in sandstone reservoirs) after a low-salinity water injection, the results will be utilised for further understanding of low-salinity enhanced oil recovery (LS-EOR). Understanding clay mineral detachment and migration, as well as broader LS-EOR effects, will lead to the development of more efficient crude oil extraction from existing reservoirs. Extraction of additional petroleum from existing reservoirs rather than drilling new petroleum reservoirs would help the development of the future energy supply since society as a whole are concerned with these environmental issues, so much so that many may prefer petroleum industries to curtail or maintain current petroleum exploration levels (Fears and Clement, 2019) while global energy demand has continued to increase (BP Energy Outlook 2019 edition, 2019).
In order to aim at achieving success, experimental steps and the objective of the research project are listed below:

- The project seeks to develop the use of confocal microscopy with the use of a fluorescent microscope that will later be coupled with total internal reflectance fluorescence (TIRF) microscopy, a method as yet to be applied to studying LS-EOR.

- For the first step of this project, confocal microscopy has been applied to test any inherent fluorescence of various types of clay mineral samples to set a baseline for further imaging and identifying the optimal clay mineral to use. This will be valuable in the understanding of whether or not clay samples are fluorescing and useful in comprehending patterns and features of clay fluorescence.

− Having identified highly fluorescent clay samples in accordance with the first step, the clay samples will be placed inside TIRF cells in such a way that the real time reactivity of clay minerals to changes in fluid salinity may be imaged.

− In spite of the fact that innumerable research has been conducted in studies on LS-EOR, with numerous methods and conclusions having been reached, as yet fluorescent imaging has received relatively little attention. Confocal microscopy has a possibility of becoming one of the most capable instruments in terms of verifying LS-EOR effects, combining non-destructive in situ imaging, capable of handling different liquids.

- The rest of the thesis is structured as follows: In Chapter 2, the focus is upon introducing the main instruments of this project, the so-called confocal microscopy and its mechanisms, as well as how all the samples were prepared for each instrument; confocal microscopy, TIRF, SEM, and AFM.

- Chapter 3 presents the findings of the project and discussion based upon images captured from confocal microscopy with supporting data from SEM, AFM, commercially provided XRD data; the previously published literature are provided.

- Chapter 4 presents the testing using TIRF revealing the swelling and migration of clay minerals owing to the reduction of the salinity level.

- Chapter 5 Presents cohesion measurements of clay minerals which were aged with high salinity and low salinity water by using AFM.

- Chapters 6 and 7 are the discussion and the final summaries including an overview of further work arising from this project.

Chapter 2 Experimental Methods

2.1 Experimental Approach and COVID-19 Mitigation

The initial plan of the project was to test fluorescence of clay minerals by confocal microscopy and subsequently test migration of these fluorescent clay minerals by TIRF. However, due to the COVID-19 pandemic, and its subsequent effect within the UK, which required Durham University to enter a lockdown from March 2019 and the strict restriction for accessing laboratories; a contingency plan had to be put in place as the lockdown procedures were continued even after the country-wide lockdown was relaxed somewhat.
In order to use the time effectively and progress with this study even under the circumstances, XRD analysis and AFM were added to this project; XRD analysis was outsourced to X-ray Mineral Services Ltd and AFM data was collected by Dr Miro Cafolla on the basis of the initial experimental design by myself. In addition, TIRF was eventually carried out by Miss Joanne Robson due to the laboratories in the Biosciences department where the TIRF was located being one of the last departments to re-open. Also TIRF is a the super-resolution microscope that requires proper training and delicate handling; the prepared samples were entrusted to Miss Joanne Robson, the Imaging technician, and the entire experiments were remotely shared and steered by myself.

2.2 Principle of Confocal Microscopy

Confocal microscopy was invented by Marvin Minsky in 1955 (Semwogerere and Weeks, 2005), and has become known as an instrument which allows acquisition of 3D, and non-destructive images; confocal microscopy is especially capable of controlling depth of field, which allows for the scrutinisation of thick specimen samples (Lange *et al*., 1993). Therefore a major limitation of light microscopes has been effectively dealt with by the instrument of confocal microscopy. Minsky had theorized that in order to get less haze and better contrast images that restricting the light from the specimen, but not from the microscope's focal plane is necessary. His devised concept became the fundamental basis of modern confocal microscopy.

2.2.1 Fluorescence

Fluorescence is a physical property that releases light with an altered wavelength after a substance absorbs light, which changes from the original wavelength.

The mechanisms of how fluorescence works are summarized below:

1. The wavelength (=colour of the light) is determined by the energy the photon obtains.

2. The ground state atom or molecule absorbs light (Figure 2.1-a) and a ground state electron moves to a higher energy, excited state (Figure 2.1-b).
3. The stored and surplus energy will be lost, and the electron is simultaneously dropped down to the conduction band edge (Figure 2.1-c).
4. As a result of the energy loss, the photon will emit at a longer wavelength (Figure 2.1-d), thus emitting a different colour (Figure 2.2); these photons will be the subject of the data will be collected during the fluorescence observation experiment.

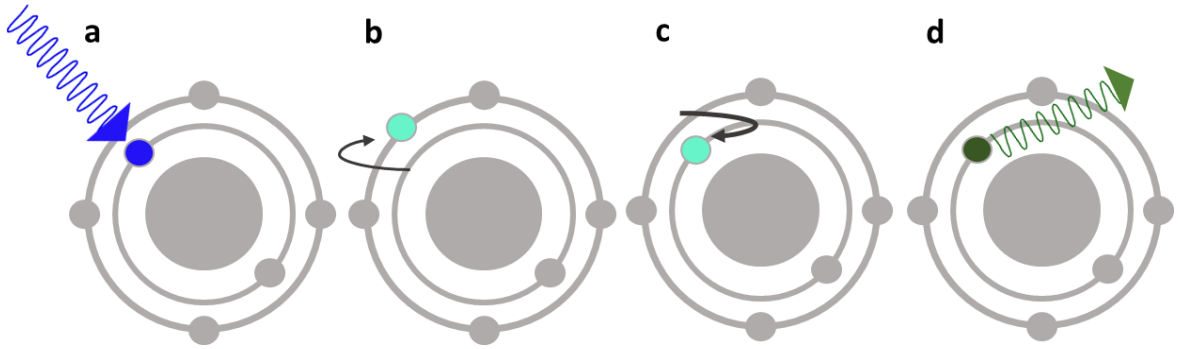

Figure 2.1: The interaction of photons and electrons to produce fluorescence phenomena. Adopted from King, (2020).

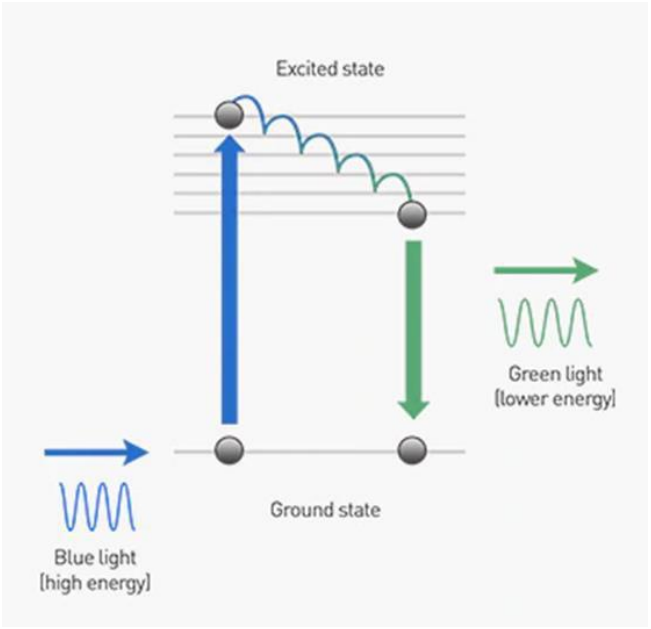

Figure 2.2: Simplified Jablonski diagram showing the change in colour and wavelength after light passes through the ground state. Taken from Thermofisher.com, (2019).

2.2.2 Mechanisms

The fundamental features of confocal microscopy, which are different from conventional

fluorescence microscopy are shown in Figure 2.3. The objective of confocal microscopy is to capture clear images without significant background haze. In other words, microscopy is required to capture the highest intensity of the excitation light (dark blue light), whereas it needs to attenuate the out-of-focus light (light blue light). To achieve minimizing and block the out-of-focus light, a pinhole aperture is installed in front of the light source to prevent inclusion of out-of-focus light as much as possible.

As shown in Figure 2.4, confocal microscopy uses two pinholes, which reduces background haze dramatically, compared to conventional fluorescence microscopy (Semwogerere and Weeks, 2005).

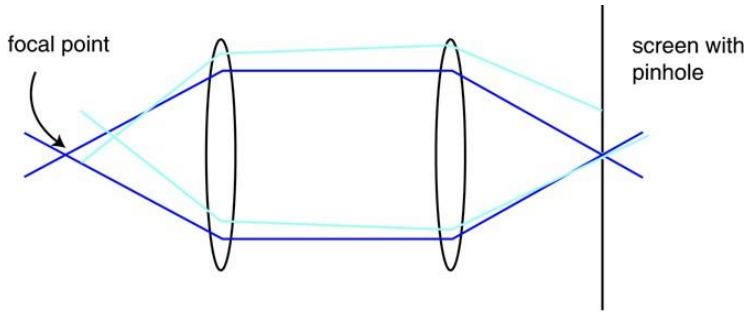

Figure 2.3: The blue lines show the highest intensity of the excitation light from the specimen; thus, the light is required to capture, and it is set up to passes through the pinhole. The light blue lines indicate the out-of-focus light, the passing of which through the pinhole is minimised. Taken from (Semwogerere and Weeks, 2005).

2.2.3 Setup

The standard configuration of a confocal microscope is shown in Figure 2.4. Intense excitation light emanating from the laser is subsequently reflected off a dichroic mirror. The light hits two vertical and horizontal scanning mirrors. The specimen is excited, and made to fluoresce and that fluorescent light travels back through the same way, descanned by the two scanning mirrors. The light passed through the dichroic mirror, focuses at the pinhole, and is measured by the detector.

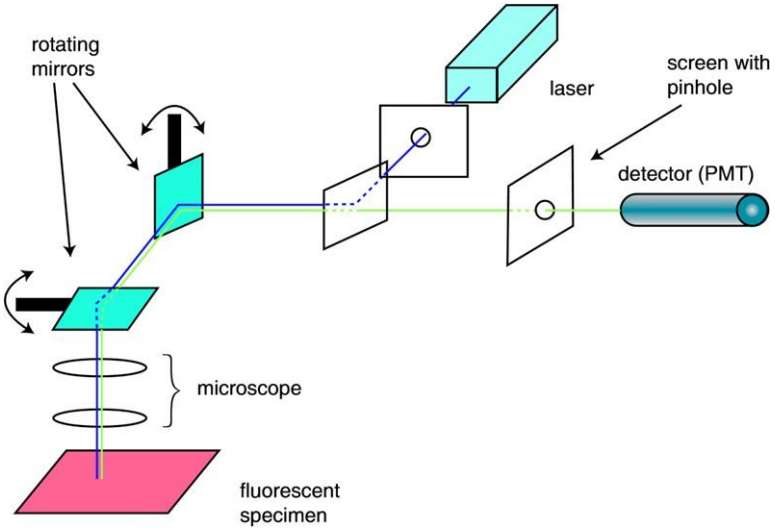

Figure 2.4 : The standard configuration of the confocal microscope. The blue line represents excitation light, whereas the green line represents fluorescent light (Semwogerere and Weeks, 2005).

2.2.4 Zeiss 800 with Airyscan

In this thesis, initial imaging of the samples was undertaken with the Zeiss 800 instrument. One of the outstanding features of the Zeiss 800 with Airyscan is its ability to capture high resolution images when compared to conventional confocal microscopy, which is possible with the Airyscan technology. The confocal microscopy is highly sensitive requiring short acquisition times which enables real time measurements. However, although the smaller pinhole increases the sharpness of the images, the decreased light also results in a decrease in fluorescent signal and, consequently, a disadvantage of this is that those images will be dimmer.

The Airyscan technology makes use of a detector system, called the "airy disk", which is concentrically arranged with a hexagonal detector array, configured with 32 single detector elements. The benefit of the airy disk is that by allowing the confocal pinhole to remain open and this enables the absorption of all photons, without rejecting much light in contrast to the conventional confocal images (Figure 2.5).

As Figure 2.6 shows, the 1st ring image, which was acquired from the internal 6 detector elements, resulted in an average light despite the relatively distinct and stronger signal provided at the centre. The 2nd and 3rd ring images were not as focused as these elements are further from the centre. Deconvolution of all the 32 detector elements was required, before digitally shifting the light to the centre element and aligning them together to form them into the reconstructed image.

This is an extremely practical technique which, when followed correctly, will allow for the efficient capture of higher resolution images with 1.7 fold improvement in 3-dimensions (ZEISS LSM 800 with Airyscan Your Compact Confocal Power Pack, 2015).

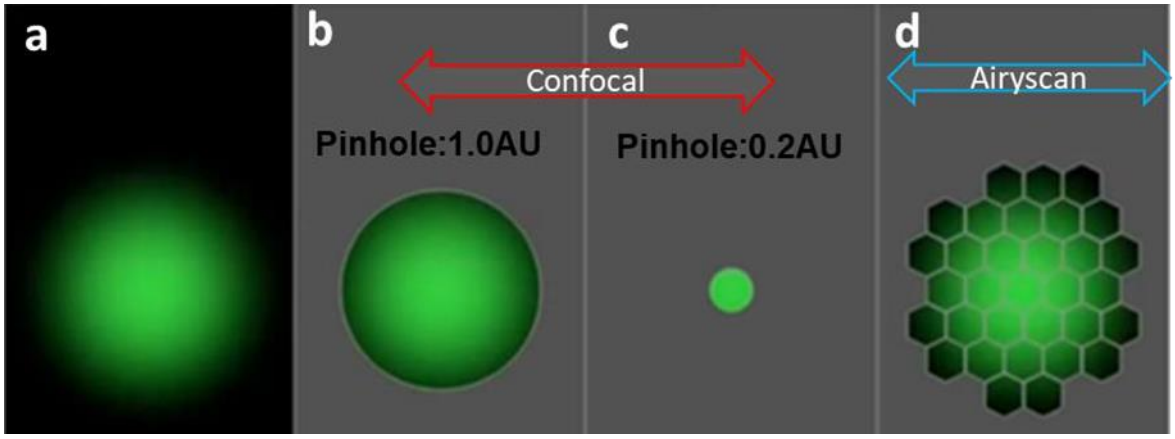

Figure 2.5: Showing how the Airyscan detects the light efficiently and overcomes a limitation of conventional confocal microscopy. (a) Emission of a point-like emitter (b) Confocal detection with a pinhole 1.0 a.u. (arbitrary unit). c) Confocal detection with a pinhole 0.2 a.u.. d) Airyscan detection; each hexagons detectors compare to a pinhole set to 0.2 a.u.. Taken from ZEISS Webinar: LSM 800 with Airyscan – Your Compact Confocal Power Pack, (2015)

Pawley (Pawley, 2010) mentioned that if very small pinholes (such as <0.1 a.u.) were created, it could improve the resolution of confocal images up to 40%, but this comes at the sacrifice of 95% of the signal. As pinhole (c) clearly depicts, most of the light has been cut off as compared to the larger pinhole (b). Thus, signal loss is more significant than the gain in resolution. In contrast, Airyscan detection (d) detects an entire signal with smaller a.u. detectors.

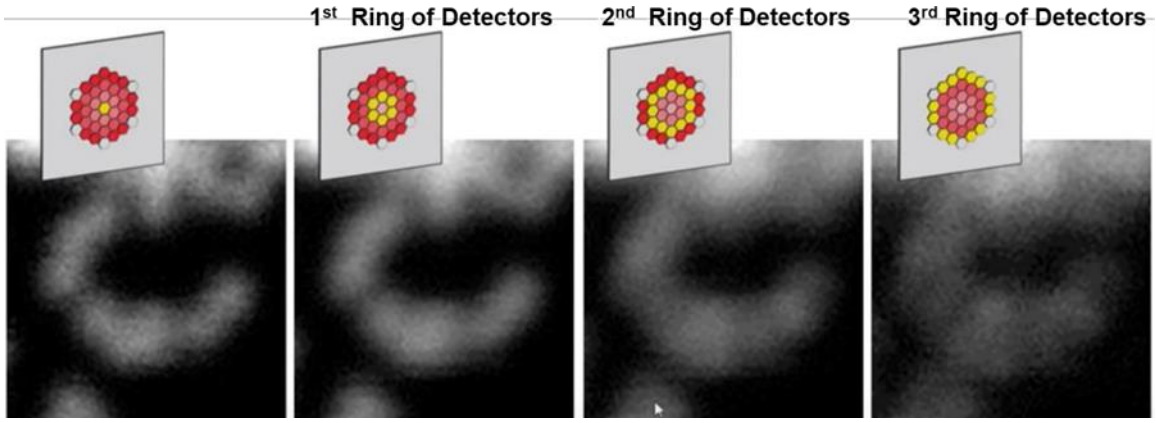

Figure 2.6: Showing the 1st to 3rd ring of detector (filled with yellow) that their resolution decreases further from the centre. Taken from ZEISS Webinar: LSM 800 with Airyscan – Your Compact Confocal Power Pack, (2015).

2.2.5 Total Internal Reflection Fluorescence (TIRF) Microscopy

TIRF is a form of fluorescence microscopy which provides exceptionally high axial resolution, which was established by Daniel Axelrod in the early 1980s (Ockenga, 2012); TIRF has a built-in evanescent wave which only illuminates near the interface. This local excitation wavelength is suitable to detect the low intensity light of a molecule from the fluorophores owing to the spatially restricted excitation wavelength, which significantly lessen fluorescence from outside the focal plane, as illustrated in Figure 2.7 (C&I Co., Ltd., n.d; Ross *et al.*, n.d; Iino, 2012). Due to the unique technique of limiting fluorescent molecules, TIRF allows for the capture of images with remarkably high axial resolution of below 100 nm, and is also capable of acquiring images with a significant signal-to-noise ratio (Ockenga, 2012). Although this instrument is commonly used in the field of biosciences

to observe membrane-associated processes (Ockenga, 2012) it is nevertheless suitable in application to this project, in the case of clay fluoresces due to the occurrence of fines migration commencing at the oil−brine−rock interfaces (Al Maskari, *et al*., 2019), also clay minerals would emit relatively delicate fluorescence intensity which is within the scope of the TIRF capabilities. In addition to that, TIRF is capable of capturing three-dimensional images which would provide a further understanding of fines migration. The Applied Precision OMX BLAZE Super-Resolution microscope supplied by GE Healthcare was employed for the project; Olympus TIRF 60x ApoN N.A. 1.49 for lenses, 488 nm for excitation laser line, and excitation FITC / GFP 461 - 493 nm, emission FITC 528 nm band pass 48 nm were applied for this study.

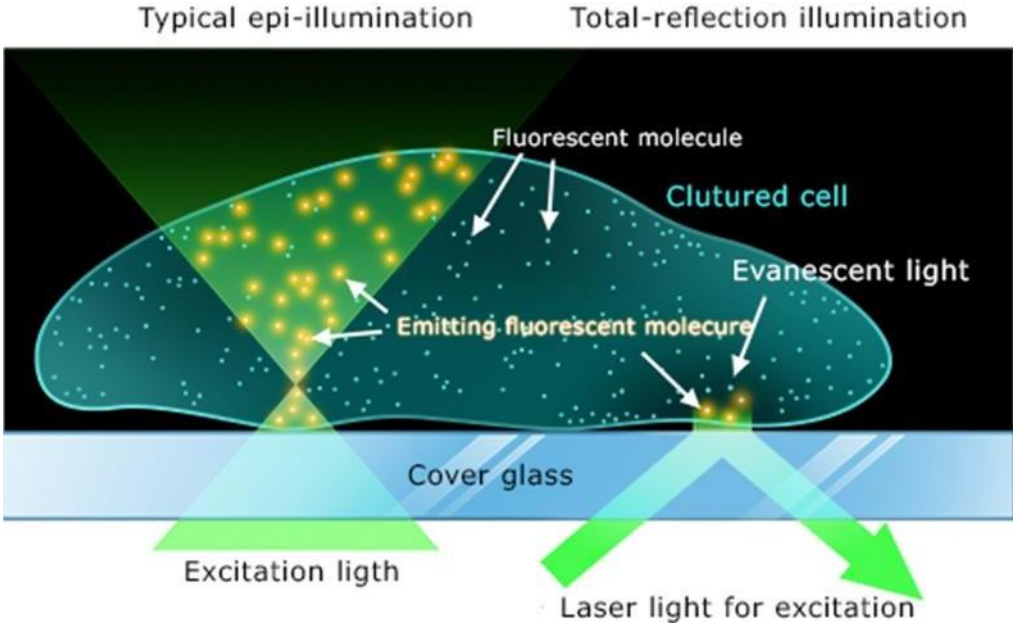

Figure 2.7: An illustration of the difference between a conventional fluorescence microscope and TIRF; the main difference is the illumination methods that conventional microscopes apply namely epi-illumination which causes illumination through the entire sample, whereas the TIRF employs evanescent light which only illuminates fluorescent molecules at the interface of the cover glass and the sample. Taken from (C&I Co., Ltd., n.d.)

2.3 Materials Used

2.3.1 Clay Minerals

As the following table briefly summarises, fluorescence intensity and their scope were scrutinised based upon the 8 clay minerals. The 7 clay minerals other than Na-bentonite were purchased from the Clay Minerals Society, Na-bentonite are from the Steetley Na-bentonite & Absorbents Ltd. Those 7 clay minerals from the Clay Minerals Society were relatively purified samples, which also provide further chemical and physical information as accessible (please also refer to Appendix 5). KGa-1b is low defect kaolinite that is well-crystallized minerals compared to high-defect kaolinite of KGa-2. 3 types of Mg/Fe LDH; Mg_2Fe, Mg_3Fe,

and Mg_4Fe, also 3 types of Mg/Al LDH; Mg_2Al, Mg_3Al, and Mg_4Al were additionally investigated in order to search for the cause of fluorescent factors of the previously mentioned 8 clay samples.

Table 2.1: Summary of 8 major clay samples that were tested for this project.

Offical Names	Origin	Group	Distributor
Na-bentonite DGM	Wyoming, USA	2:1 Smectite Group	Steetley Na-bentonite & Absorbents Ltd,
SWy-2	Wyoming, USA	2:1 Smectite Group	The clay mienrals society
SCa-3	Otay San Diego Country, California, USA	2:1 Smectite Group	The clay mienrals society
STx-1	County of Gonzales, State of Texas, USA	2:1 Smectite Group	The clay mienrals society
IMt-2	Silver Hill, Montana, USA	2:1 Micas	The clay mienrals society
CCa-2	Flagstaff Hill, El Dorado County, California, USA	2:1 Chrolite	The clay mienrals society
KGa-1b	Washington Country,Georgia, USA	1:1 Kaolinite	The clay mienrals society
KGa-2	Warren, State of Georgia, USA	1:1 Kaolinite	The clay mienrals society

2.3.2 Model Crude Oil

Creating 1 M model polar oil was achieved by mixing one litre of n-Dodecane supplied from Acros Organic and 176.26g of Decanoic acid from Sigma-Aldrich. n-Dodecane alone could also be used as model non-polar oil, see Table 2.2. The composition for the use of n-Dodecane and Decanoic acid for the making of synthetic model crude oil follows the guidance given by Kareem, (2016) (Table 2.2) and Santha (2019).

Table 2.2: Component properties of model crude oil. The amalgamation of Decanoic acid with n-Dodecane creates model oil more specifically model polar oil. The production of model crude oil requires polar components; these are essential as a replacement to crude oil. The significance of polar components within oil is expanded upon further in Chapter 1 (MIE)

Chemical Name	*Polarity*	*Chemical Formulation*	*Boiling Point*	*Density*
n-Dodecane	Non-polar	CH3(CH2)10CH3	215.0 ℃	0.7530 g mL−1
Decanoic acid	Polar	CH3(CH2)8COOH	269 ˚C	0.893 g/mL−1

2.3.3 Formation Water, High-Salinity Water, and Low-Salinity Water

Typical reservoir formation water (FW) composition used in flow experiments was provided by BP (Table 2.3); the composition was simplified to remove the necessity for minor ions. The definition of formation brine as for chemical compositions and properties, with a control factor of pH value, and salinity calculation are further mentioned in the book titled: 'Advanced Well Completion Engineering' (Renpu, 2011). With regards to high-salinity water (HSW) and low salinity water (LSW), the composition and ion concentration (Table 2.3) were from the paper written by Morishita *et al*. (2020).

Table 2.3: The ion concentration (mg/L) applied in this instance. The properties of ion concentration for both formation water (FW) and high salinity water (HSW) have a slight inconsistency than that of the original. However, the gaps are negligible.

	FW	HSW	LSW
Na^+	8101	11345	1/30 of HSW
Ca^{2+}	348	441	
Mg^{2+}	147	1075	
K^+	2383	439	
Cl^-	15703	20373	
SO_4^{2-}	—	1990	

2.4 Methodology for Sample Preparation

2.4.1 Non-Aged Samples for Confocal Microscopy

1 g of as received clay mineral powder was added into a 1.5 ml microcentrifuge tube and filled with tap water, brine, or crude oil until it reached to slightly above the 0.5 ml line (Figure 2.8 a). The microcentrifuge tubes were mixed using a Vortex shaker for 10 to 15 seconds (Figure 2.8b).

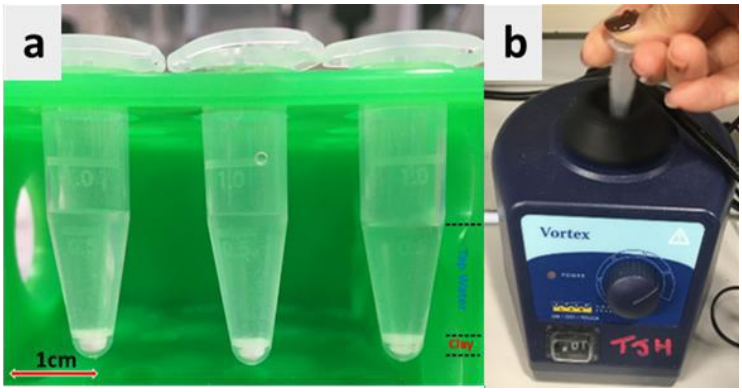

Figure 2.8: (a) non-aged samples were placed in the microcentrifuge tubes showing the approximate quantity of clay samples and tap water; the same amount for brines and crude oils were applied. (b) Blending clay particles and tap water. The method is conducted because some clay samples were immobile and deposited due to the swelling of clay minerals which happened immediately after water was poured into the microcentrifuge tubes.

2.4.2 Aged Samples

Petroleum reservoirs are situated a few kilometres underground, and the temperature increases depending on the geothermal gradient of the located reservoir. Hence, the petroleum reservoir temperature depends on the depth and the location of the reservoir. (Lovering and Goode, 1963; Kargarpour, 2016).

On the basis of this knowledge, two types of crude oils and clay samples were aged as the first step of understanding fines migration under typical sandstone reservoir conditions.

0.2 g of clay samples were prepared and 3 ml (approximately 3 g) of crude oil. The samples were mixed well using a small spatula after which they were placed in small glass bottles (Figure2.9 a). These samples were aged in an oil bath for 3 days at 70 ℃ (Figure 2.9 b), then aged another 2 weeks under room temperature. The samples were mixed again before placing them on glass slides; the observation methods were the same as with the non-aged samples.

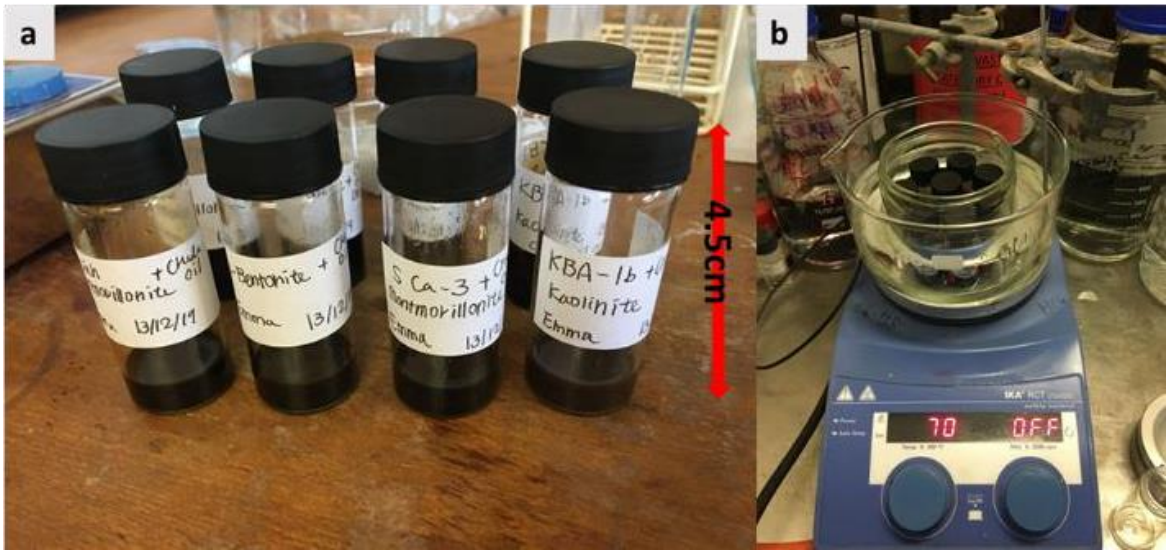

Figure 2.9: (a) clay minerals and crude oil are in the labelled glass bottles. (b) The samples along with the silicon oil were heated at 70 °C on the hot plate.

2.4.3 Total Internal Reflection Fluorescence Microscope (TIRF) Sample Preparation

TIRF experiments were undertaken in specific TIRF cells, obtained as 'µ-Dish 35 mm, high Glass Bottom', purchased from Ibidi, to observe fines migration. The steps for preparing TIRF samples were:

1) Immersion of clay samples with formation brine. Initially, 0.5 ml of formation brine and 0.05 g of clay powders which fluoresced to a high enough intensity were well mixed by the orbital shaker for 15 minutes at a speed of 560 rpm; this procedure is required for clay particles to be well distributed in the solution. KGa-1b, Na-Bentonite, and IMt-2 to each µ-Dish. The proportion of clay powders and formation water was based on the protocols from research undertaken by Santha (Santha *et al*., n.d.).

2) Aging process. Clay samples immersed in formation brine were placed in the oven at 70 ℃ for three days, with a lid in order to stop the solution evaporating.

3) Immersion of clay samples with model crude oil. 0.5 ml of model crude oil was added into formation brine-coated clay samples in order to coat another layer of model crude oil.

4) Aging process. Finally, clay samples coated with formation brine and model crude oil were placed in the oven at 70 ℃ for a week with the lid in place (Figure 2.10).

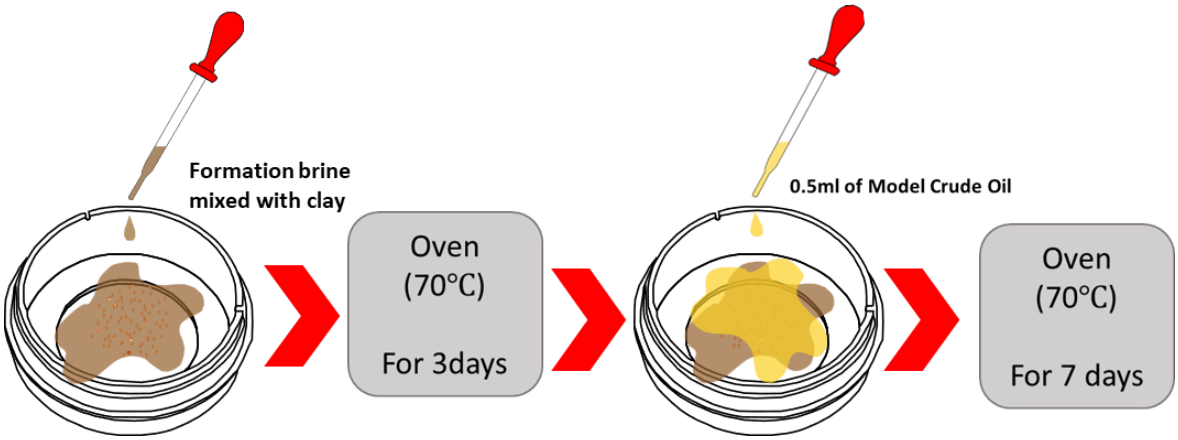

Figure 2.10: Showing each step for preparing TIRF samples. Further details of 'µ-Dish 35 mm, high Glass Bottom' can be found from the website (µ-Dish 35mm, high Glass Bottom | High Quality Imaging | ibidi, 2020).

2.4.4 Scanning Electron Microscopes (SEM)

Sigma 300 VP and Evo Analytical Scanning Electron Microscopes were employed to observe the chemical and structural features of the clay minerals used, in order to aid understand the reason for the fluorescence of clay minerals.

1. In order to prevent cross-contamination between the different clay mineral samples, each type of clay mineral sample which was tested was placed in its own small individual glass vial and then dispersed in $(CH_3)_2CHOH$ (isopropyl alcohol, IPA) , then sonicated for 10 mins. The sonicated solution was pipetted or drop casted on to a clear polycarbonate disk.
2. An Au/Pd sputter coating process was carried out with Cressington Sputter Coater 108 Auto in order to acquire high-quality SEM images. These samples, mounted on aluminium stub were only utilized for observing the structure of clay minerals. In contrast, chemical analysis required resin sample pucks and carbon coating.

2.4.5 Atomic Force Microscopy (AFM)

1 cm by 1 cm glass slides were cleaned in order to ensure the slides were grease-free, using an ultrasonic bath (Ultrawave QW5; 100% power, no heating, frequency leap on) ahead of time. The clean slides were coated with a first layer which would be either with a solution of clay mineral and brine or clay mineral and model oil. The procedure, shown in Figure 2.11, was as follows: 1) the glass slides were cleaned with washing up liquid and tap water before, 2) being placed in the ultrasonic bath in a beaker of high purity water for 5 minutes. 3) After drying with a clean paper towel, the slides were placed in an ultrasonic bath in a beaker of acetone, of >99.8% purity, for 5 minutes. The acetone was purchased from Fisher Scientific. 4) After being dried with a clean paper towel, the slides were placed in ultrasonic

bath in a beaker of high purity water for 5 minutes, 5) dried again with a clean paper towel, then placed in an ultrasonic bath in a beaker of ethanol., absolute (>99.8%) for 5 minutes. The ethanol was also purchased from Fisher Scientific. 6) The glass slides were then stored in ethanol until ready for use, subsequently dried on a clean paper towel before use.

A solution of clay minerals and formation brine mixed in the same amount as the TIRF sample were placed on the cleaned glass slides. The preparation of the clay film on the glass slides is illustrated in Figure 2.12.

The prepared glass slides were affixed to a steel disc using epoxy glue, and all the samples and the silicon nitride cantilevers were immersed entirely in high salinity brine (200 µl), followed by low salinity brine (200 µl). See Table2.3 for the composition of the brine. The AFM was a commercial Cypher ES AFM (Oxford Instruments, Santa Barbara, CA, USA). Since the samples were significantly brittle and with a strong affinity for the cantilevers, the experiments utilised silicon nitride cantilevers (Olympus RC800 PSA, Olympus, Tokyo, Japan) which were chosen after trials with several different models, so as to optimise the imaging conditions. The nominal flexural spring constant was kf = 0.10 N m^{-1}, also each cantilever was calibrated using its thermal spectrum yielding a typical stiffness of 0.15 (±0.05) N m^{-1} in solution. Imaging of the interface was conducted operating the AFM in amplitude modulation using acoustic excitation. Friction force microscopy (FFM) imaging was performed in contact mode, recording the lateral torsion of the AFM tip as a function of a given normal force.

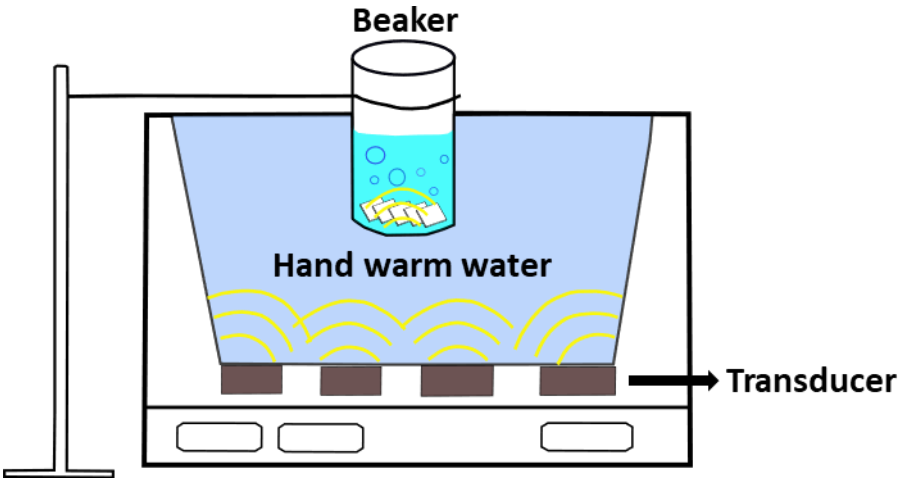

Figure 2.11: The experimental set up of ultrasonic bath in a beaker to clean the glass slides; I have digitally reconstructed this from the image taken from Fındık (Fındık, 2018). The instruction manual is publicly accessible in PDF format (Ultrawave Precision Ultrasonic Cleaning Equipment, 2004).

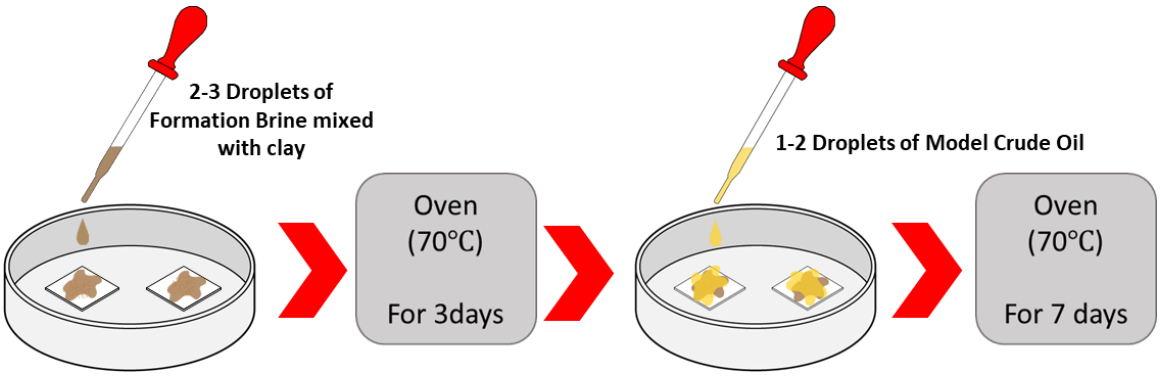

Figure 2.12: The figures depict the procedure of constructing clay film on the 1cm × 1cm glass slides to be examined under the AFM.

2.5 Applied Laser

Both confocal microscopy and the TIRF have the same set lasers; an excitation wavelength of 493 nm, the emission wavelength of 517 nm, and detection wavelength of 490-700nm. These were determined as the optimum lasers after trying out various lasers, and testing the quality of the resulting fluorescence images.

2.6 Imaging samples with the Zeiss 800

Pipette tips were renewed each time the samples were changed so as to avoid cross-contamination, and 2-3 droplets were placed on the microscope glass slides. Each sample was covered with a slide cover on the glass slide and the space between the glass slides and cover slides were sealed by nail polish to avoid the samples leaking and contaminating the microscope lenses. Nail polish is easily-obtainable for use in sealing these gaps and its quick drying properties proved effective. The prepared glass slides (Figure 2.13) were observed under the confocal microscope, Zeiss 800 with Airyscan. One droplet of immersion oil were placed on top of the cover slide to create an oil column between the lens and the sample. Afterwards, the sample was examined through a microscope and the position of the sample adjusted again on the affiliated computer screen to locate the most substantial fluorescent part — this method was repeated after cleaning the lens with 70% ethanol.

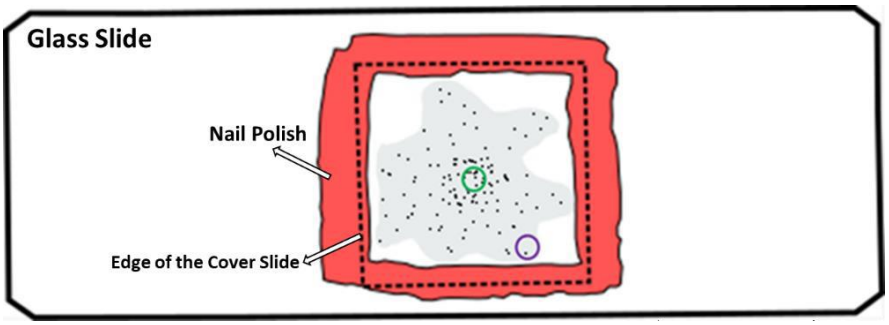

Figure 2.13: Illustration of the prepared glass slide displays that there was difficulty in controlling the clay concentration; the green and purple cycles illustrate the approximate area that can be captured in one image. Inside the green cycle which is located in the centre of the glass slide, a large number of clay particles can be captured. In contrast, the purple circle, which is located at the edge of the glass slide is not able to capture as many clay particles. The difference in clay concentration in each image is practically impossible to control

2.7 Data Processing

2.7.1 Quantifying Average Fluorescence Intensity and Fluorescence Scope

In order to compare the fluorescence micrograph of nine different clay samples, micrographs acquired from confocal microscopy were quantified in terms of optical and fluorescence intensity (Table 2.4). The fluorescence microscope allows the fluorescence to manifest the intensity of each pixel within a certain range thus, calculating an average fluorescence intensity of an image, the number of pixels was multiplied by the fluorescence intensities respectively; and after adding them all, the fluorescence intensity of the image was then divided by only the pixels that displayed fluorescence. Moreover, in order to quantify the fluorescent scope of the image, the number of fluoresced pixels were then divided by the total pixels of the micrograph; this number can be provided as percentages of the fluoresced scope of each micrograph. The range of lowest fluoresced intensity that the software can provide is between 0 to 255, all pixels that fluoresced within this range were dismissed. In addition to that, images which did not fluoresce more than 256 intensity were also disregarded. This procedure was undertaken because, although determining what caused clay minerals to fluoresce differently is intriguing, it is more critical to detect the presence of clay minerals under the confocal microscope to observe fines migration.

Table 2.4: The table shows how the fluorescence intensity was quantified, and the fluorescent scope of micrographs. The range of fluoresced intensity and number of pixels were provided from the fluorescence microscope. In this instance, the average fluorescence intensity of the micrographs is approximately 442.56 (a.u.), also 2.34% of the total area showed fluorescence. As confocal microscopy provides nano-scale micrographs, capturing the exact quantity of clay particles in each image is not feasible. Hence, nine micrographs from three different glass slides were acquired to provide more precise results.

Intensity	Number of Pixcels	Intensity × Pixcels	
0	3199282	0	
256	36551	9357056	
512	26534	13585408	
768	11915	9150720	
1024	1655	1694720	
1280	163	208640	
	76818	*33996544*	*442.5596084*
	3276100		*0.023448002*

SUM

SUM

SUM

Chapter 3 Characterisation of Fluorescence in Layered Minerals

3.1 Fluorescent of Experimental Equipment and Brines

3.1.1 Fluorescence of Tap water and Glass

Fluorescence of water, glass slides, and cover glass were initially studied. The intensity of fluorescence of the water and a set of the glass slide and cover glass were observed to be negligible in the samples studied (see Table 3.1). The examined tap water was acquired from the bioscience laboratory in Durham. Fluorescence of the glass slides and cover glass may be affected by either process technology or the use of higher purified raw materials (TIE-36: Fluorescence of optical glass, 2010). To sum up, it was found that the fluorescence intensity of tap water and glass slides are negligible; however, it is better to exclude intensity below 200 to rule out extraneous variables.

Table 3.1: (Top) The maximum intensity which is provided from ZEN software (ZEN3.1 Blue edition); source of tap water: Durham University Department of Bioscience, laboratory room 137/138. (Bottom) tested fluorescence of cover glass on top of glass slide. Glass slide: Academy Microscope Slide 76x26mm, thickness 1.0-1.2mm. Cover glass: Precision cover glasses thickness No. 1.5H (22×22 ㎜)

Tap Water	Sample 1	Sample 2	Sample 3
Maximum Intensity/a.u.	18	15	19

Glass Slide + Cover Glass	Sample 1	Sample 2	Sample 3
Maximum Intensity/a.u.	122	129	163

3.1.2 Fluorescence of Brines

Data from each of the 6 different salinity levels (9 replicates for each) were obtained in order to compare their maximum fluorescent intensity based upon the hypothesis that brines of higher salinity, and thus higher ion contents, may exhibit higher fluorescent intensity than brine with lower salinity and correspondingly less ion content. Although there were a few outliers for NaCl and $CaCl_2$, no correlation between salinity levels and fluorescent intensity was found, and fluorescence intensity levels were relatively uniform at all the salinity levels. Thus, although Moses, (1963) and Rost, (1995) stated that the presence of calcium ameliorates fluorescence, this was not clearly evidenced from the test which was undertaken (Figure 3.1). In addition, the increment of sodium and chloride did not show changes in fluorescence intensity. The average-maximum intensity was slightly increased after adding the clay minerals, though there was no correlation between the maximum intensity observed and the different salinity levels in the presence of clay minerals (Figure 3.2).

After finding that there was no relationship between salinity levels and the strength of fluorescent intensity, KGa-1b (low-defect kaolinite) with water, KGa-1b with 0.5 M brine, and KGa-1b with 1.5 M brine were observed. The average-maximum intensity slightly increased after adding clay minerals, though there are no characteristic inclinations between maximum intensity and the different levels of salinity with clay minerals [see Appendix1]. The test appears to suggest that the clay mineral itself, KGa-1b in this case, fluoresces more than the brines showing that imaging of the clay minerals under the brine should be possible.

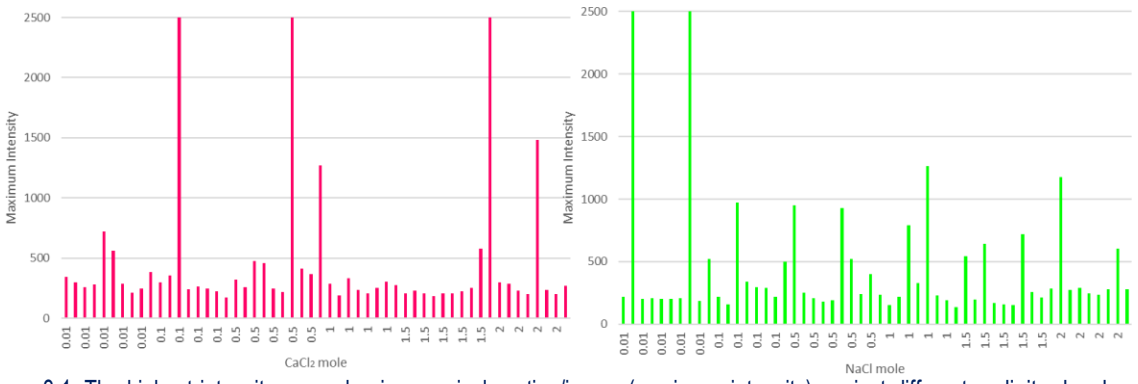

Figure 3.1: The highest intensity on each microscopical section/image (maximum intensity) against different salinity levels of brines.(Left) $CaCl_2$ (Righ)NaCl

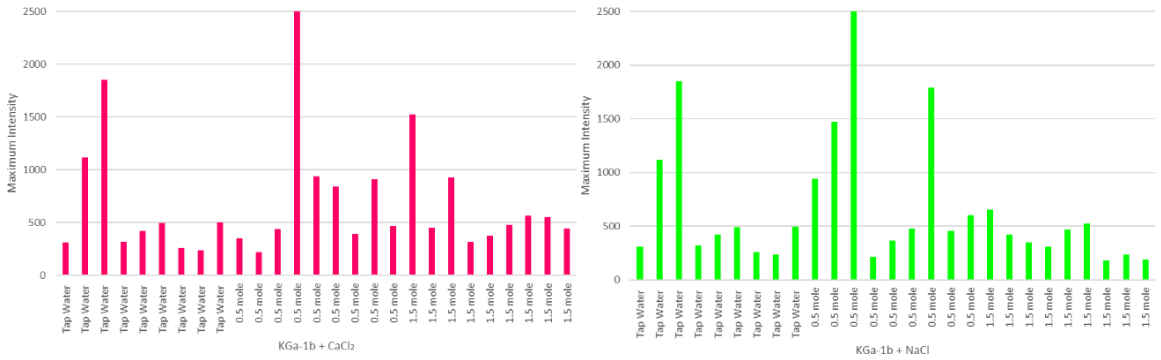

Figure3.2:Thehighestintensityoneachmicroscopicalsection/image(maximumintensity)vsdifferentsalinity levels of brines and KGa-1b. (Left) $CaCl_2$ (Right)NaCl

3.2 Fluorescent of Crude Oil

3.2.1 Fluorescence Properties of Different Crude Oils

Two types of crude oil were employed; the first was a black, heavy crude oil, which was provided from BP (denoted BP crude oil), and the second a brown, light crude oil from Hardstoft (Hardstoft crude oil). The latter is where the existence of the first successfully conducted "oil exploration well", in the UK was drilled (Craig *et al.*, 2013). After some tests, the most effective 488 nm laser wavelength [see Appendix 2] was employed to test both types of crude oil. The BP crude oil fluoresced with an intensity between 1024 and 6144, while the Hardstoft crude oil gave an intensity between 3840 and 5888 (see Figure 3.3).

Despite the fact that the two crude oil types have different physical features in terms of viscosity and colour, the fluorescent intensity is not as different as might be expected. Polyaromatic hydrocarbons, are known for being the most dominant fluorescent substance in oils, they would be the fluorescing species for these two types of crude oils. Further oil analysis is required to determine the assumption.

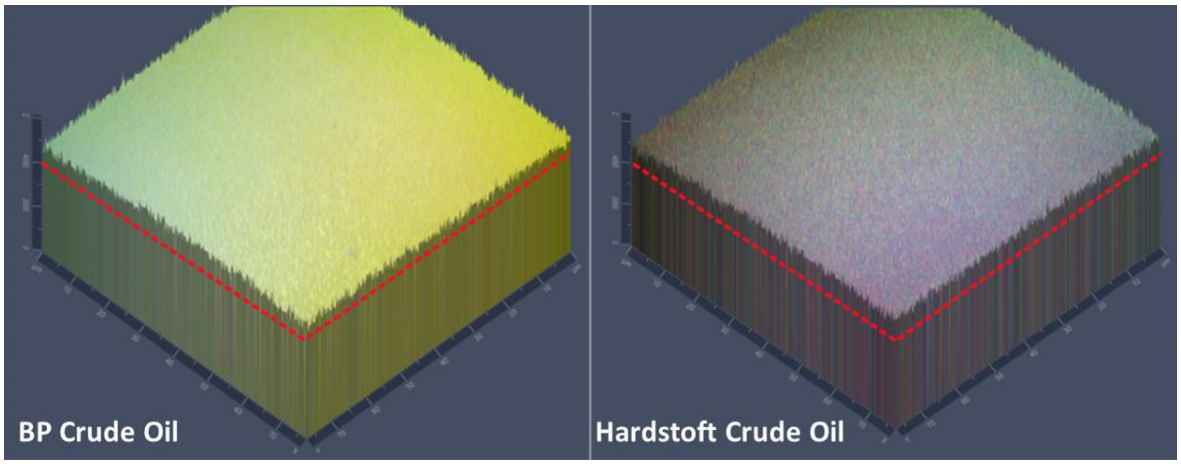

Figure 3.3: 2.5D fluorescent images of BP crude oil and Hardstoft oil; both heavy and light crude oil exhibited more than 4000 relative intensity from entire pixels. The red dashed-line is representative of fluorescence intensity of 4000.

3.2.2 Clay Samples with Crude Oil

Since crude oil fluoresces approximately 8 times stronger than the average intensity of clay minerals (Figure 3.3 and Figure 3.6), the background showed bright green when clay samples were mixed with highly fluorescing crude oil, whereas the background of the image became dark when the fluorescence of bentonite clay samples was tested with either water or brine (Figure 3.4a), thus the intensity of clay samples were overlain and saturated by the intensity of the fluorescence from the crude oil, and this triggered the high background intensity as seen in Figure 3.4b and Figure 3.4c). In particular, KGa-1b particles swelled to approximately 2.6 times (the average particles sizes for non-aged KGa-1b were 0.467 μm, and for aged KGa-1b were 1.227 μm) after ageing the sample for 3 days at 70 °C, followed by 2 weeks at room temperature, when imaged under the confocal microscopy. This swelling of the KGa-1b, along with potential dispersion of KGa-1b, lead to difficulty in imaging the presence of clay minerals within the crude oils. This would prove to be a hindrance in allowing tracking their migration in the next phase of work, using the TIRF instrument. To address this, it was decided to also test amodel crude oil that fluoresces less than but also maintains some physical features of crude oil (Santha, 2019).

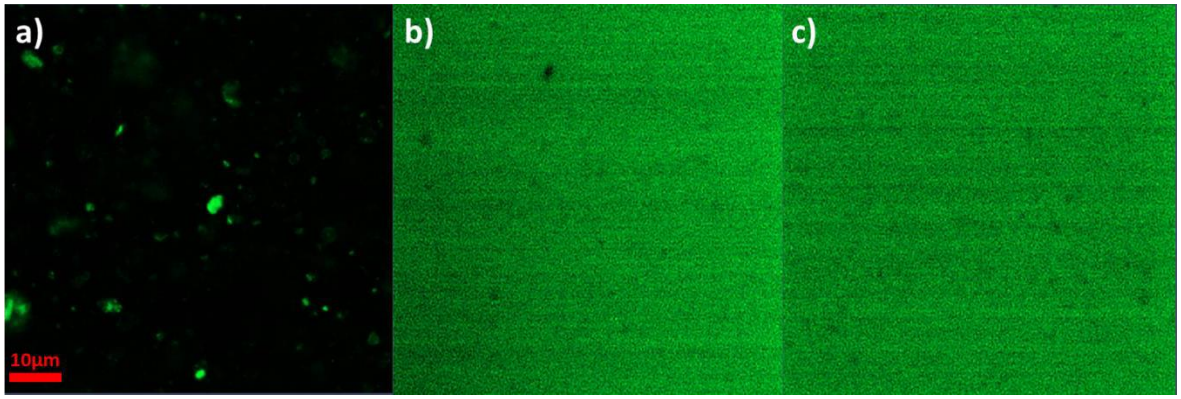

Figure 3.4: a) Na-Bentonite with water. b) Non-aged Na-Bentonite with crude oil c) Aged Na-Bentonite sample with crude oil. For b) and c), these fluorescence images with high fluorescence were most commonly captured from all the types of clay samples with crude oil whereas a) is clearly showing the presence and location of clay minerals. In particular, the presence of aged Na-Bentonite is scarcely conspicuous in (c).

3.3 Fluorescent Properties of Model Crude Oil

Through utilising a model crude oil, detection of the presence and the location of clay minerals should be possible, while still obtaining physical and chemical properties of crude oil such as viscosity, wettability, and polar components. As aforementioned in Section 3.2, 'Clay Samples with Crude Oil', the fluorescence of model crude oil was tested to confirm whether or not it prevents the fluorescence image being saturated and allow contrast between the clay mineral and the oil fraction such that individual clay particles/aggregates can be discerned. As Figure 3.5 presents, the linear alkane/carboxylic acid model oil (decanoic acid in dodecane) with no aromatic groups has a very low fluorescence compared to the crude oils in Figure 3.4 b and c; for the polar and non-polar model crude oil components the average maximum intensity was 122 a.u. and 140 a.u., respectively [see Appendix3]. Furthermore, the appearance of fluorescent images of KGa-1b with water, and KGa-1b with the model crude oil are indistinguishable, thus firmly applicable for studying the migration of clay minerals with TIRF.

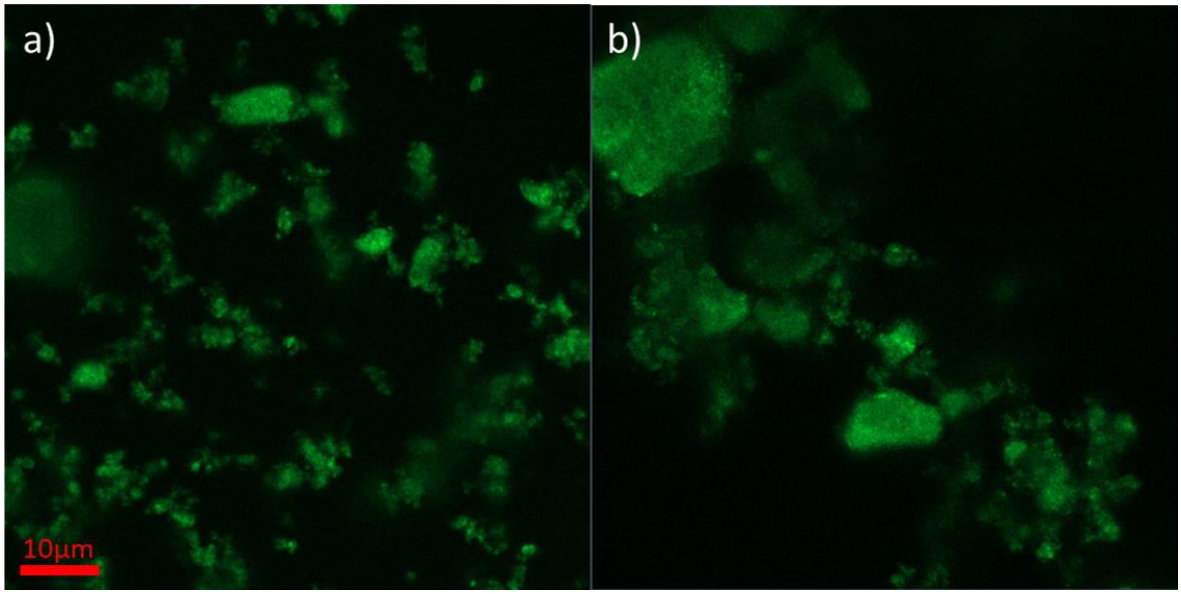

Figure 3.5: The fluorescent images of a) KGa-1b with polar model crude oil and 2) KGa-1b with tap water. In terms of the image quality, there are no substantial differences in fluorescence between a) and b)

3.4 Fluorescence Intensity and Fluorescence Scope of Different Clay and Layered Mineral Samples

3.4.1 Kaolinite, Smectite, Illite, and Chlorite Group

Four samples from the smectite group and a sample from each of the kaolinite group, illite group, and chlorite group of clay minerals were scrutinized to compare their exhibition of autofluorescence. Figure 3.6 shows the average intensity of each fluorescent image, whereas Figure 3.7 represents the fluoresced scope of each of the fluorescence images. The purpose of obtaining the two types of data is mentioned in the methodology part in Section2.3.1 'Quantifying Average Fluorescence Intensity and Fluorescence Scope.' Na-Bentonite recorded the highest, and broadest scope of average intensity, while KGa-1b demonstrated the lowest average fluorescent intensity, yet exhibited the second largest fluorescence scope, thus exhibiting the clearest fluorescence image following Na-Bentonite. Accordingly, the percentage of illuminated pixels shown in Figure 3.4 is not necessarily proportional to the fluorescence intensity. This is demonstrative of the fact that, fluorescence images of KGa-1b were brighter and better resolved than the majority of the clay samples, despite KGa-1b exhibiting a lower average fluorescent intensity. The most critical requirement for fines to be tracked by the TIRF is its ability to visually confirm the presence of fluorescing fines under confocal microscopy, thus fluorescence of larger numbers of pixels is more important than recording higher average fluorescence intensity. As a result of these considerations, the three most promising clay samples as applicable for TIRF experiments were deemed to be

Na-Bentonite, KGa-1b, and IMt-2(Illite).

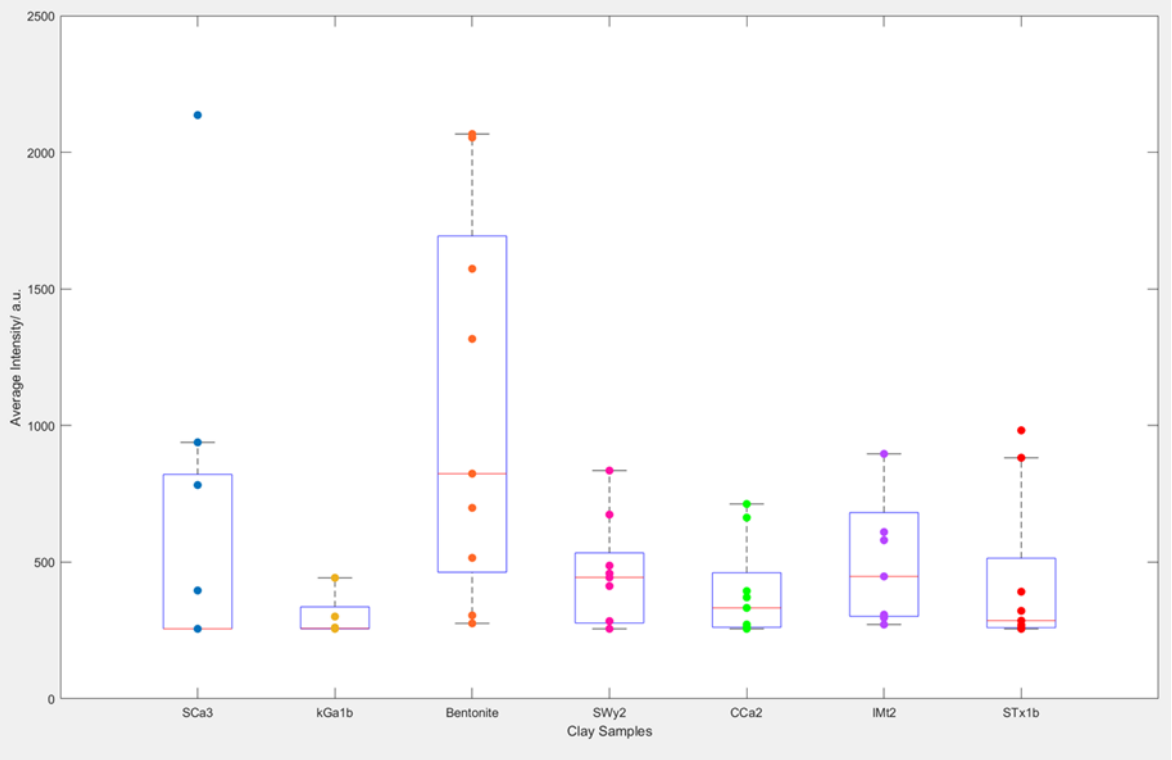

Figure 3.6: Average intensity of fluoresced pixels; each dot represents the average intensity of fluoresced pixels per image. Fluorescent images which do not fluoresce more than 256 intensity were dismissed. (SCa-3) Montmorillonite (KGa-1b) low-defect kaolinite (SWy-2) Na-rich montmorillonite (CCa-2) Ripidolite (Chlorite) (IMt-2) Illite (STx-1b) Texas Montmorillonite. For SCa-3, SWy-2, CCa-2, IMt-2, and STx-1b, majority of fluoresced images falls in less than 1000 relative intensity though the bulk of STx-1b are prone to fluoresce less than 500 relative intensity. Each box and whisker plots describe the range of fluorescence intensity for each clay mineral; The fluorescence intensity of KGa-1b fits within a specific range (256-500) thus exhibited similar intensity every time KGa-1b was tested. Diversely, the fluorescence intensity of Na- Bentonite dispersed in the range between 256 to 2000, which means that almost every image showed different fluorescent intensity.

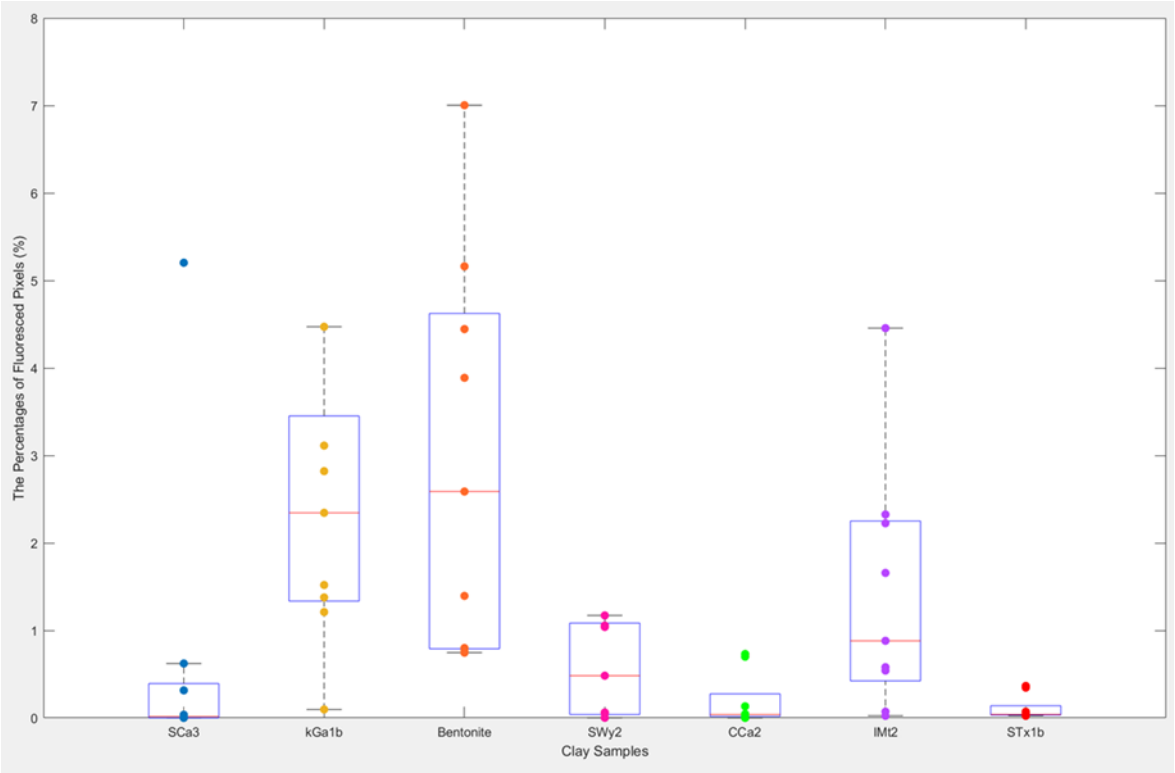

Figure 3.7: The graph shows the average percentages of fluorescence scope; each dot represents the percentages of fluoresced pixels per image and the box and whisker plots describe the range of the plot. Na-Bentonite showed the highest percentages of fluoresced pixels per image as it corresponds with the trend of the strength of fluorescence intensity. In contrast, kaolinite (KGa-1b) which is the second most widely fluoresced clay sample recorded the lowest fluorescence intensity; thus, the intensity of clay minerals is not always proportional to the visibility of fluoresced images. The values are directly related to the degree of visibility of the presence and location of clay samples.

3.4.2 Fluorescent Properties of High Defect Kaolinite vs Low Defect Kaolinite

Figure 3.8 illustrates the average fluorescent intensity of high-defect (KGa-2) and low-defect (KGa-1b) kaolinite. Despite the average-intensity of high-defect kaolinite and low-defect kaolinite being comparable, low-defect kaolinite was considerably higher in fluorescence scope, which is indicative of a broader number of low-defect kaolin particles having fluoresced with reasonable intensity, mostly around 256 a.u. to 300 a.u. In contrast, the high-defect clay exhibited well distributed intensities, and this increased the overall average. Isolated large fluorescence intensities from high-defect samples could be due to the fluorescence of non-clay mineral impurities, and, as such, low-defect kaolinite fluoresced more than the high-defect kaolinite (Figure 3.9).

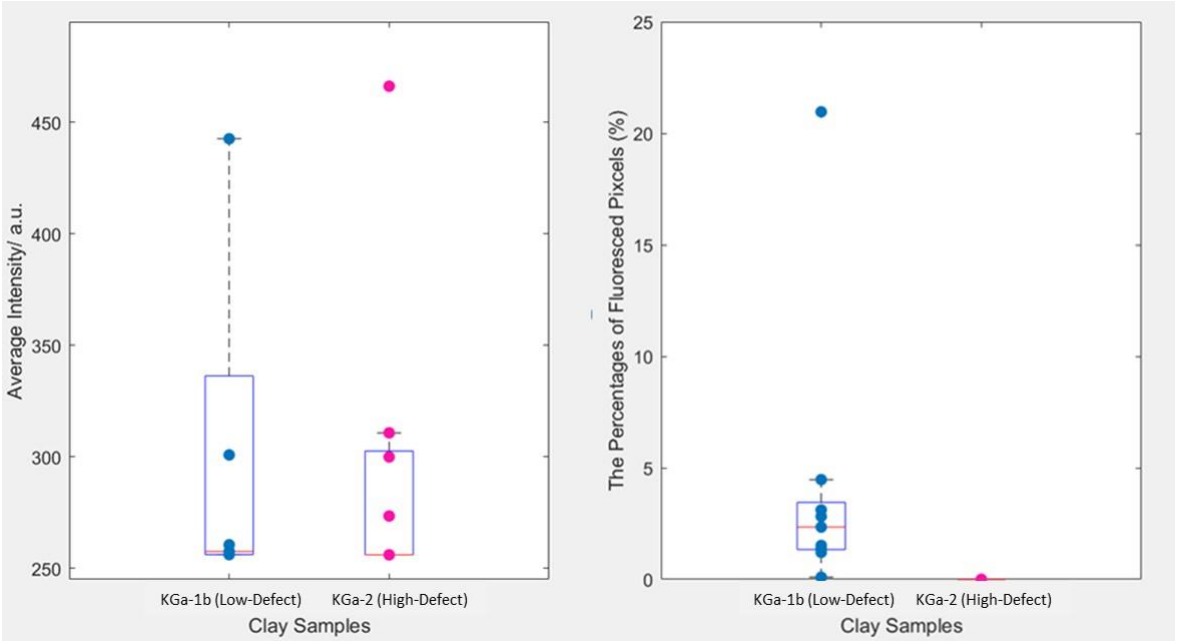

Figure 3.8: (Left) Average-fluorescent intensity of low defect and high defect kaolinite. (Right) The average- percentages of fluoresced pixels per image. The emphasis is upon plot dots rather than the box plots; majority of KGa-1b fluoresced just above 256 intensity as well as showing fluorescence to a reasonable certain scope. Furthermore, fluorescent intensity of KGa-2 mainly fits within the range between 256 and 300 which is more or less comparable with KGa-1b, however, its fluoresced scope is nearly zero.

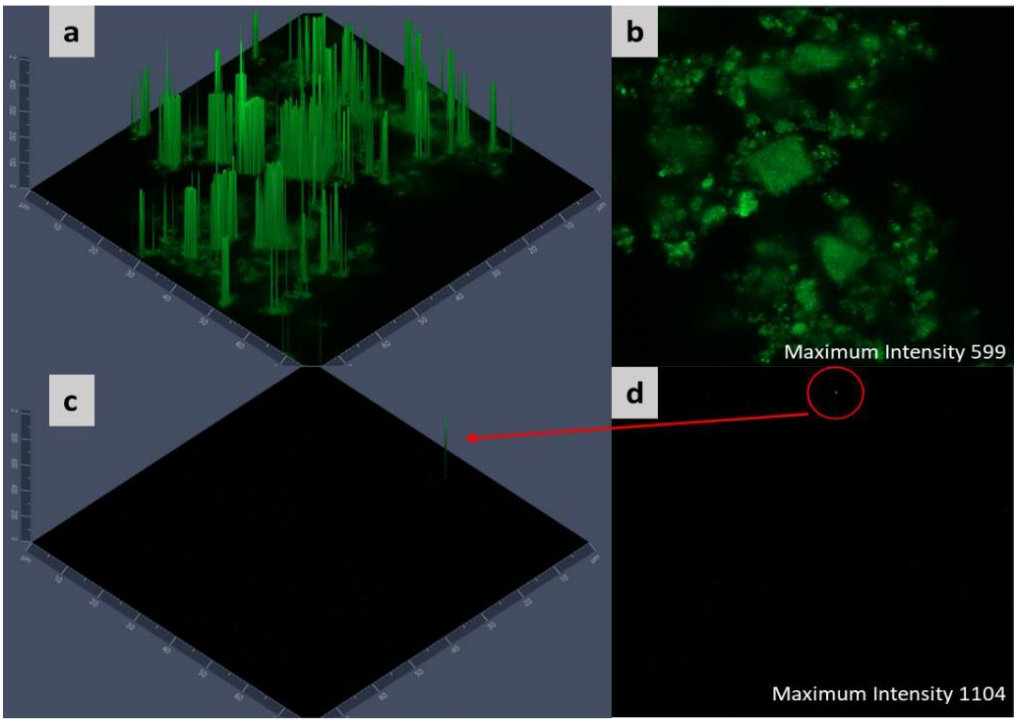

Figure 3.9: (a)(b) fluorescent images of low-defect kaolinite, mixed with tap water (KGa-1b). (c)(d) fluorescent images of high-defect kaolinite, mixed with tap water (KGa-2). (a) and (c) are showing which part of the image is fluorescent and with what intensity (b)(d) 2D images of (a) and (c). Since confocal microscopy focus on the highest part of the images, the inclusion of extremely-highly fluoresce substances might disturb the visibility of clay samples; inside of the red circle there might be some impurity which fluoresces with exceptionally high intensity.

The low/high defect kaolinite nomenclature was originally used to describe well-crystallised and poorly crystallised kaolinite, respectively, by R.E. Grim (1953). This was subsequently altered to describe well-ordered or poorly-ordered kaolinite samples, which is currently preferred by mineralogists (Kogel *et al.,* 2006). This crystallinity depends on the absence or presence of stacking faults between kaolinite layers and it is this which leads to differences in the kaolinite properties.

Both high defect and low defect clay samples were purchased from the Source Clay Repository of the US Clay Minerals Society. Subsequent X-ray diffraction analysis, including quantitative clay mineral, by a commercial provider (X-Ray Mineral Services Ltd of North Wales)indicated there was no significant difference in composition and amount of impurity between the high and low defect kaolinites. However, it should be noted that detecting the presence of high-defect kaolinite under confocal microscopy proved challenging as compared to low-defect kaolinite though the maximum fluorescence intensity of high-defect kaolinite was markedly higher; this result is also shown in Figure 3.9. Due to the fact that one of the reasons for fluorescence to occur in minerals is through crystal structural defects (King, 2020), the results recorded from high-defect kaolinite were expected to be higher in fluorescence intensity and wider, or similar in scope, to the fluoresced area when compared with low-defect kaolinite.

In general, visible fluorescence is rarely observed in minerals, especially clay minerals, due to most minerals having a wide band gap between the valence and conduction bands, and are thus typically insulators, thus emitted light will occur outside the visible light range of EB > 3.2eV (Li et al., 2001; Nassau, 2021).

Therefore, it can be presumed that the recorded extremely high fluorescent intensity from high defect kaolinite is due to the fact that elemental defects might be included within the composition of the clay mineral, and splitting of the electron orbitals will lead to a reduction of the band gap thus making it possible to observe fluorescence of this clay optically (Nassau, 2021), as shown in Figure 3.10.

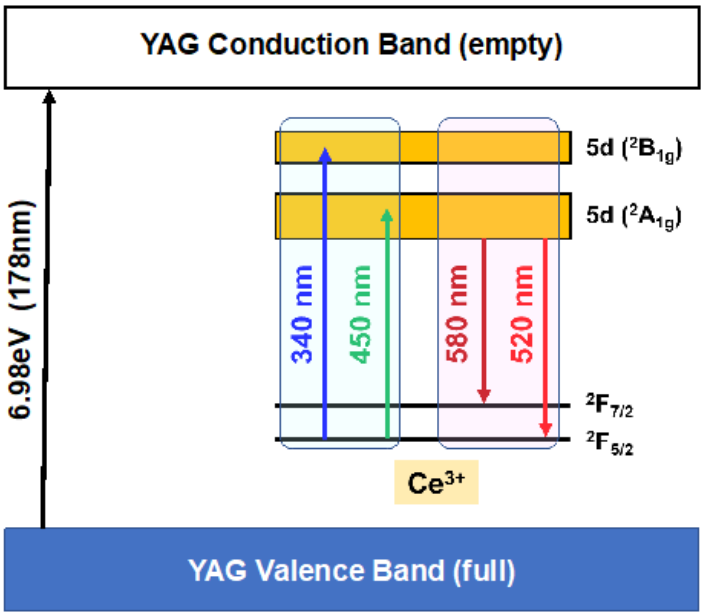

Figure 3.10: Ce3+ has 4f1 configuration (Ibrahim *et al.*, 2015). The ground state electron configuration which can also be referred to as the lowest energy state (2F) (Allsman, 2021) splits into 2 sub-states or divisions of the original lowest energy state (the values being: "0.16eV apart; 2F7/2 and 2F5/2") due to "spin-orbit coupling" which occurs when there is an amalgamation of the moment of generated magnetisation with the naturally occurring properties incorporating the mass at its centre and how it has become charged electrically (Hosmane, 2007).The excited d states separated into 2A1g and 2B1g owing to crystal field splitting (this term is the process of the change of different d orbitals of ligands. This is also the explanation for the changes in colour which occur between two metal-ligand complexes (Flowers et al., 2020; Lancashire, 2020). The diagram is adopted from Fang *et al.*, (2014) and redrawn by Dr. Peter Holliman.

One challenge is that measurement of band gap in clay minerals is somewhat challenging, with techniques and simulations sometimes giving different answers (Horwath and Liang, 2011). Though it is surmised here that composition may be responsible for fluorescence, Howarth and Liang, (2011) observed, using transmission electron microscopy (TEM) with electron energy loss spectroscopy (EELS) that chemical composition information could not be directly correlated with band gap information and there was no clear relationship between degree of isomorphic substitution and band gap energies. Comparison of density functional theory (DFT) simulations and UV spectroscopy showed that the clay minerals hectorite and montmorillonite differed. In the simulations, hectorite had a band gap of approximately 4 eV (insulator) while montmorillonite gave 0 eV (suggesting a conductor) (Figure 3.11). The UV-Vis spectrum showed that hectorite had a range of band gaps from 1.5 eV to 6.5 eV compared to that of montmorillonite which started at 2 eV and extended to 6.5 eV (Figure 3.12)(Horwath and Liang, 2011). The main difference between the two minerals is the degree of isomorphic substitution. For fluorescence to be observed, the band gap would have to be within that of visible light (< 3.2 eV), so some of the clay mineral may fluoresce where the bandgap is below this.

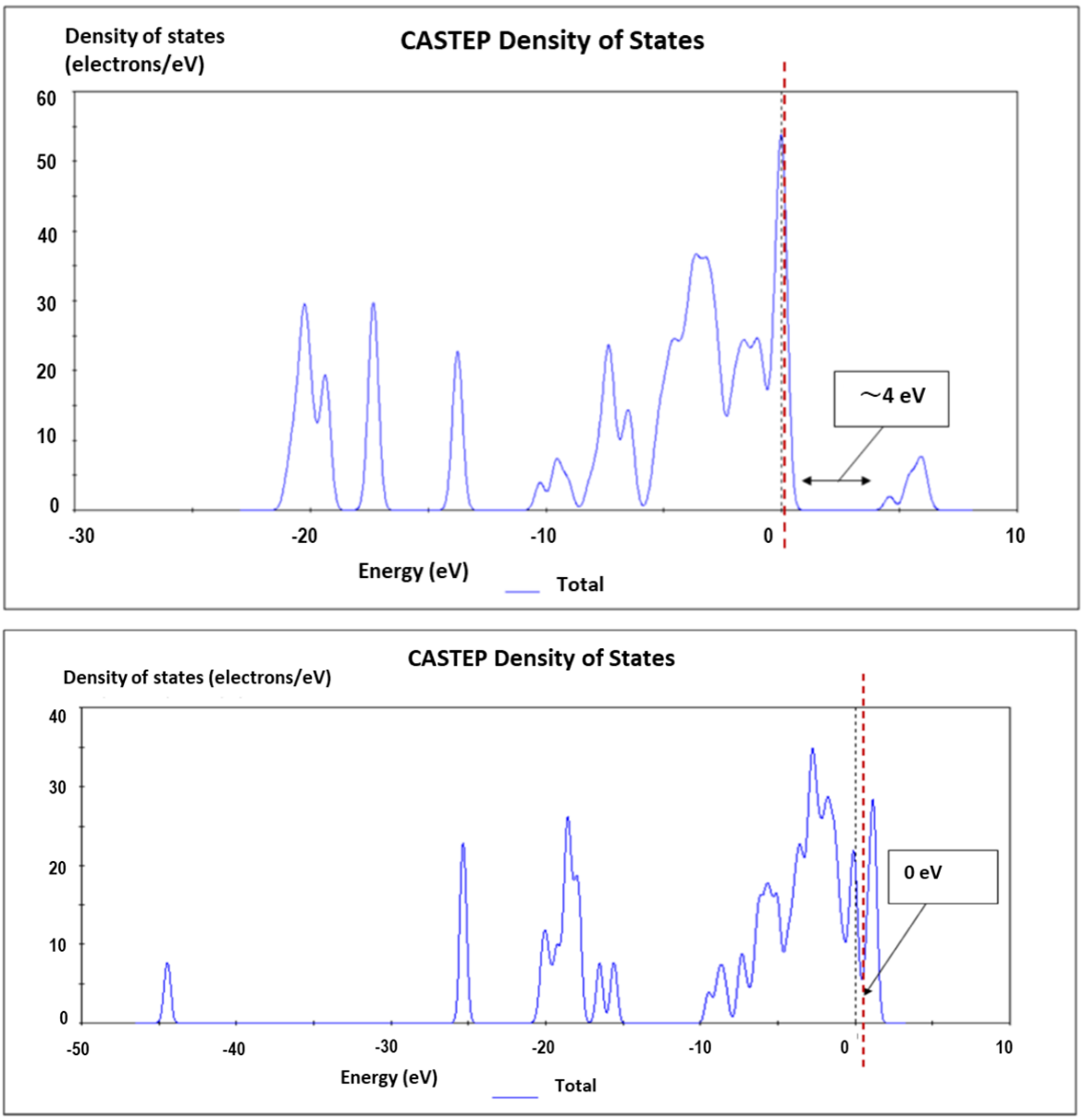

Figure 3.11: CASTEP theoretical modelling results for hectorite (top) and montmorillonite (bottom) clay minerals respectively. Adopted from Horwath and Liang, (2011).

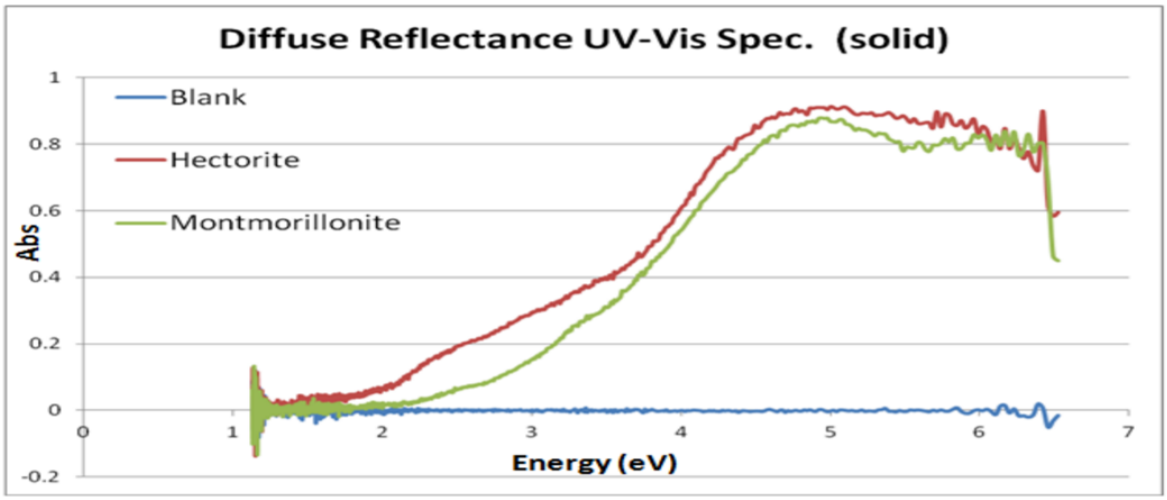

Figure 3.12: Diffuse reflectance UV-Vis spectra for hectorite and montmorillonite clay minerals. Adopted from Horwath and Liang, (2011).

We suggest the same is true of kaolinite and a recent study by Pietzsch et al., (2015) using DFT methods alongside X-ray absorption spectroscopy (XAS), showed that defect states in the band gap for kaolinite contained defects where oxygen replaced hydrogen in one of the Al (001)-hydroxyl groups of the kaolinite clay sheets< decreasing the band gap by about 3.2 eV, and thus fluorescence may be observed.

3.4.3 The Effect of Na^+/Ca^{2+} Exchange on Fluorescence

In LS-EOR mechanisms, Na^+/Ca^{2+} exchange is of considerable importance, especially for the multi-component ions exchange (MIE) mechanism discussed in Chapter 1. Comparison of fluorescence intensities of Na^+/Ca^{2+} exchanged samples of SWy-2 (Na-rich montmorillonite) were carried out to test whether they could be distinguished from one another under confocal microscopy upon ion exchange. Na^+/Ca^{2+} exchanged samples contain significantly higher amounts of Ca^{2+} compared to the original SWy-2. For these experiments, ion exchange of 1 g of SWy-2 and 1 M $CaCl_2$ brine were conducted in centrifuge tubes. The samples were well mixed by the stirrer for more than 3 hours at 480 rpm. The supernatant solution was discarded and then deionized water added to dissolve any sodium salts. This process was repeated another two times. Upon subsequent analysis in the fluorescence microscope, there was no significant intensity difference between Na^+/Ca^{2+} exchanged samples and SWy-2, however a larger area fluoresced from the samples of Na^+/Ca^{2+}exchange, illustrating that it may be possible to differentiate pre-ion exchanged images and post-ion exchanged images from one another by the brightness of the images, but not with relative fluorescence intensity (Figure 3.13).

The result is consistent with the results obtained after testing fluorescence of brines; there are no significant differences in fluorescence intensities between Ca-rich bentonite clay and Na-rich bentonite clay. However, the relatively Ca-rich exchanged bentonite clay showed a wider fluorescence area.

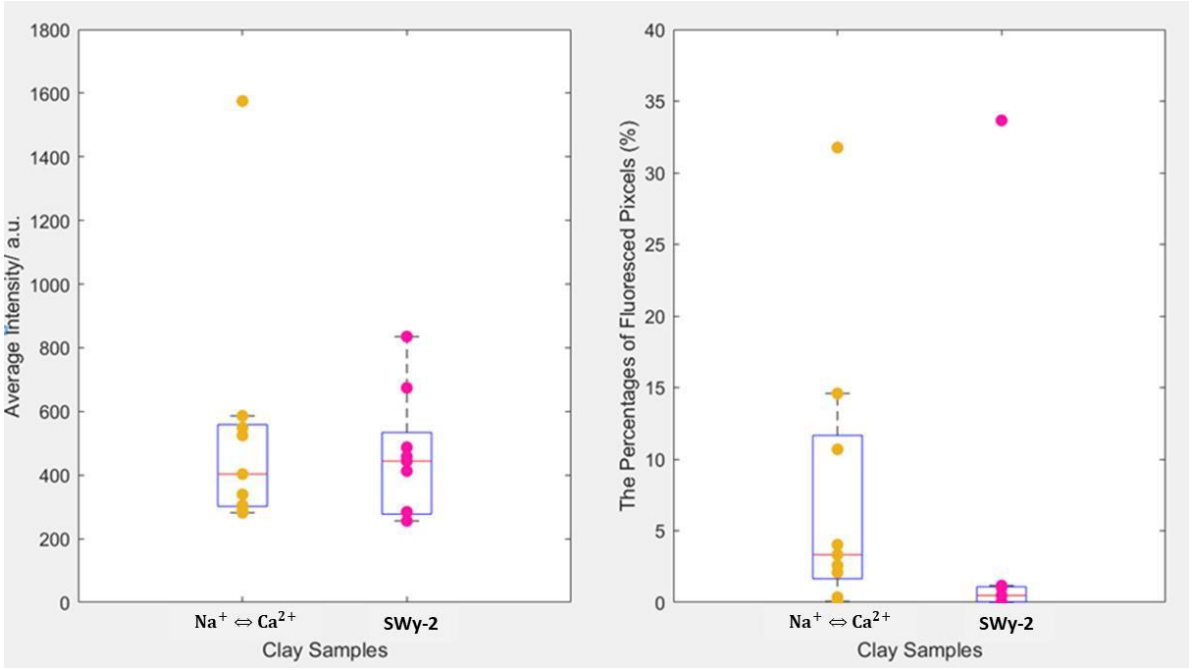

Graph 3.13: (Left) Average-fluorescent intensity of images of pre-ion exchanged and post-ion exchanged. (Right) The average-percentages of fluoresced scope per image. The brightness of the images can identify the fluorescence images of pre and post ion exchange but not with relative fluorescence intensities.

3.4.4 Fluorescent Properties of Mg/Al Layered Double Hydroxide Minerals

To ascertain whether presence of certain elements impacted the fluorescent properties of layered minerals, and whether these were due to inclusion of fluorescent elements such as Fe in the natural clay minerals, a set of synthetic minerals from the layered double hydroxide (LDH) group were tested. These were prepared in previous work by the Greenwell group and had known composition, being prepared from high purity reagents and under controlled conditions.

The first set of samples, with varying Mg/Al ratio (the higher the Mg/Al, the more Mg) looked the effect of these two elements in natural clay mineral clay samples. This is clearly demonstrated by the fact that KGa-1b and IMt-1, which are the second and third most extensively fluorescing samples, respectively, contain relatively higher aluminium content according to a comparison of the chemical data provided from the website of the Clay Minerals Society [see Apendix 5]. The results for the different Mg/Al LDH are shown in Figure 3.14. No correlation was found between the aluminium (Al) and magnesium (Mg) content with either strength of fluorescence intensity or in respect of the fluoresced scope. Moses (1963) and Rost (1995) suggested that the presence of aluminium might enhances the fluorescence and categorised Mg as one of the elements that quenches fluorescence, while the data in Figure 3.14 shows an opposite effect to this, suggesting the particular local environment of the Al and Mg must also play a part.

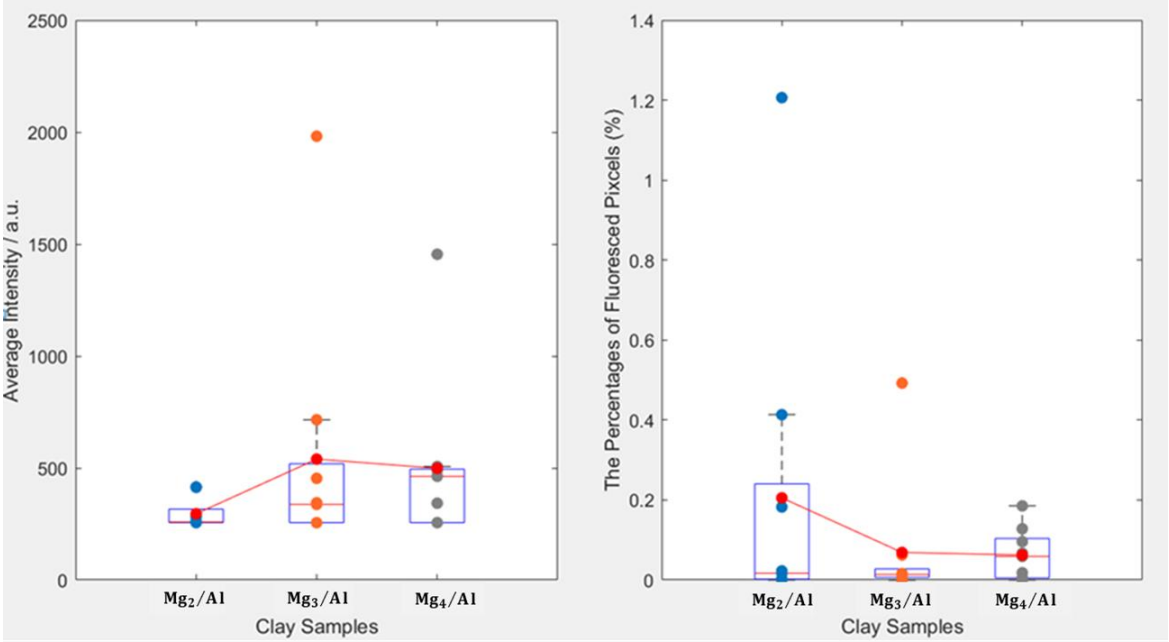

Figure 3.14: Sample Mg4/Al LDH as compared to sample MG2/Al contain a higher percentage of magnesium and a lower percentage of aluminium, and it has been ascertained that considering the volume of the magnesium and aluminium in both samples, this bears no effect upon the fluorescence intensity and the extent of the pixels in the fluoresced images if any other external factors were not involved in the results. Each red dot shows the average values acquired from nine data samples.

3.4.5 Fluorescence of Mg/Fe Layered Double Hydroxides

To investigate the relationship between fluorescence and the types of elements, another group of LDHs containing Mg/Fe were analysed. As with the Mg/Al LDH, the higher the Mg/Fe designates higher Mg content and less Fe content. The results showed that both fluorescent intensity and percentages of fluoresced pixels rapidly increased as the Mg/Fe increase (Figure 3.15). As noted already from the previous test with LDH Mg/Al, the amount of magnesium within the samples does not influence its fluorescence intensity and scope, however the higher amount of Fe would have curbed fluorescence intensities and scope. As increasing Mg means a diminishing Fe content this may have amplified the fluorescence intensities and scope as Fe in minerals is widely acknowledged as a potential inhibitor of fluorescence, which may modify or quench fluorescence (Moses, 1963; Rost, 1995; Hui, 2020; King, 2020).

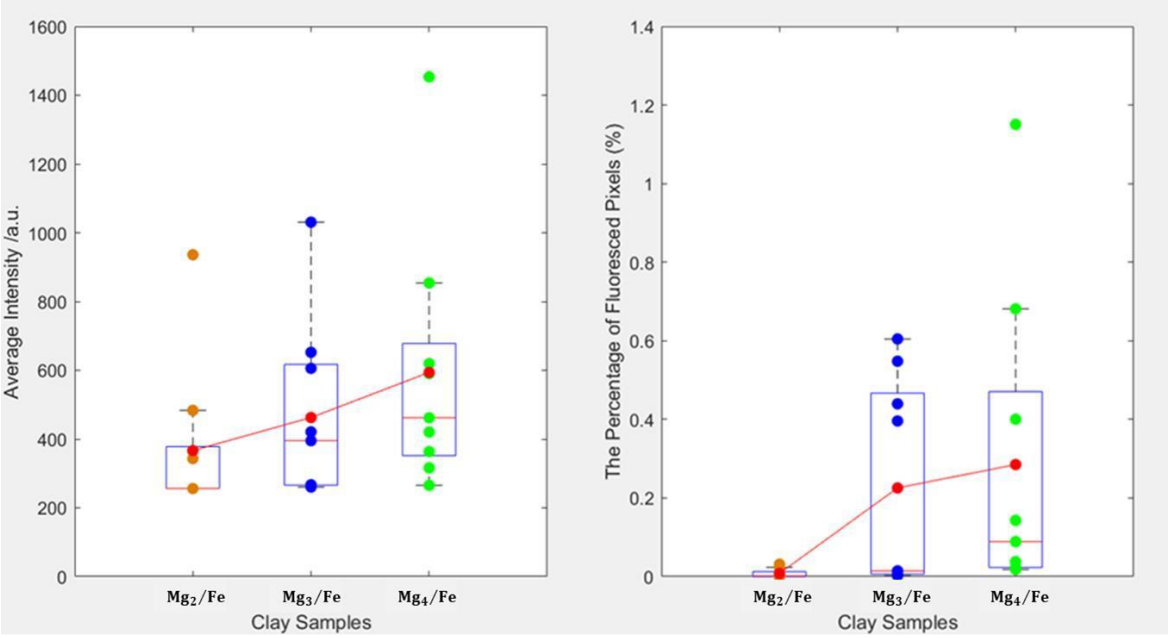

Figure 3.15: Mg_4Fe LDH as compared to sample Mg_2Fe contain a higher percentage of magnesium and a lower percentage of iron thus higher magnesium and lower iron contents were present, which increased the average fluorescence intensity and also the extent of the pixels in the fluoresced images. After comparing Figure 3.7 and Figure 3.8, it has been ascertained that there was no correlation between magnesium content and the fluorescence of the clay samples; a higher amount of iron might have suppressed the fluoresce of the clay samples.

3.5 Scanning Electron Microscopy Analysis

The samples of KGa-1b recorded the lowest fluorescent intensity and exhibited the second widest fluoresced scope, and SCa-3(Montmorillonite), which recorded a higher average intensity than KGa-1b, and fluoresced with less scope were both examined by scanning electron microscopy (SEM). The photomicrograph of KGa-1b is relatively uniform (Figure 3.16 a), whereas the photomicrograph of SCa-3 displays the presence of many different kinds of mineral grain (Figure 3.16 a). With the intention of detecting the location and presence of mineral grains more precisely, the SEM images were processed with Image - J Fiji, shown in Figure 3.16 b and Figure 3.17 b. As compared to the scale of the image, the area redacted in red must not contain only single clay particles, due to the size of the clay particles which are typically less than 2 µm (Brindley, 1981; Ito and Wagai, 2017; Huggett, 2019), and, thus, the red colour might be representative of mineral grains, which may also contain impurities. Some of the red areas may possibly constitute aggregation of clay particles, such as inside of the yellow lines, especially the clay particles which are often found to be larger than 2 µm (Huggett, 2019). Some mineral grains are exceptionally large, due to higher relief and exhibited distinct boundaries; an example is shown within the dashed blue line in Figure 16. The other clay samples which were tested, such as SWy-2, SCa-3, and Na-Bentonite also presented a similar variety of mineral grains as observed in the SCa-3 photomicrograph [see Appendix 4]. Therefore, it is possible that the difference in fluorescence intensity and its

scope might be contingent upon variation within the mineral composition of the samples. In order to ascertain whether other mineral phases were present, X-ray diffraction (XRD) analysis was used to find the mineral composition of each of the clay mineral samples, so that any relationship between the mineral compositions could be established.

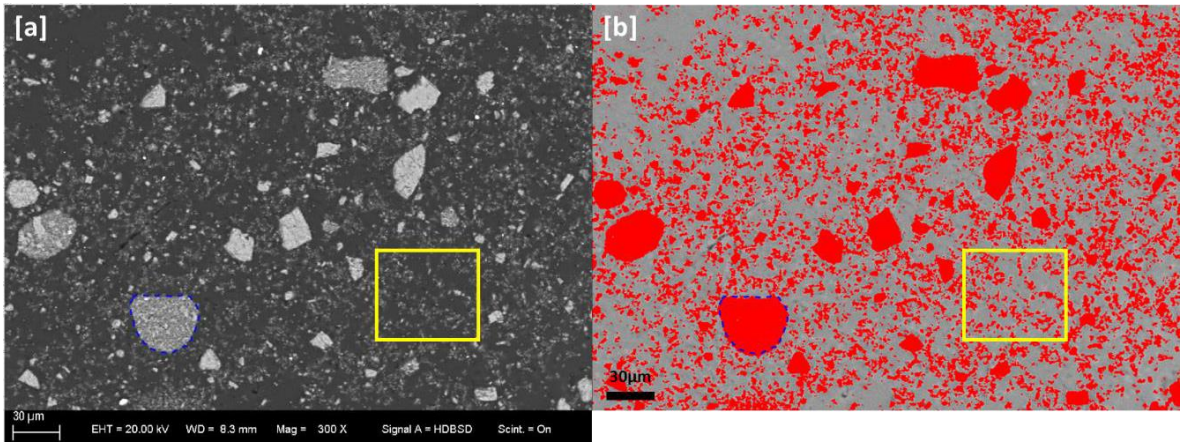

Figure 3.16: (a) Original SEM image of KGa-1b; which clearly shows that KGa-1b is relatively uniform in grain variations (b) SEM images which processed with Fiji ImageJ; the red area accounts for approximately 32% of the total area. Blue dashed line is showing a significantly large mineral grain that would have possibly blended from a different source. Inside of the Yellow lines which could be an aggregation of clay particles.

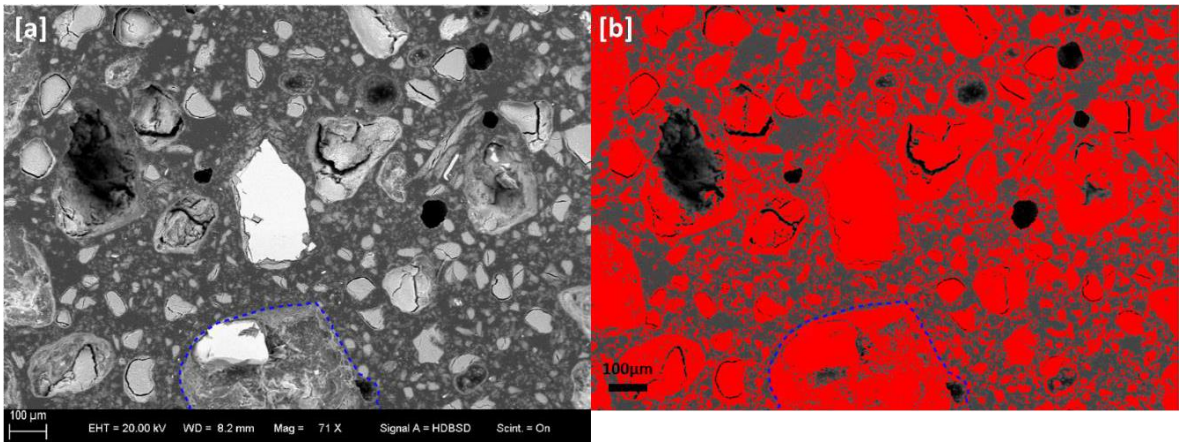

Figure 3.17: (a) Original SEM image of SCa-3; it is clearly showing that SCa-3 is made up of many types of mineral grains. (b) SEM images which were processed with the Fiji ImageJ; the red area accounts for approximately 57% of the total area. Blue dashed line is showing a significantly large mineral grain that would have possibly blended from a different source.

3.6 X-Ray Diffraction Analysis of Clay Mineral Samples

Quantitative X-ray diffraction (XRD) analysis was undertaken by X-ray Mineral Services Ltd, North Wales, in the interest of further understanding the composition and cause of fluorescence of the clay mineral samples.

3.6.1 Impurity Analysis of Clay Mineral Samples

The SEM analysis suggested a quantity of non-clay mineral grains were present in the samples. Comparisons of the data provided by X-ray Mineral Services Ltd allowed the mineral composition of the samples to be established and the presence of other phases confirmed by the bulk of the XRD data provided for KGa-1b, KGa-2 and SCa-3 (Table 3.2), also for the separated clay fraction data for KGa-1b, KGa-2, SCa-3, and Na-bentonite (Table 3.3).

Since the percentage of an average fluorescent scope for KGa-1b and the proportion of total non-clay minerals for KGa-1b are consistent, it is considered that the anatase, which is known to be a photocatalytic polytype of titanium dioxide, is likely to have contributed to the wider fluorescent scope of the KGa-1b sample. However, as shown in Figure 3.18, titanium dioxide exhibits considerable fluorescent intensity at emission wavelengths between 350 nm and 400 nm, whereas the fluorescent images of KGa-1b were acquired at the emission wavelength of 517 nm, which is longer than the 400 nm wavelength in the emission spectra, also the intensity exhibited was less than 100 a.u., which is low enough to be dismissed. At this point, even if quartz grains exhibited strong fluorescence emission, it would be improbable to show such a wider fluorescence area, with only 1.2% of quartz impurity (see Table 3.2), especially if the fluorescent scope reached to only 4.5% of the image. Hence according to a comparison of fluorescence data, SEM images, and bulk XRD analysis data, as well as separated clay fraction XRD data, the authenticity of the observed KGa-1b autofluorescence can be confirmed, especially the fluorescence of < 2 μm mineral fraction within the KGa-1b sample, which firmly infers autofluorescence of KGa-1b itself. In addition, large mineral grains, between 15 μm and > 30 μm which were observed in KGa-1b SEM images, are likely to be comprised of mainly quartz grains and only the small fraction of quartz within the XRD analysis would be unlikely to be detected in the confocal fluorescence microscope. The following Table 3.2 and Table 3.3 also show the mineral phase composition for high defect kaolinite and low defect kaolinite to be analogous, and thus their difference in fluorescence intensity and scope is not synonymous with their chemical composition, but probably due to their physical and structural characteristics.

Table 3.2: The quantification for the bulk sample of the CMS standards KGa-1b and SCa-3; provided from the X-ray Mineral Services Ltd. The non-clay minerals for the KGa-1b is only 2.3% in total. The mineral phases and its quantity for KGa-2 are much the same as is compared to KGa-1b. SCa-3 contains a more considerable amount of non-clay minerals which makes it more challenging to identify the cause of fluorescence.

Sample	Anatase	Quartz	Plagioclase	K-feldspar	Kaolinite	Illite	Montmorillonite	Total non-clay minerals
KGa-1b	1.10%	1.20%	—	—	97.70%	—	—	**2.30%**
KGa-2	1.80%	0.4%	—	—	97.80%	—	—	**2.20%**
SCa-3	—	6.40%	4.50%	4.30%	—	5.40%	79.50%	**15.20%**

Table 3.3: <2 micron separation of the 4 types of clay samples; the samples were run as random powders. In the Na-bentonite sample, a small amount of Opal-C was detected; the exact quantity for the Opal-C is unknown, yet is considered to be less than 2-3%.

Sample	Lab n.	Wt. % <2um	Smectite	Illite/Smectite	Illite+Mica	Kaolinite	Chlorite	Quartz	K Feldspar	Plagioclase	Calcite	Dolomite	Anatase	Pyrite	*Total*
Kaolinite (KGa-1b)	199	50.5	0.0	0.0	0.0	**98.5**	0.0	0.0	0.0	0.0	0.0	0.0	**1.5**	0.0	***100***
Kaolinite (KGa-2)	200	84.4	0.0	0.0	0.0	**98.3**	0.0	0.0	0.0	0.0	0.0	0.0	**1.7**	0.0	***100***
Montmorillonite (SCa-3)	201	31.9	**100.0**	0.0	0.0	0.0	0.0	TR	0.0	0.0	0.0	0.0	0.0	0.0	***100***
Na-Bentonite (Steetley Na-Bentonite)	202	73.7	**91.3**	0.0	0.0	0.0	0.0	**8.7**	0.0	0.0	0.0	0.0	0.0	0.0	***100***

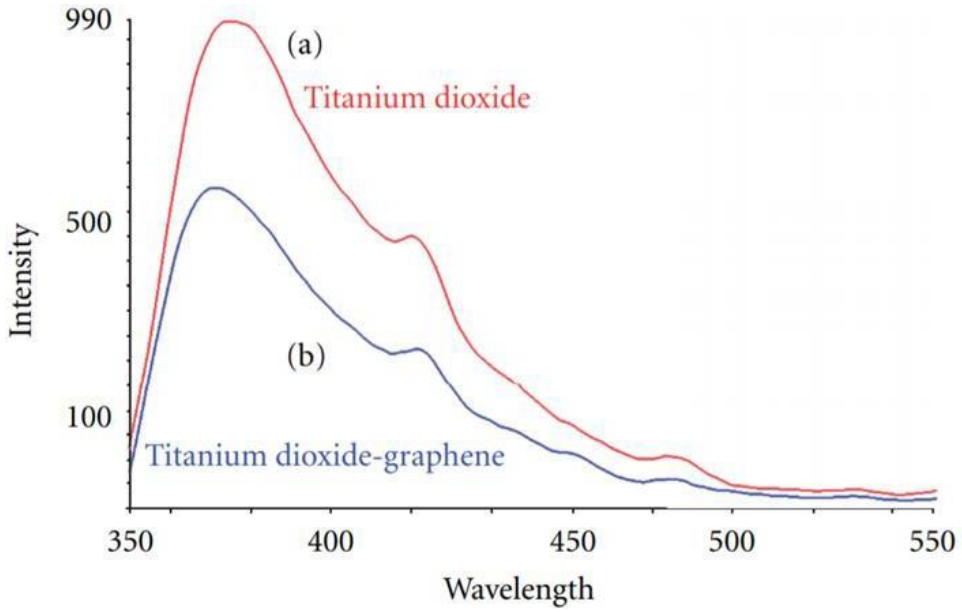

Figure 3.18: Fluorescence emission spectra of titanium dioxide (anatase) (Basheer, 2013). The graph implies that the applied emission wavelength does not show higher than 100 intensity.

Conversely, the SCa-3 sample contained a wider variety of non-clay minerals, as was expected from the SEM analysis, thus making the task of attributing the origin of fluorescence in the sample more complex. Due to the provided data for Na-bentonite being limited, in comparison with other clay samples, preferentially oriented XRD analysis (filtered) was run on Na-bentonite, and the results are shown in Figure 3.19 and Figure 3.20. As bentonite is often made up of an aggregation of multiple minerals (Ito *et al*., 1994), it is perhaps not surprising that Figure 3.19 and Figure 3.20 also present a few types of clay minerals, and some additional non-clay mineral impurity reflections. At first glance, Table 3.3, which contains mineral fraction data, suggested that Na-bentonite was a relatively pure sample as over 70% of the sample was found to be comprised of the < 2 μm fraction and, furthermore, over 90% of this < 2 μm powder was determined to be in the smectite group. However, it was also clear that the samples were not pure, as Table 3.3 presents, and based

upon SEM data and Figure 3.19 and Figure 3.20. This was probably because most of the impurity grains in Na-Bentonite were much larger than 2 μm. The Na-bentonite sample contained more than enough impurity to detect fluorescence from other phases than SWy-2 itself and, especially, according to the bulk XRD analysis, as Na-bentonite contains 2-3% of Opal-C which is also known to be a strongly fluorescing mineral (Schneider, 2010), which might have a considerable fluorescence effect on the micron-scale studied in the confocal microscope.

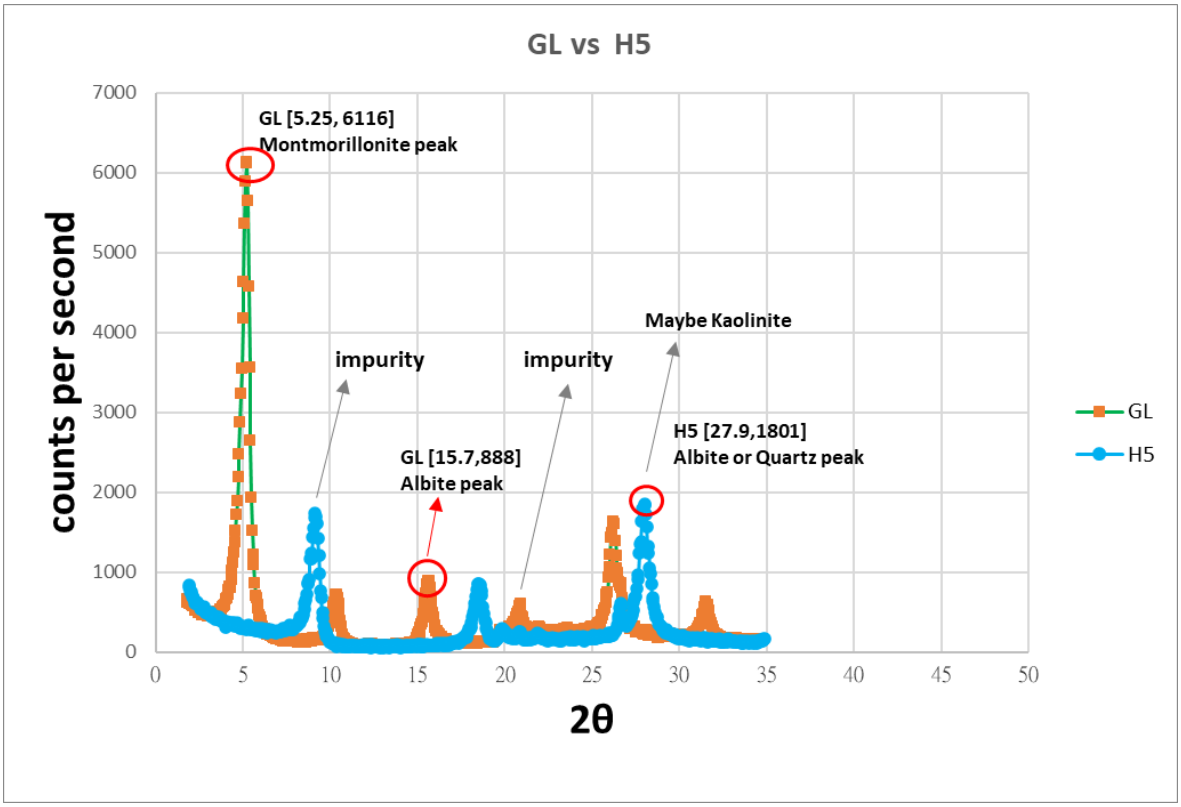

Figure 3.19: XRD oriented filter data shows multiple types of clay minerals within the SCa3 sample, as well as non-clay mineral impurities. (GL) Glycolated sample (H5) heated at 550°C.

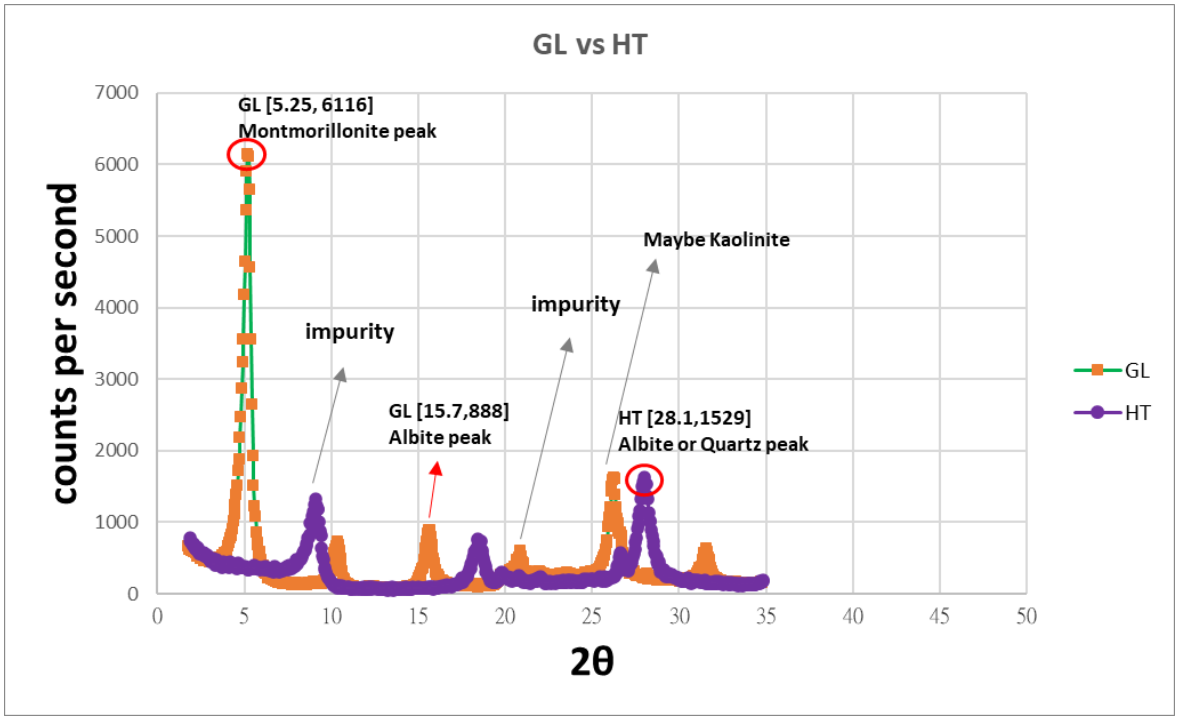

Figure 3.20: XRD oriented filter data shows multiple types of clay minerals and impurities. (GL) Glycolated sample (HT) heated at 380 °C.

3.7 Conclusions

In order to study LS-EOR *in situ* using non-destructive/invasive methods, confocal fluorescence microscopy may present an opportunity. However, before undertaking *in situ* experiments, the fluorescent properties of the various components of the experiment need to be established. Here it has been shown that crude oil is too highly fluorescing to be used, while the brine phases and glassware are all suitable. As such a model crude oil with low fluorescence has been found to be suitable. Furthermore, a range of layered minerals has been examined for fluorescent properties, with the effect of defects, composition and impurity phases explored.

Since fluorescence of clay minerals have not been investigated previously, to the best of the authors' knowledge, clay samples containing impurities, such as the SCa-3 and Na-bentonite are challenging to establish the origin of fluorescence within. For this reason, for further work, the most appropriate clay sample is KGa-1b, which is pure enough to determine and confirm that the fluorescent component is the kaolinite itself.

Chapter 4 Imaging of Swelling and Mobilisation Using Fluorescence Methods

4.1 Total Internal Reflection Fluorescence Microscope Analysis

TIRF was employed to assess whether the fluorescence of clay minerals confirmed in Chapter 3 could be utilised for the study of LS-EOR effect. In contrast to confocal microscopy, TIRF emits light from below the sample, thus the sample is not required to be sandwiched between a microscopic glass slide and a cover glass. This allows imaging of dynamic processed through the base of a sample cell, which allow the instrument to observe clay swelling or movement more naturally and *in situ* variation of solution composition.

Figure 4.1 shows xy dimensional images which were captured using the TIRF, and the labels provided on the top-right match the following graph in Figure 4.2. In this experiment 200 µl of high salinity water was initially added to the TIRF cell, followed by 200 µl of low salinity water added 300 seconds after the monitoring commenced. Another 200 µl of low salinity water was then added at 600 seconds. Finally, 300 µl of the solution was removed from the sample then 300 µl of low salinity water was added before the time reached 950 s. The duration of the monitoring continued for 1200 seconds in total. The experiment is shown in snapshots extracted from the digital recording in Figure 4.1.

Figure 4.1 (a) shows the initial state of clay minerals, before the inclusion of high salinity brine; hence, the image is only showing some clusters of Na-Bentonite which were aged with formation brine and non-polar crude oil within the TIRF cell. Some particles that fluoresce with significantly high intensity compared to the surrounding area are assumed to be impurities within the Na-Bentonite, and are shown with green circles (see Chapter 3, '3.6.1 Impurity Analysis of Clay Mineral Samples'). Figure 4.1 (b) shows the sample 15 seconds after adding 200 µl of high salinity water. The cluster of clay mineral crystals has become blurred, and the image overall changed and became whiter when compared to Figure 4.1(a), which suggested that the clay minerals were swelling. Figure 4.1(c) shows 70 seconds after the high salinity water was added, and the cluster of clay minerals on the top-left started moving towards the left. After 135 seconds post addition of the high salinity water (Figure 4.1(d)), the cluster of clay minerals on the top-left completely disappeared from the area of imaging. Figure 4.1(e) shows 310 seconds into the study, during which 200 µl of deionised water was added; the image is dark because no image would be acquired while adding extra solution due to a safety interlock to cut off the laser light. Figure 4.1(f) is a snapshop taken 350 seconds after commencing monitoring the image, immediately after adding deionised water; the inside of the red-square identified a marked difference between (d) and

(f). The remaining clay particles were dispersed upon lowering the salinity in the system; however, no other significant changes were observed between 300 seconds and 600 seconds into the study. Figure 4.1(g), shows that after 615 seconds and while adding another 200 µl of deionised water, when compared to the images in Figure 4.1(f), it can be perceived that the clay mineral cluster has undergone further swelling and the gaps between clay minerals became closer by approximately 1.3 and 1.7 times as is shown with the green and yellow arrows respectively. After 850 seconds elapsed after starting monitoring the image (Figure 4.1(h)), the clay particle on the top-left, inside the red-square, was moved from outside of the studied area. At 910 seconds after monitoring the image started, shown in Figure 4.1(i), clay particles inside of the red-square started oscillating and moving towards the lower right. The oscillation of the clay minerals occurred some 300 seconds after adding the deionised water and, hence, it is considered that the motion caused was due to the reduction of the salinity in the system, not the physical force from the water flow. Figure 4.1(j) shows 950 seconds after monitoring the image commenced, 300ml of the solution in the system was removed then another 300ml of deionised water was added; the image became dark due to the aforementioned reasons in Figure 4.1(e). Figure 4.1(k) and Figure 4.1(l) depict images at 980 seconds and 1095 seconds into the monitoring of the images respectively, with no further significant changes observed through to the experiment end.

TIRF establishes that swelling of clay minerals and higher sensitivity of fines movement occurs after altering the salinity of the system. Figure 4.1 was an optical image, whereas Figure 4.2 is numerical, showing swelling and migration of clay minerals. Figure 4.2 clearly shows that the mean fluorescence intensity has decreased by adding more deionised water to reduce the salinity in the system; this reaction is attributed to the swelling of clay minerals as observed in Figure 4.1, due to the dispersion of the fluorescence of the clay. At 600 seconds after monitoring the image, when the brine in the system was diluted by deionised water for the second time, it became clear that the changes in amplitude had increased in intensity which indicates that the movement of the clay minerals became significantly intense after a fourfold dilution. More intense movement of clay minerals was also observed in Figure 4.1(h) and Figure 4.1(i). After 900 seconds, although the solution in the sample was even more diluted, no significant changes were observed hence, it can be determined that fourfold salinity dilution initiated low salinity effects in this study. Referring to Table 4.1, which provides a four-fold dilution of high salinity brine, if the ionic concentration of high salinity water is considered at 10, 000 mg/L, then 2, 500 mg/L fits within the range of slightly saline water. The results also signify that clay swelling and fines migration may occur by adding low salinity brine to samples initially aged with non-polar crude oil - these findings are supported by AFM (Chapter 5) as well as Al-Sarihi *et al*., (2018) and Maskari *et al*., (2019).

4.2 Conclusions

Having established the fluorescent properties of clay minerals in the presence of a model oil and brines in Chapter 3, in this chapter the use of TIRF is explored to understand the dynamic processes occurring when a clay mineral is exposed to salinity changes. This is potentially the first time that TIRF has been used to study clay mineral swelling dynamics and structures and this preliminary study has shown TIRF to have good resolution for studying the processes at work using a non-invasive method.

Here, a Na-bentonite sample was studied, with good fluorescence properties as identified in Chapter 3. Under changing from high concentration brine (total ionic strength of 0.69 M) to a low concentration brine, swelling and dispersion was observed in real time, confirming the role of swelling clay minerals and fines migration in low salinity enhanced oil recovery and that TIRF may present an ideal method for studying such processes

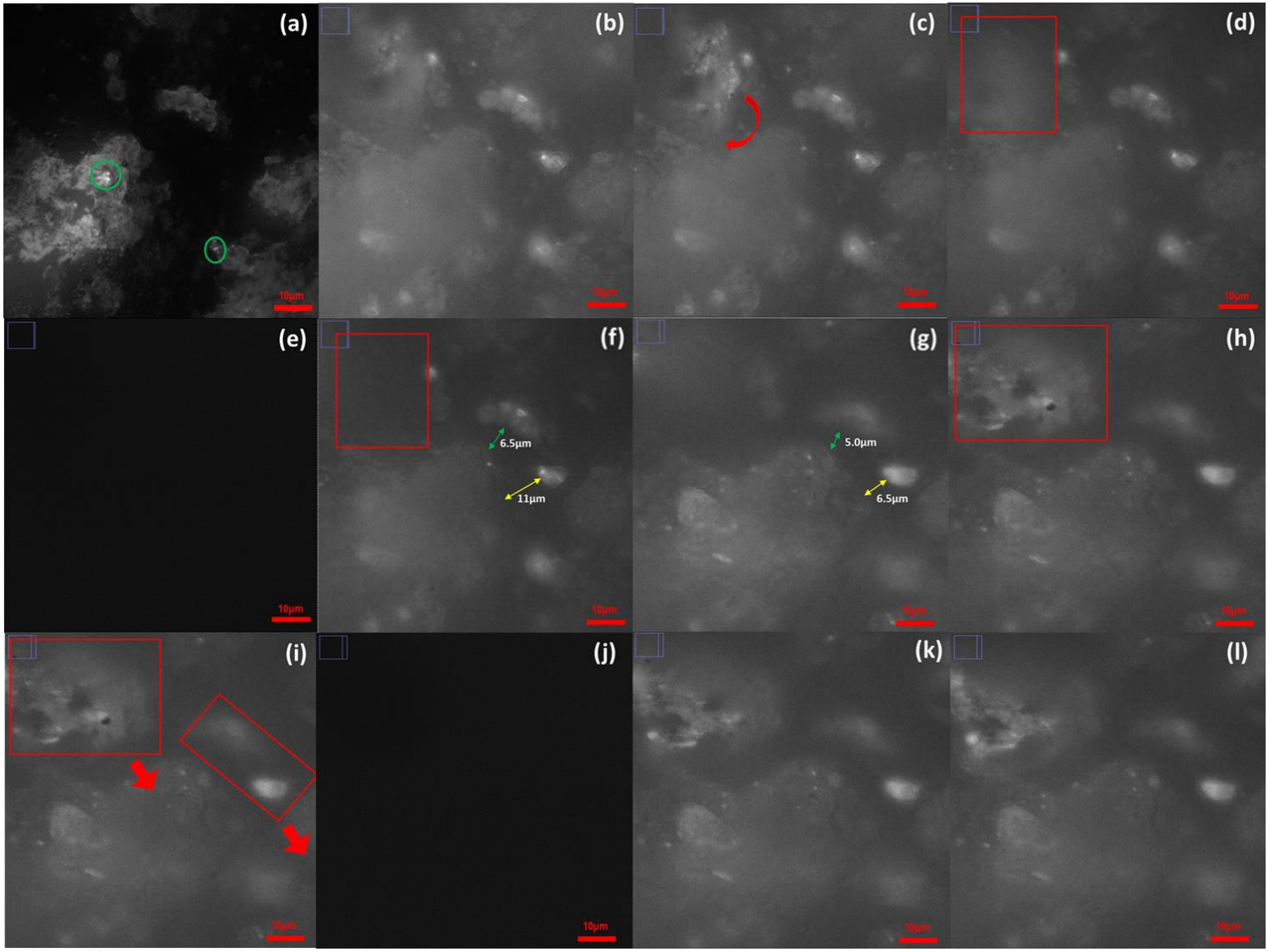

Figure 4.1: TIRF images of Na-Bentonite which was initially aged with formation brine and non-polar crude oil at 70 ℃. (a); the initial state before adding any solution to the sample. (b)～(d); after adding 200 µl of high salinity water. (e); The duration of adding the 200 ml of deionised water. (f); after adding 200 ml of deionised water. (g)～(i); after adding another 200 ml of deionised water. (j); the period having removed 300 ml of solution from the sample, then adding another 300 ml of deionised water. (k) and (l); after removing 300ml of the solution from the sample and then adding another 300ml of deionised water.

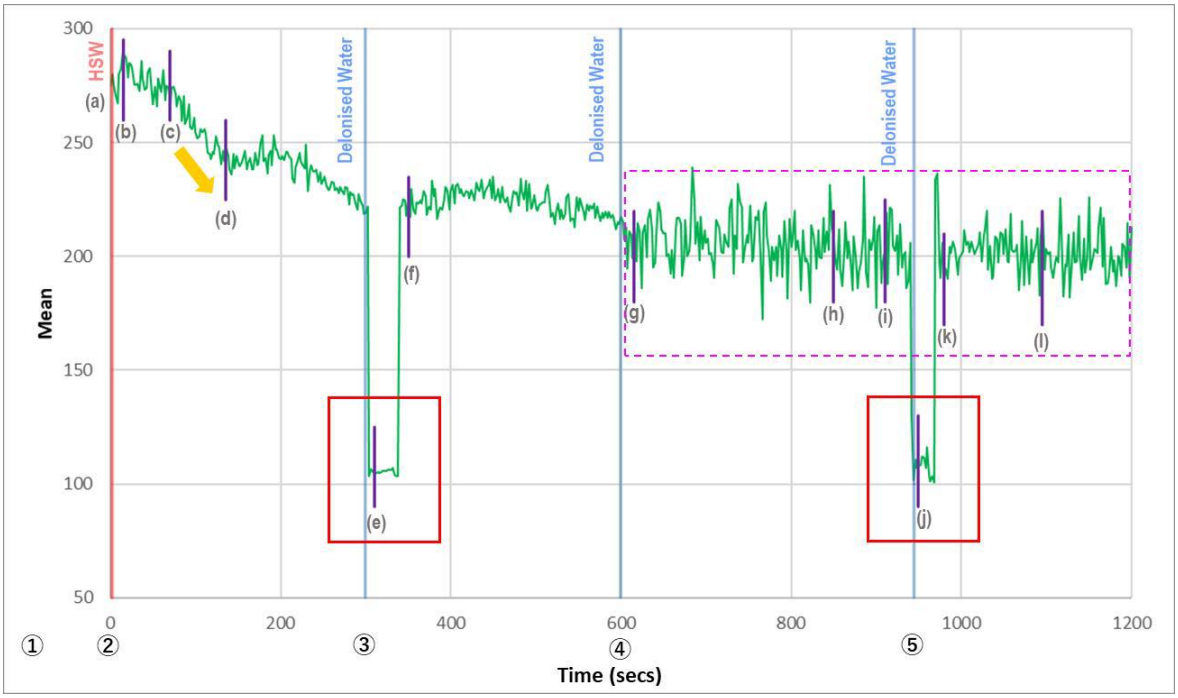

Figure 4.2: The graph is showing mean fluorescent intensity on the y-axis versus time on the x-axis; there is a slightly sharp decrease in the mean fluorescent intensity between (c) and (d) which is also shown with a yellow arrow corresponding to the disappearance of clay minerals. The red-squares highlight the dramatic drop in mean fluorescent intensity which are caused due to adding solution to the sample; At 600 seconds, the graph does not show a dramatic drop of mean fluorescent intensity as shown for the first time and third time in the added deionised water, (e) and (j) respectively. The absence of the dramatic drop of mean fluorescent intensity for the second time in the added deionised water is because the sample was once removed from TIRF, as well as paused monitoring, thus the trend was not recorded. The pink dashed- square emphasises that alteration of the mean fluorescent images were more intense as compared to the beginning of the monitoring when the system was still under the high salinity condition.

Table 4.1: The table shows the ionic concentration (mg/L) in the sample at each stage; it is assumed that the sample was initially aged with 0.5 ml of formation brine.

	①	②	③	④	⑤
Na^+	8108	11336.93	5675.54	3785.27	1894.21
Ca^{2+}	348	440.77	220.66	147.17	73.64
Mg^{2+}	147	1072.69	537.01	358.16	179.23
K^+	2383	443.85	222.20	148.20	74.16
Cl^-	15703	20361.35	10193.39	6798.42	3402.04
$SO4^{2-}$	—	1985.04	993.76	662.78	331.67

Chapter 5 Measuring Cohesion of Clay Minerals Using Atomic Force Microscopy

5.1 Introduction and Context

Owing to the limited availability of the fluorescence microscopy laboratory during the Covid-19 pandemic, and the slow re-opening owing to the laboratory being fully air conditioned and needing specialist legionella checks, it was decided to further probe the changes in the clay mineral samples with model oils with atomic force microscopy (AFM). The AFM is presently due to be upgraded to have coupled fluorescent microscopy, allowing the techniques to be combined. Thus, the initial AFM experiments undertaken here present initial data for comparison with the future upgraded instrument.

5.2 Methods

The methods are presented in Section 5.3.1. The samples used were prepared by the author, as described in Section 2.4.5, with clay minerals mounted on quartz slides. The AFM analysis was undertaken by Dr Miro Cafolla in the AFM laboratory of Prof. Kislon Voitchovsky in the Department of Physics, Durham University.

In order to test various types of clay mineral, KGa-1b (kaolinite), CCa-2 (chlorite), and IMt-1(illite) were purchased from the US Clay Minerals Society (Source Clay Repository). Any type of clay mineral can be applied to this stage of the experiment, regardless of the fluorescence intensity. Hence, it was possible to employ CCa-2, which was rejected for testing under the fluorescent microscopy due to its faint fluorescent intensity, however the sample proved valuable to test in this instance due to the fact that only one clay mineral in our sample had a positive surface charge (Meunier,2005; Kareem, 2016). Applying high salinity water and low salinity water in situ are possible in AFM experiments, and thus consistent with the TIRF analysis, further information of the ionic concentration of the brines are presented in Table 2.3.

5.3 Results and Discussion

5.3.1 Effect of Salinity Change on Kaolinite-Kaolinite and Kaolinite-Quartz Interactions

For the KGa-1b sample aged with non-polar model crude oil (dodecane), it was noted that as the condition shifted from high salinity to low salinity (see Figure 5.1), under high salinity (total ionic strength of 0.69 M), distinct KGa-1b clay crystals, with average thickness of ~20 nm, indicating multiple KGa-1b layers (ca 0.7 nm per layer) were observed. In contrast, at low salinity (total ionic strength of 0.02 M) distinct, individual crystals were no longer

visible and a uniform gel-like interface appeared. This suggests that swelling and dispersion of the adsorbed KGa-1b particles had occurred. Therefore, a strong layer cohesion seems to be prevented under the low salinity condition, though the clay sample was aged with non-polar oil (Figure 5.1). The ability of clay minerals to readily detach from a quartz surface at a low salinity condition was also confirmed through subsequent analysis of different types of clay minerals with the presence of polar crude oil. The observed decrease in structure on moving from high to low salinity, with dispersal of KGa-1b crystals to form a gel-like layer with no discernible topography is indicative of a low-salinity enhanced oil recovery effect, where migration of fine clay particles occurs and the attached oil is mobilised with the clay particle.

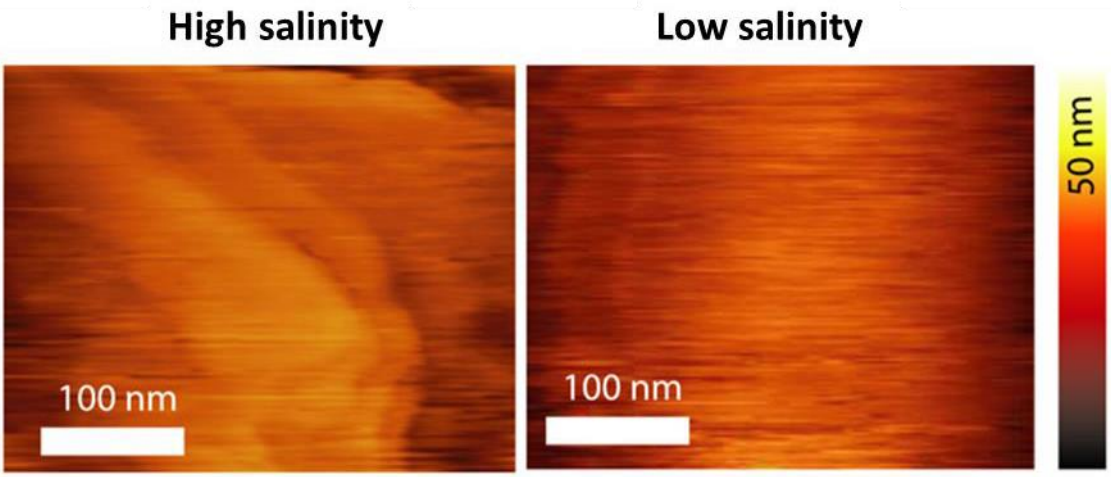

Figure 5.1: Amplitude modulation AFM imaging of the KGa-1b - brine interface. Changing from high salinity brine to low salinity brine results in a structural transition in the clay organisation with a local "melting" of layers. The sample was initially aged in the formation brine, then aged in presence of non-polar crude oil.

5.3.2 Comparison with Chlorite and Illite Reservoir Clay Minerals

Figure 5.2 illustrates the amplitude modulation AFM imaging of CCa-2. Again, under high salinity (total ionic strength of 0.69 M), individual CCa-2 particles can be observed on the substrate. As ionic concentration decreases, a more diffuse, gel like layer begins to form.

This trend is also repeated, and is perhaps more clear, in the IMt-2 clay mineral studied (Figure 5.3). Distinct individual crystals with a thickness corresponding to several layers are visible under the high salinity condition (total ionic strength of 0.69 M), though those layers disappeared and became more uniform as salinity decreased (approaching to the total ionic strength of 0.02 M). Under the low salinity regime, the IMt-2 gel structure was also easily displaced from the substrate by the scanning probe; the white line which is circled with a light-blue dashed line indicates a region where the clay minerals were dragged by the AFM tip.

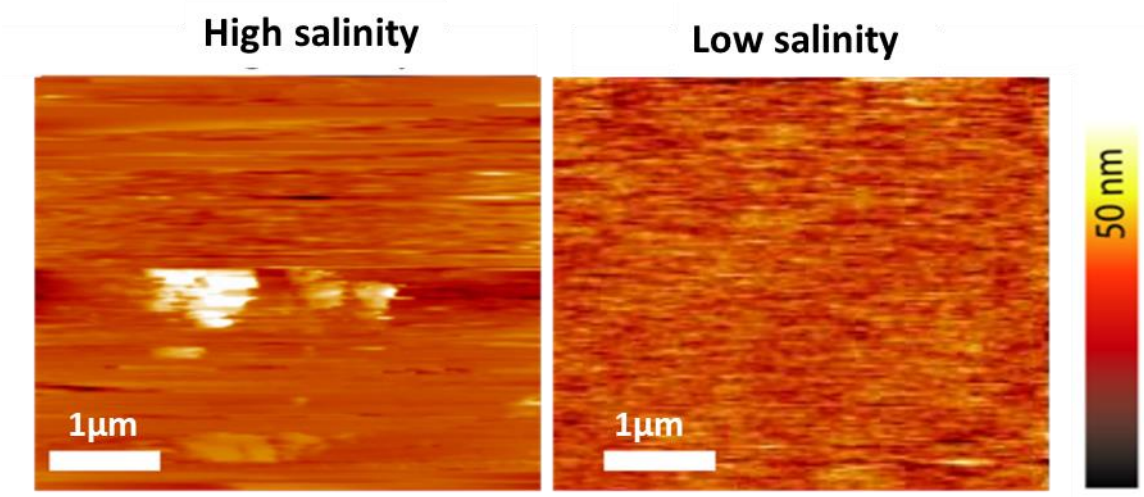

Figure 5.2: Amplitude modulation AFM imaging of the CCa-2 - brine interface. The change from high salinity brine to low salinity brine results in a structural transition, uneven interface to homogeneous interface. The sample was initially aged in the formation brine, then aged in amalgam with crude oil

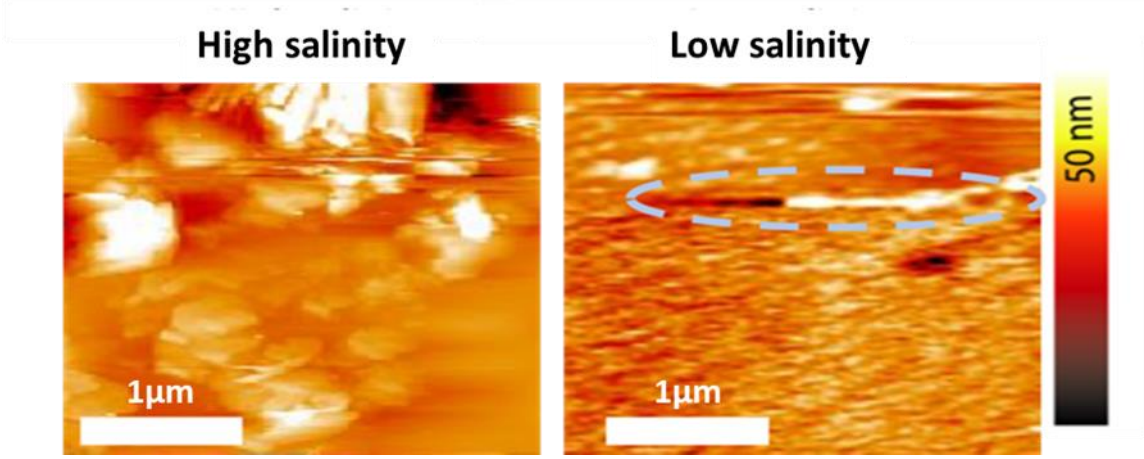

Figure 5.3: Amplitude modulation AFM imaging of the IMt-2- brine interface. Changing from high salinity brine to low salinity brine results in a structural transition, clay layers vanished resulting in the interface becoming more uniform and levelled. The sample was initially aged in the formation brine, then aged in amalgam with polar crude oil. The light blue dashed line highlights the clay dragged by the AFM tip.

5.3.3 Friction Force Microscopy Analysis of Clay Mineral Films Under Salinity Changes

Friction force microscopy (FFM) is where the sample is scanned with the AFM in the direction the cantilever undergoes a torsion movement. FFM was applied to 2 CCa-2 samples, which were aged in polar-model crude oil, to provide further insight into clay migration as a response to salinity alteration noted above in the amplitude modulation experiments.

For the first sample, as shown in Figure 5.4, the AFM tip was allowed to plough through the top layer of the CCa-2 film under high salinity condition, which resulted in the striated sample appearance. Lowering the salinity level weakened the ability of the adsorbed clay to effectively resist the applied force of the tip in the FFM experiment and, thus, the lateral torsion of the tip resulted in displacement of the top layers of the clay gel-like phase towards the edge of the scanned area.

For the second sample, shown in Figure 5.5, the result is similar to the findings from Figure 5.4. At high salinity, only a minor amount of clay particles are displaced by the laterally moving tip in the FFM experiment, and the yellow dashed line highlights the shifted clay particles. The bulk of the sample exhibits deep, slow to heal striations, indicating a well-structured and resilient sample with high viscosity. In contrast, at low salinity condition, the entire top layer was displaced by the scanning probe and stacked up at the edge of the scanned region.

Hence it can be concluded that lowering ionic concentration weakens the ability of clay minerals to resist the force from the AFM tip in FFM experiments, and therefore the top clay layers displaced towards the edge of the scanned area.

Furthermore, force spectroscopy analysis further confirmed that high ion concentrations present under high salinity conditions induce organisation of the clay into more resilient layers (Figure 5.6 and Figure 5.7).

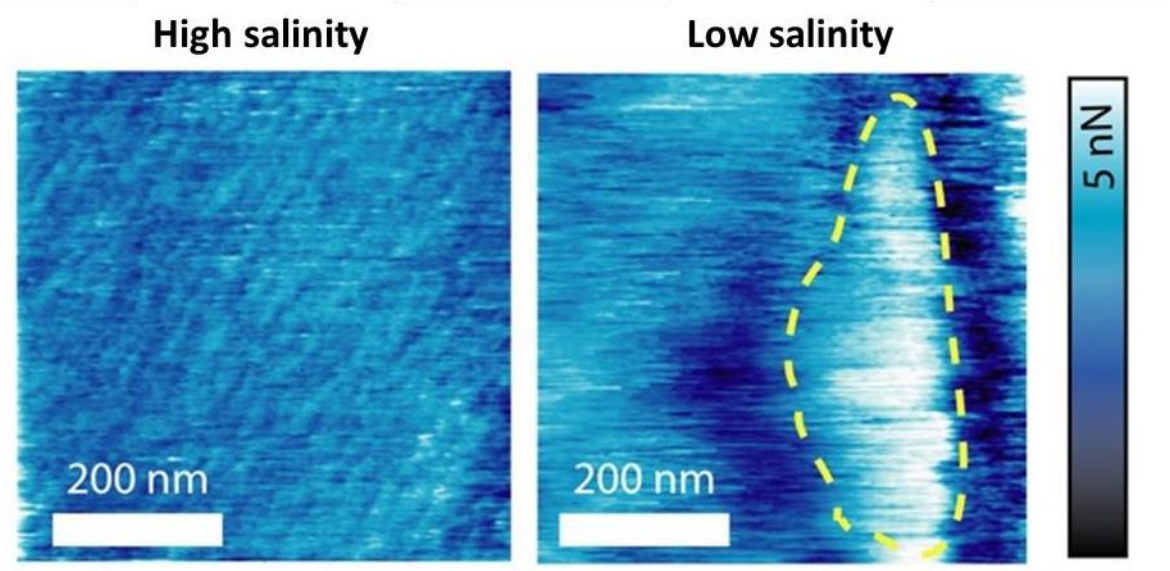

Figure 5.4: FFM imaging shows the interface of brine and CCa-2 (1), which was previously aged in polar model crude oil. For the high salinity condition, the tip can plough through the clay surface, which indicates some striated bands. Reducing the salinity level; thus, a sharp decrease in the ion concentration results in the lateral motion of the tip being able to replace the top layers of the clay sample as shown with the yellow dashed-curved line. The top layers of the clay are forcibly and quite quickly shifted towards the edge of the scanned area. Imaging was performed with application of force 5 nN .

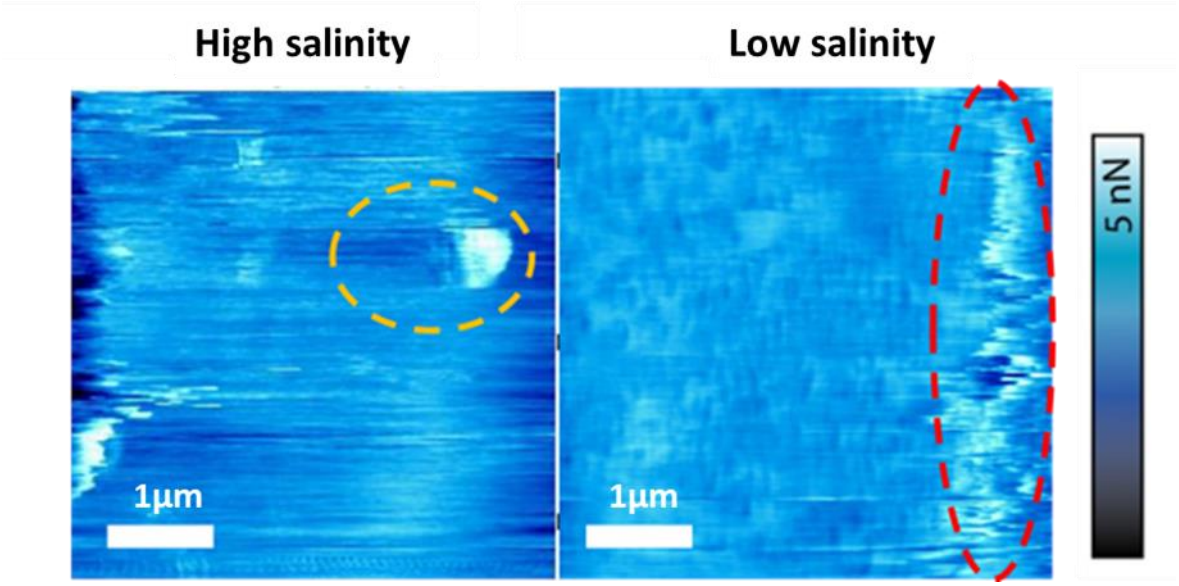

Figure 5.5: FFM imaging shows the interface of brine and CCa-2 (2), which was previously aged in polar model crude oil. For the high salinity condition, the tip could plough through only a limited area, which is highlighted by the yellow dashed-line. Reducing the salinity level therefore plunges the ion concentration results in the lateral motion of the tip, thus allowing for the replacement of the top layers of the clay sample- as indicated by the circled parts with the red-dashed line. The top layers of the clay are forcibly and quite quickly shifted towards the edge of the scanned area. Imaging was performed with application of force 5 nN.

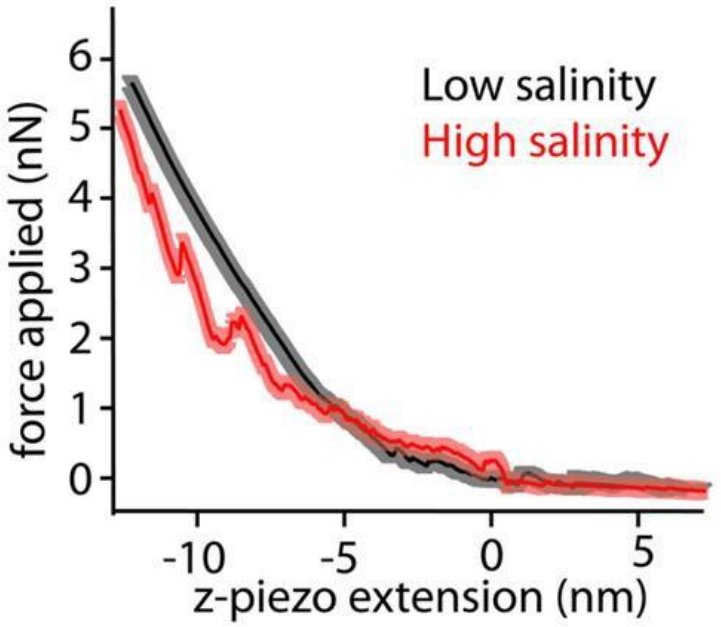

Figure 5.6: Force spectroscopy imaging shows the interface of brine and CCa-2, which was previously aged in polar model crude oil. This graph illustrates that under the high salinity condition, the clay formed multiple layers that the tip could plough through. The presence of these multiple layers are shown in the graph as multiple step-like features of the force curve. In contrast, under the low salinity condition, layering was not observed due to the higher mobility of clay. The thickness of the curves represents the standard error.

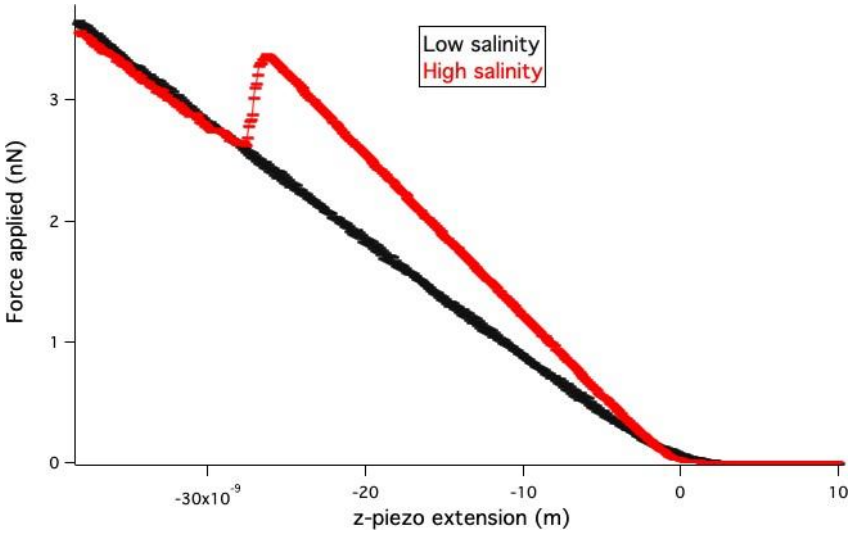

Figure 5.7: Force spectroscopy imaging shows the interface of brine and IMt-2, which was previously aged in polar model crude oil. Similar to that of figure 3.17, under the high salinity condition, the clay formed multiple layers that the tip could plough through and the presence of these multiple layers are featured in the graph as a step-like/jagged line of the force curve. In contrast, under the low salinity condition, layering was not observed due to the higher mobility of the clay. The thickness of the curves represents the standard error.

Chapter 6 Discussion

Hitherto, whilst research has been undertaken into intercalating fluorescent molecules into clay minerals, as far as can be established, no research has been undertaken into the fluorescent properties of reservoir clay minerals. In Chapter 3, the fluorescence of a range of reservoir clay minerals, as well as some other layered minerals was explored. It was shown that in the clay minerals used, fluorescence was unlikely to be owing to the presence of impurity phases and that fluorescent imaging of clay swelling, dispersion and its role in fines migration during low salinity enhanced oil recovery should be possible to investigate using fluorescent microscopy. As such, for the first time, TIRF has been used to directly image immobilised clay aggregates during salinity changes and the results from this experiment presented in Chapter 4. In order to further explore and understand the effect of salinity change upon the immobilised clay mineral films, AFM was used to understand the nanoscale properties of the clay films during brine ionic strength changes, as discussed in Chapter 5. A novel AFM method, friction force microscopy, FFM was used to explore the resilience of the clay film formed.

6.1 Use of Fluorescent Imaging in Looking at Fines Migration in EOR

The data provided in Chapter 3 evidenced that clay minerals were suitable for examination under the fluorescent microscope, yet only when certain required conditions were met. Crude oil, with its high aromatic group content, exhibited very high fluorescence, and the strength was approximately 8 times stronger than the weak natural fluorescence of clay minerals. As such, fluorescence images of clay mixed with crude oil did not clearly display the presence and location of the clay minerals. This issue of using crude oil under the fluorescence microscopy was overcome by applying a model crude oil (decanoic acid in dodecane, consistent with earlier work by the Greenwell group). However, there was a further limitation of not being able to adopt any clay minerals without considering the presence or absence of that clay sample's fluorescence.

Only 3 types of clay minerals; Na-bentonite, IMt-2 (illite) and KGa-1b (low-defect kaolinite), out of 8 clay mineral samples, were confirmed to be strong enough to be applied in confocal microscopy experiments. Of these, only KGa-1b was confirmed as having direct autofluorescence, the other 2 types of clay minerals (Na-bentonite and IMt-2) contained a large amount of mineral grains that proved difficult to decipher when attempting to determine the cause of its fluorescence. Hence, the novel approach of employing fluorescence microscopy to the observation of fines migration requires a preliminary study to test whether

or not to target the clay mineral fluorescence. Having to evaluate the properties of each set of clay mineral samples in the process will consequently consume more time before the commencement of the actual observation of the mobility of clay minerals. In addition, the target clay mineral particles might not be strong enough to fluoresce when observing their mobility in combination with other phases.

Despite these limitations, overall, the use of fluorescent images to understand fines migration can be deemed well suited, as positive results of clay mineral fines swelling and dispersion, as a precursor to fines migration, are introduced in Chapter 4.

6.1.1 Benefits of using Confocal Microscopy and Total Internal Reflectance Fluorescence (TIRF)

Nair *et al*., (2020) are most likely to have published the first paper on conducting a study of LS-EOR using confocal microscopy. Nair *et al*., (2020) employed 3D confocal Raman microscopy to acquire an xy map (Figure 6.1) and an xz map (Figure 6.2) to observe wettability alteration when ambient brine salinity shifts from high to low. Nair *et al*., (2020) stated that the benefit of 3D confocal Raman microscopy is that it allows the map shape of local microscopic oil droplets and the distribution of components in 3D. Nair *et al*., (2020) also emphasized that capturing 3D images are not observable by conventional optical CAM.

Confirming positive LS-EOR effects stemming from this project (Chapter 4) and in in consideration of CAM conducted by Nair *et al*., (2020) the argument for the potential of applying fluorescent microscopes to LS-EOR is further strengthened, In addition to this, Nair *et al*., (2020) has proven that confocal microscopy is applicable not only to fines migration but also to CAM.

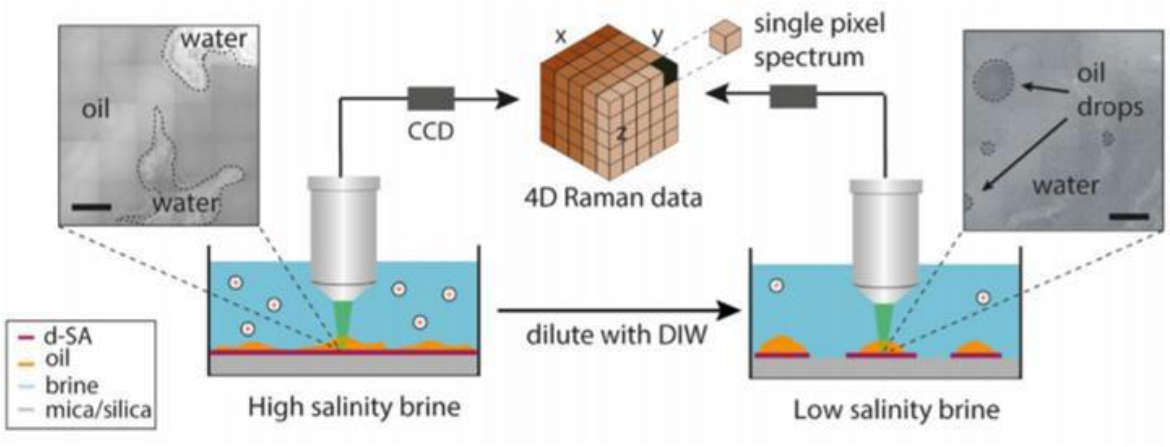

Figure 6.1: Showing the methodology of observing wettability alteration by 3D Confocal Raman Microscopy which is set as an algorithm-improved mode. The xy maps depict the distribution of oil and water under high salinity and low salinity conditions. It can be determined from the xy maps that the oil is widespread at the high salinity condition, but it changed to more of a droplet-like shape as the ambient brine changed to the low salinity brine. Hence, xy maps have shown that oil became more water-wet as the ambient brine salinity decreased. d-SA → deuterated-stearic acid (surfactant) DIW→ deionized water. the scale bar in the xy maps corresponds to 0.22mm.

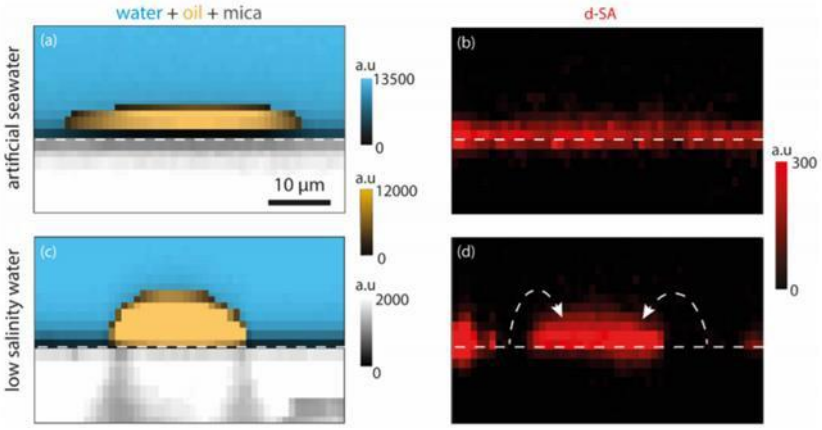

Figure 6.2: xz maps showing wettability alteration at high ambient salinity and low ambient salinity. Acquiring 3D images are required to visualize the contact angle changes and d-SA detachment and dissolution. Yellow→ oil, blue → water, grey →mica, red →d-SA.

For the use of TIRF, it can be determined based upon this study that the greatest benefit of employing TIRF is the fact that it is a non-invasive technique to image clay mineral fines swelling, dispersion and migration in real-time. The limitations of methodologies commonly utilised for the study of LS-EOR; CAM, SEM, AFM, and Micro-CT are concisely introduced in Chapter 1, '1.5.5 Limitations of Methods'. As it was noted in that section, on one hand, many surface imaging methods may allow extremely high-resolution imaging of certain surfaces and phenomena, in addition, micro-CT is able to acquire 3D images by a non-invasive method. However, micro-CT is more likely to be applicable for the study of pore-scale and core-scale experiments (Bartels *et al.*, 2017; Shabaninejadet *et al.*, 2018; Yu *et al.*, 2018), and allows for the comparison of fines migration before and after waterflooding tests (Yu *et al.*, 2018) but has hardly ever been conducted on an observation of fines migration at

micron-scale in real-time. Micro-CT has a further disadvantage in that intensities of clay minerals are very similar to the intensities of grain and pore, making it challenging to segment clays in tomogram images (Yu *et al*., 2018). Hence, in the studies in this thesis, the use of TIRF has systematically been argued for to allow even more direct evidence of fines migration in real-time at micron -scale.

Nevertheless, micron-scale results alone are insufficient and do not provide strong enough evidence to propose its sole use; thus, integrating multiple instruments, as most of the research does, would be the most optimal way of researching LS-EOR overall.

6.1.2 Use of Total Internal Reflectance Fluorescence (TIRF) to Image Clay Mineral Fines Swelling, Dispersion and Migration

The conventional ways of confirming fines migration owing to the reduction of salinity in the system are either through coreflooding to test elution of fines (Valdya and Fogler, 1992; Tang and Morrow, 1999a; Jackson *et al*., 2016; Nguyen *et al*., 2020) or by capturing SEM images of the pore-space (Fogden *et al*., 2011; Jackson *et al*., 2016). Yet still, there is very limited direct evidence, where fines were imaged during migration processes, reported (Yu *et al*., 2018). The direct monitoring of fines migration was successfully demonstrated in this present study by using images acquired with TIRF as a non-invasive technique. The results are relatively in line with results acquired with the coreflooding test as reported by Al-Sarihi and Zeinijahromi (2018).

Al-Sarihi and Zeinijahromi (2018) advocated that a reduction in permeability as salinity decreases and a notable reduction of permeability is initiated when the salinity in the system is reduced from 35,000 mg/L to 6,000 mg/L and dramatic formation damage was witnessed at a salinity of 750 mg/L (Figure 6.3).

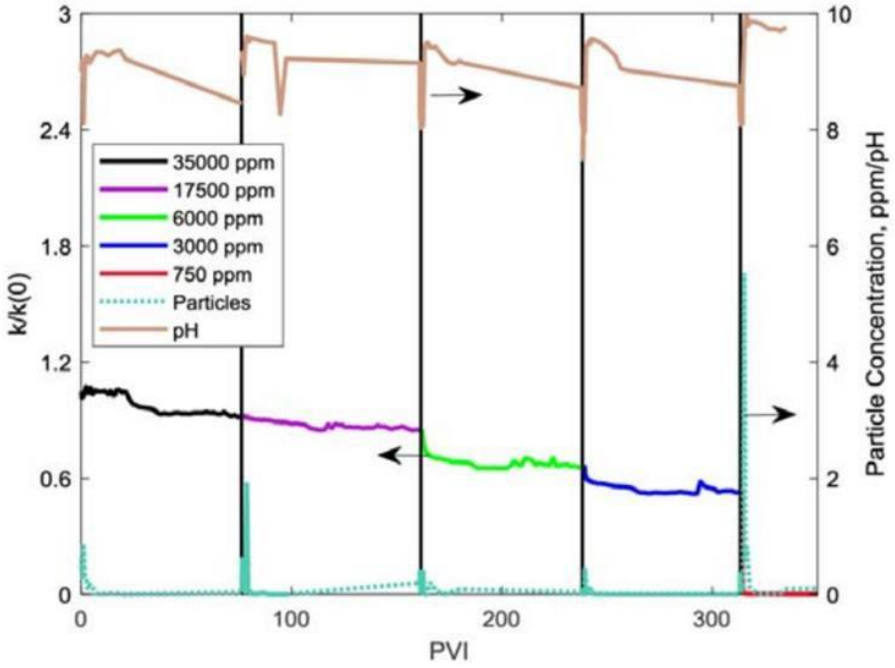

Figure 6.3: Permeability reduction, fine particles production, and the increment of pH which are measured by lowering salinity are revealed from the coreflooding test conducted by Al-Sarihi and Zeinijahromi (2018). PVI →Pore Volume Injected k→Permeability

Based upon the results proposed in Chapter 4, swelling of clay minerals commenced straight after immersion in high salinity water of total ionic strength of 0.69 M, the clay minerals continued to swell as the salinity level decreased. Fines dispersion and migration, notably initiated under TIRF, took place after the fourfold dilution of salinity, fourfold dilution of 35,000 mg/L is approximately 8,750 mg/L. Considering that both experiments were conducted by reducing the salinity step-wise, observation of fines migration initially at fourfold dilution would equate approximately to 8,750 mg/L which is consistent with observing initial notable permeability reduction at 6,000 mg/L (Al-Sarihi and Zeinijahromi, 2018). However, the salinity range for inducing LS-EOR is generaly considered to be between 1,000 mg/L and 2,000 mg/L, and a positive LS-EOR effect was confirmed up to 5,000 mg/L, with no oil recovery confirmed at 7,000 mg/L according to Austad *et al* (2010) and Chavan *et al*., (2019). Hence, fourfold dilution is still theoretically a high ionic concentration to observe LS-EOR, but it could also be interpreted that fines dispersion and migration could initiate at a higher salinity than the optimal salinity, while the emulsion phase formed and oil molecule surface release may require a much lower ionic concentration in order to enable residual oil recovery.

It is also worth noting that the typical ocean salinity is 35,000 mg/L as introduced in Table 1.1 and 35,000 mg/L brine is the initial salinity state applied by Al-Sarihi and Zeinijahromi (2018). High salinity water employed for this project is the total ionic strength of 0.69 M, which is almost equal to the typical ionic strength of ocean water of 0.7M (Ryan, n.d.). Therefore, the initial salinity level for the test under the TIRF and the coreflooding test

conducted by Al-Sarihi and Zeinijahromi (2018) would have been very similar.
More study is required to confirm the interpretation since not many researchers have tested which salinity level initiates fines dispersion and migration, most of the research papers have confirmed fines dispersion and migration in line with permeability reduction by lowering salinity, which consequently resulted in an increase in recovery rate of residual oil (Valdya and Fogler, 1992; Nguyen *et al*., 2020).

6.1.3 Probing the Effect of Non-Polar Oil on Clay Mineral Fines Swelling and Dispersion

Dispersion and migration of clay minerals preliminarily aged with non-polar crude oil was successfully reported by not only applied TIRF in this study, but also AFM as a result of this study and this is in alignment with core-flooding tests undertaken by Al-Sarihi and Zeinijahromi (2018). Al-Sarihi and Zeinijahromi (2018) intentionally applied non-polar crude oil in order to confirm fines migration and hence the subsequent permeability reduction as the independent mechanism is not attributed to wettability alteration by lowering the salinity level. Amott tests initially confirmed that the core of Berea rocks were water-wet and further determined the wettability index calculated with Equation 3.

$$WI = \frac{V_{osp}}{V_{ot}} - \frac{V_{wsp}}{V_{wt}} \qquad \text{Equation}$$

Where V_{osp} was the volume of oil displaced spontaneously, V_{ot} was the total volume of oil displaced by imbibition and force displacement, $V_{wsp}$was the volume of water displaced spontaneously, and V_{wt} was the total volume of water displaced by drainage and forced displacement (Al-Sarihi and Zeinijahromi 2018). Due to the fact that the wettability index for high salinity water and low salinity water indicated almost the same number, 0.98 and 0.99 respectively, Al-Sarihi and Zeinijahromi (2018) therefore highlighted that wettability alteration would not have been undertaken during the coreflooding test with low salinity water and some other mechanism, for example fines migration, must have been responsible for any EOR effect. Hence, this seems contradictory to the model advocated by Tang and Morrow (1999a) for the formation of oil-wet or a mixed-wet surface before fines dispersion commences. As a consequence of integrating interpretation from Al-Sarihi and Zeinijahromi (2018), fines dispersion and migration pictured in Figure 4.1 and Figure 4.2 are merely due to the weaker electrostatic forces developed by lowering the salinity in the system. Furthermore, Maskari *et al*., (2019) witnessed the wettability alteration of non-polar model oil on a carbonate surface, as pH values increased from pH 6.5 to pH 9.5 and pH 11. CAM, AFM adhesion force measurement between the non-polar oil and calcite surface, and zeta

potential measurements of the non-polar oil-brine and brine-calcite interfaces were all conducted in the presence of 10,000 mg/L NaCl, with only changed pH values. CAM revealed a more water-wet surface, AFM revealed a decreased adhesion force, and the zeta potential showed more negative values as the pH levels increased. Integrating results from all the three instruments, Maskari *et al*., (2019) concluded that detachment of non-polar model oil from a carbonate rock surface by altering wettability could take place, it also shed light on the importance of pH values variation on a carbonate surface adhered with non-polar model oil.

Non-polar oil is widely acknowledged as being non-effective in terms of exhibiting LS-EOR effects, and thus of limited use for application in the study of LS-EOR (Austad *et al*., 2010; Jackson *et al*., 2016). However, recently published results (Al-Sarihi and Zeinijahromi 2018; Maskari *et al*., 2019), and the TIRF and AFM results in this thesis, of observing fines migration after ageing with non-polar model oil are significant, and these results produce further insight into the field of LS-EOR, which also suggests polar components are not the dominant components for LS-EOR effects and that there is likely to be a subtle balance of effects arising owing to surface wettability alteration and those arising due to fines migration.

6.2 Can Atomic Force Microscopy (AFM) and Friction Force Microscopy Give Quantitative Insight Into The Low Salinity Enhanced Oil Recovery Process?

As aforementioned in Chapter 5 '5.2 Methods', the advantage of utilising AFM compared to TIRF is that any type of clay mineral is applicable regardless of the fluorescence intensity, this includes CCa-2 (chlorite) which did not fluoresce enough to be tested using the TIRF when investigating its force friction microscopy (FFM). On the other hand, AFM is not a non-destructive method, as the AFM probe makes contact with the sample surface there is a very real possibility of causing damage to the samples and not acquiring accurate results. Nonetheless myriad research has been undertaken on LS-EOR (Hassenkam *et al*., 2011; Hassenkam *et al*., 2012; Siretanu *et al*., 2014; Matthiesen *et al*., 2014; Hilner *et al*., 2015; Yang *et al*., 2015; Al Maskari, *et al*., 2019). The standard method for applying AFM for the study of LS-EOR measures adhesion force between functional tip and samples which leads to an understanding of the interaction between mineral, water and crude oil under different salinity conditions.

In the case of observing a decrease in adhesion force on mineral surfaces, it is determined that this is due to expansion of the electrical double layer, which much research indicates as

one of the mechanisms of the LS-EOR effects (Hassenkam *et al*., 2011; Hassenkam *et al*., 2012; Matthiesen *et al*., 2014; Jackson *et al*., 2016; Al Maskari, *et al*., 2019). Meanwhile, Yang *et al*., (2015) captured topography images of the asphaltene-coated surface and its histograms of point height (Figure 1.20) under various salinity levels to confirm the LS-EOR effect. This is the first time of trying to quantify changes in an attached film of clay as an effect of low salinity and exhibited an effect in terms of imaging, and in terms of the force required to generate displacement of the film. Hassenkam *et al*., (2011) and Hassenkam *et al*., (2012) noted based upon their AFM testing that only a 0% to 2% of adhesion change on the illite surface were observed and this is significantly low compared to the response on silicate surface, which has decreased to 20% to 30% of adhesion force. However, our AFM images denoted that the IMt-2 sample aged with polar model oil was successfully dispersed as salinity decreased from the total ionic strength of 0.69 M to 0.02 M. The contribution of illite clay mineral to EOR effects is also supported by the work of Al Maskari, *et al*. (2019). Al Maskari, *et al*., (2019) confirmed LS-EOR effects by measuring adhesion force between muscovite and functional groups of $-CH_3$ and -COOH; only varying the pH values, tested under either pH 7 or pH 11 conditions, and applied ambient salinity of 1,000 mg/L NaCl for both pH values. Al Maskari, *et al*. (2019) has previously confirmed the increment of pH values when injecting low salinity brine to a system with basal-charged clays, such as illite, chlorite, and smectite (Chen *et al*., 2018). Thus, Al Maskari, *et al*. (2019) has hypothesised that the increase of pH leads to a more negative zeta potential for oil-brine and brine-clay, subsequently triggering increases in DLE. The experiments conducted by Al Maskari, *et al*., (2019) consequently revealed that 80% of adhesion force decreased as the pH increased from 7 to 11 for both $-CH_3$ and -COOH functional groups. In summary then, when considering AFM measurements, Zeta potential measurements and computing total disjoining pressure, Al Maskari *et al*. (2019) clarified the determination of basal-charged clays as certainly contributing to DLE, which is one of the LS-EOR mechanisms.

Our experiment reduced the salinity level, without considering other external factors such as pH levels and temperature, yet clay dispersion was recorded regardless of the oil types (polar and non-polar model oil) and clay types. Incorporating results from the project and published papers (Hassenkam *et al*., 2011; Hassenkam *et al*., 2012; Siretanu *et al*., 2014; Matthiesen *et al*., 2014; Hilner *et al*., 2015; Yang *et al*., 2015; Al Maskari, *et al*., 2019), it is arguable that the attribution of fines migration by lowering salinity is due to the electrical double layer expansion which can be explained by DLVO theory (also referred to in chapter 1 '1.4.3 Electric Double Layer (EDL) Effects'), also the pH level is increased by injecting low salinity water into the system (also referred to in chapter 1 '1.4.1 pH Effects' and this is likely to be an appreciable influence. This is due to the fact that the study reported similar

results as those reported in this thesis, i.e. non-polar oil has little effect on fines dispersion, providing a mechanism by which oil may be released irrespective of the polar oil components in the oil and that permeability reduction may result from fines migration and observed by lowering the salinity level (Al-Sarihi and Zeinijahromi, 2018). Also, measurements of pH variation were undertaken and it was confirmed that the increment of pH lowered the salinity (Figure 6.3). However, this discussion is still speculative because we have not tested the pH measurements, so consideration of external factors that might affect LS-EOR effects would be required for further study.

Chapter 7 Conclusion & Further Studies

Realised in field-scale trials, low salinity enhanced oil recovery has been studied extensively for a number of years. Numerous core-flood experiments have constrained conditions under which LS-EOR may be observed, and in recent years there has been an increasing research effort in understanding the fundamental mechanisms occurring at mineral interfaces that may underpin wettability alteration. Such studies are necessary owing to the present lack of predictability over whether LS-EOR may be successful on any given oil reservoir. However, while chemical force microscopy has begun to offer nanoscale insight, the reproducibility is challenging and it is also an invasive contact technique where the experiment may generate many artefacts (Santha *et al*., 2019). In this thesis, the use of non-contact confocal fluorescence microscopy is studied. To aid to quantification of these studies, friction force microscopy was investigated as a possible way to understand changes in the behaviour of clay films at quartz surfaces.

Based on the results of this study, the following conclusions can be made:

- Owing to the fluorescence intensity of glass slides, tap water and brine being negligible, and for brine, the fluorescence intensity was not affected even though its salinity was altered, fluorescence microscopy was able to be used to study clay mineral systems.

- There was no significant fluorescence intensity difference between heavy BP crude oil and light Hardstoft crude oil; both crude oil showed approximately 4000 intensity, and this implied that the fluorescence intensity of crude oil is not influenced by their physical properties, such as viscosity and the colour. The exceedingly strong fluorescence intensity of crude oil was determined to be about eight times higher than the average fluorescence intensity of the clay minerals studied, meaning that real crude oil is not possible to use where the behaviour of the underlying clay minerals needs to be studied.

- The fluorescent intensity of a model crude oil; a mixture of polar dodecanoic acid and non-polar *n*-dodecane recorded negligible fluorescence intensity, and allowed imaging of the presence of clay minerals, while maintaining approximate physical properties and wettability of a simple crude oil. The result marks an advancement in the progress for further study of clay migrations under fluorescence microscopy.

- As a result of the comparison between 8 different types of clay minerals in terms of fluorescence intensity and the fluoresced scope, Na-bentonite recorded the highest intensity

and KGa-1(low-defect kaolinite) has recorded the lowest intensity. Nevertheless, KGa-1b exhibited the second widest fluoresced scope; thus, KGa-1b is one of the most accessible clay minerals to confirm their presence. Due to the fact that the facileness of detecting clay minerals is more important than the strength of their fluorescence intensity, Na-Bentonite, IMt-2(illite) and KGa-1b are predominant clay minerals for further study of TIRF.

- In order to understand the factors affecting the fluorescence of clay minerals, fluorescent intensity and fluoresced scope of high-defect kaolinite and low defect kaolinite were compared. Although low-defect kaolinite exhibited slightly lower fluorescence intensity than high defect kaolinite, it was much easier to detect low-defect kaolinite under the confocal microscope due to the fact that well-crystallised low-defect kaolinite is more uniform, in terms of their fluorescence intensity.

We presumed that defect states in the band gap for kaolinite contained defects where oxygen replaced hydrogen in one of the Al (001)-hydroxyl groups of the kaolinite clay sheets; decreasing the band gap by about 3.2 eV, and thus fluorescence may be observed.

- Investigation of any fluorescence changes before and after ion exchange of sodium and calcium were undertaken. Post-ion exchange, clay with a higher quantity of calcium displayed a slightly wider fluoresced scope yet, there was no systematic significant difference between the fluorescent intensity of pre and post-ion exchange.

- The fluorescence intensity and the fluoresced scope of LDH Mg/Al and LDH Mg/Fe were assessed. There was no correlation for LDH Mg/Al, whereas LDH Mg/Fe exhibited a higher fluoresced intensity and wider fluoresced scope as the amount of iron in the clay increases. Hence, the quantity of iron in clay samples controls the fluorescence intensity and fluoresced scope.

- Based upon SEM imaging, it was confirmed through visual inspection of crystal morphology that all the clay samples other than KGa-1b contained impurity minerals; KGa-1 only consisted of approximately 32% of a significantly large mineral grain that could possibly be due to having been blended from a different source whereas, SCa-3(Montmorillonite) consisted of approximately 57% of non-clay large minerals. SWy-2(Na-rich montmorillonite), SCa-3, and Na-Bentonite detected a similar variety of mineral grains as compared to the SCa-3 electron micrograph.

- Quantitative XRD data was acquired in the interest of further understanding the cause of

fluorescence of the clay mineral samples, and this data was compared with the obtained SEM data. For KGa-1b, it was considered that KGa-1b itself might be fluorescing since the percentage of fluoresced pixels were more than the percentage of impurity minerals that would fluoresce at the applied wavelength. For KGa-2 (high-defect kaolinite), the percentage of impurities being analogous compared to KGa-1, meant that the difference in fluorescence features are attributed to the physical properties rather than the chemical composition.
SCa-3 was analysed by XRD to quantify the bulk composition of the sample for the three types of clay. It can be determined that most of the minerals detected as non-clay minerals under the XRD were perhaps an aggregation of clay minerals and only quantified total non-clay minerals of 15.2%, whereas SEM images detected 57% of non-clay minerals. Therefore, it is challenging to identify the difference between non-clay minerals and aggregation of clay minerals under the optical microscope. Yet, with both SCa-3 and Na-bentonite there is a wider variety of non-clay minerals, making the task of attributing sources of fluorescence more complex, especially for fluorescence of pure clay minerals, which has not yet been tested to a high degree. Hence, it was speculated that KGa-1b might be the only clay sample that has the potential of autofluorescence.

- TIRF tracked the movement of clay minerals during an experiment in brine, where the salinity was decreased in the system. High salinity water was added immediately after monitoring commenced and swelling of clay minerals was confirmed at the same time as placing high salinity water in the sample. Subsequently, adding deionsed water into the sample every 5 minutes decreased the ionic concentration. As a result, after 10 minutes of starting the experiments, after a fourfold dilution of salinity, clay swelling became more prominent and clay minerals that initially had not moved at all then began to show dynamic motion. There were no significant changes observed, not even further diluted salinity in the system. The experiments on the TIRF also confirmed positive LS-EOR effects from clay minerals initially aged with non-polar crude oil. This suggests that fines migration may contribute to LS-EOR alongside or without needing cation bridging to be disrupted between the clay mineral and oil components.

- The AFM data from studying alteration in clay thin films also demonstrated LS-EOR relevant effects. The uneven, discernible individual clay crystals visible at a high salinity condition became a more homogeneous, gel-like clay surface under low salinity conditions. These successful outcomes were demonstrated by data from amplitude modulation imaging, friction force microscopy and force spectroscopy that investigated the interface of brine and the structural transition of the clay layers which were attributed to the detachment of adhered

clay by lowering the salinity. Three types of clay minerals were employed for this experiment; KGa-1b, CCa-2(chlorite), and IMt-2. It is worth mentioning that a positive LS-EOR effect was confirmed when not only aged with polar crude oil but also with non-polar crude oil.

- The following main points were revealed at the conclusion of this research program. First, fines migration under fluorescent microscopy was successfully recorded. However, with application of the TIRF, which is both a novel instrument and method, preliminary research was required to test whether or not to target the clay fluorescence, and this process will consequently consume more time before the commencement of the actual observation. In addition to that, the target clay might not be strong enough to fluoresce using fluorescent microscopy. Moreover, application of a substance which has stronger fluorescent intensity (e.g. crude oil) than clay minerals has the possibility of disturbing the presence of any clay mineral under fluorescent microscopy thus, it is mandatory to understand the fluorescence strength of all the equipment which will be utilised and the substances which will be tested as samples and placed under fluorescent microscopy.

- The indirect methods of either the coreflooding to test elution of fines or capturing SEM images of the pore-space are typically provided as evidence for fines migration, yet direct observation is hardly ever utilised for recording fines migration. For this project, TIRF was able to monitor the swelling of clay minerals and fines migration in real-time. Furthermore, it was also possible to record the optimal salinity for clay to start moving vigorously: fourfold dilution of high salinity water.

- The high salinity water created for this research project is the total ionic strength of 0.69 M, which is almost the same ionic strength of the ocean (approximately 0.7 M). The average ionic concentration of the ocean in mg/L is about 35,000 mg/L (Table 1.1) so simply converting that fourfold dilution would be 8750 mg/L. Thus, it can be determined that the vigorous migration of clay once observation commenced at salinity of 8750 mg/L, is relatively consistent with the result observed at initiation of permeability reduction at 6,000 mg/L (Al-Sarihi and Zeinijahromi 2018) especially if permeability reduction is undertaken after the occurrence of fines migration. Nevertheless, both ionic concentration of initiated fines migration and permeability reduction as discussed by Al-Sarihi and Zeinijahromi (2018) are much higher than the salinity range for LS-EOR, which benefits from a range of between 1,000 mg/L to 2,000 mg/L.

- Meanwhile, in observing permeability reduction by utilising non-polar oil, the work of Al-Sarihi and Zeinijahromi, (2018) is also consistent with our results, which confirmed the swelling of fine and fines migration with non-polar model oil. Based upon the research conducted by Al-Sarihi and Zeinijahromi (2018), it was concluded that applying non-polar oil would prevent wettability alteration by lowering the salinity, and recorded an identical wettability index at both high salinity and low salinity conditions, which made manifest that the observed permeability reduction and fines migration would not have been attributed to altering both the oil-wet and mixed-wet state. This should instead be attributed to weaker electrostatic forces by lowering the salinity. Positive LS-EOR effects by applying non-polar oil would have reported not only fines migration and permeability reduction but also wettability alteration at a carbonate reservoir (Maskari *et al*., 2019). Hence, perhaps the polar component may not play an essential role in LS-EOR effects.

- AFM is one of the most common instruments utilised in the application of the study of LS-EOR, and the conventional way of employing AFM is to measure adhesion force between functionalised AFM tips and the sample to verify the EOR effects. Yet, for the purposes of this project, for the first time, clay films were created and the swelling was observed as the fines were dispersed and the salinity decreased. As a consequence, AFM shows that CCa-2, KGa-1b, as well as Na-Bentonite, all form a disperse/ gel-like state once the change from high salinity to low salinity has been effected. FFM displayed CCa-2 under low salinity conditions, which was much more easily probed through the sample for comparison to CCa-2 under the high salinity conditions and disturbed by the stronger electrostatic forces.

- It is arguable based upon these results that swelling of clay minerals and fines migration as witnessed from the AFM and TIRF tests would have been most dominantly been attributed to the electrical double layer expansion, which can be explained by DLVO theory. Meanwhile, the increments of pH would also influence to the LS-EOR effects, however, further study is required to confirm the latter mechanism as the project did not consider the change in pH values.

Further Study

The national-wide lockdown with the associated access restrictions to the laboratories due to the COVID-19 pandemic resulted in very limited access to conduct the research presented here in this thesis. The extended research period consequently allowed for the completion of all the experiments initially planned, though only 1 or 2 repetitions or sets of samples were able to be tested, rather than the more complete range of experiments. Additionally, some parts of the experiments had to be entrusted to staff within the university, which rendered it impossible to become as familiar or involved with the operation of some of the experimental instruments than desired or envisaged. However, at the same time, some of the data which we did not plan to acquire, such as AFM and XRD, were obtained through this slightly different process of conducting the experiments as the restrictions of the lockdown became relaxed.

The following elements should be explored in order to further this study:

1) For the AFM experiments, there is uncertainty of whether the dispersion of clay minerals was due to the probe scanning motion, or due to swelling through low salinity effects. As shown in Figure 7.1 (a), clay minerals were not firmly adhering to the substrate due to the samples, which were prepared with a very high loading of clay minerals. Low adhesion of clay minerals was demonstrated in Figure 7.1 (b), detachment of clay from the substrate was witnessed immediately after being immersed in liquid. Therefore, more time could be spent on optimising clay mineral deposition into different thickness evenly structured films. A more systematic study of the role of salinity should also be tested when performing the AFM experiments.

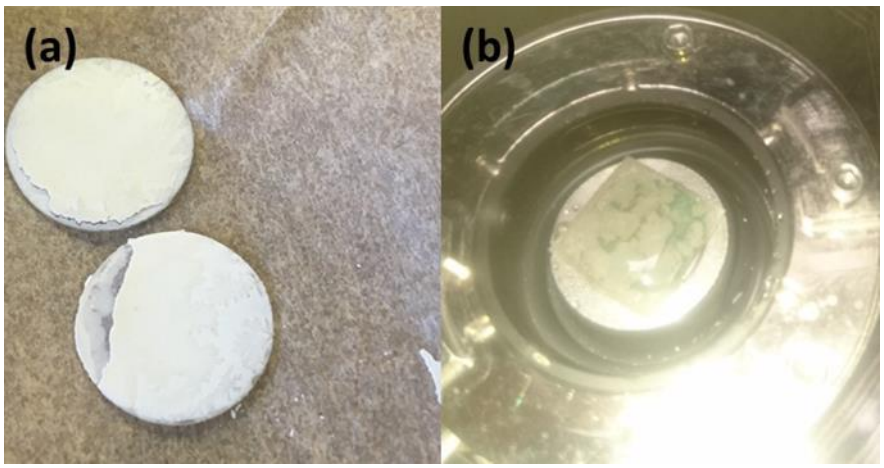

Figure 7.1: (a) The AFM samples before being immersed in liquid; Na-Bentonite clay on top and CCa-2 at the bottom. (b) some parts of clay minerals were detached from the substrate immediately after immersion in liquid; therefore, this resulted in the sample not being in optimal imaging condition.

2) Also for the AFM experiments, comparison of only two salinity levels (high and low salinity) were undertaken, yet testing multiple salinity levels, such as would be conducted for the TIRF would be beneficial in order to compare the results acquired from TIRF. Since better oil recovery with application of distilled water compared with employing 15% NaCl solution is already confirmed by Bernard (1967), investigating zero salinity water by using AFM and TIRF would also be interesting in understanding further LS-EOR mechanisms.

3) As the initial TIRF experiments were successful in demonstrating the swelling of clay minerals, with additional evidence of clay mineral dispersion. In order to observe fines migration followed by permeability reduction, more complex flow cell micromodels consisting of etched slides that replicate pores in sandstone would be obtained (Song and Kovscek, 2016). These would have clay minerals deposited in the pores and aged in model oil/formation water. Experiments to observe fines migration at low-salinity and high-salinity conditions under TIRF would then be carried out.

4) By consulting previous research conducted by other authors, emulsions (Nguyen *et al*., 2014) and oil (Shende *et al*., 2016) have been investigated in separate studies under the fluorescent microscope, yet it is unprecedented to investigate the formation of emulsion and its movement under fluorescent microscopy. In recent years, a mechanism for LS-EOR, where formation of emulsion at a low-salinity condition occurs, is gaining more attention (Aldousary and Kovscek, 2019; Morishita *et al*., 2020; Duboué *et al*., 2020). Through scrutinizing not only fines migration but also the generation and migration of stable emulsions under low salinity conditions using fluorescent microscopy would contribute to understanding LS-EOR mechanisms in more depth.

References

Akin, S. and Kovscek, A., 2003. Computed tomography in petroleum engineering research. Geological Society, London, *Special Publications*, **215**, pp.23-38.

Alameri, W., Teklu, T., Graves, R., Kazemi, H. and AlSumaiti, A., 2015. Experimental and Numerical Modeling of Low-Salinity Waterflood in a Low Permeability Carbonate Reservoir. *Society of Petroleum Engineers Journal*, pp. 1-17.

Aldousary, S. and Kovscek, A., 2019. The diffusion of water through oil contributes to spontaneous emulsification during low salinity waterflooding. *Journal of Petroleum Science and Engineering*, **179**, pp.606-614.

Allsman, O., 2021. 1.9A: Ground state electronic Configuration. [online] Chemistry LibreTexts. Available at: <https://chem.libretexts.org/Bookshelves/Inorganic_Chemistry/Map%3A_Inorganic_Chemistry_(Housecroft)/01%3A_Basic_concepts%3A_atoms/1.09%3A_The_Aufbau_Principle/1.9A%3A_Ground_state_electronic_Configuration> [Accessed 18 February 2021].

Al Maskari, N., Xie, Q. and Saeedi, A., 2019. Role of Basal-Charged Clays in Low Salinity Effect in Sandstone Reservoirs: Adhesion Force on Muscovite using Atomic Force Microscope. *Energy & Fuels*, **33**, pp.756-764.

Alvarado, V. and Manrique, E. 2010. Enhanced Oil Recovery: An Update Review. *Energies*, **3**, pp.1529-1575.

Al-Saedi, H. and Flori, R., 2018. Enhanced oil recovery of low salinity water flooding in sandstone and the role of clay. *Petroleum Exploration and Development*, **45**, pp.927-931.

Al-Saedi, H., Brady, P., Flori, R. and Heidari, P., 2018. Novel Insights into Low Salinity Water Flooding Enhanced Oil Recovery in Sandstone: The Clay Role Study. *Society of Petroleum Engineers*, pp.1-18.

Al-Saedi, H., Flori, R. and Brady, P., 2019. Effect of divalent cations in formation water on wettability alteration during low salinity water flooding in sandstone reservoirs: Oil recovery analyses, surface reactivity tests, contact angle, and spontaneous imbibition experiments. *Journal of Molecular Liquids*, **275**, pp.163-172.

Al-Sarihi, A., Zeinijahromi, A. and Bedrikovetsky, P., 2018. Low-salinity waterflooding in non-polar oil. *The APPEA Journal*, **58**, p.660-663

Al-Sarihi, A., Zeinijahromi, A., Genolet, L., Behr, A., Kowollik, P. and Bedrikovetsky, P., 2018. Effects of Fines Migration on Residual Oil during Low-Salinity Waterflooding. *Energy & Fuels*, **32**, pp.8296-8309.

Al-Mjeni, R., Arora, S., Cherukupalli, P., Wunnik, J., Edwards, J., Felber, B., Gurpinar, O., Hirasaki, G., Miller, C., Jackson, C., Kristensen, M., Lim, F. and Ramamoorthy, R., 2011.

Has The Time Come For EOR?. [ebook] Schlumberger, pp.16-35. Available at: <https://pdfs.semanticscholar.org/f4e7/756c8b0362bb1544456971567ae7bd1d9bb6.pdf> [Accessed 30 December 2020].

Al-Nofli, K., Pourafshary, P., Mosavat, N. and Shafiei, A., 2018. Effect of Initial Wettability on Performance of Smart Water Flooding in Carbonate Reservoirs—An Experimental Investigation with IOR Implications. *Energies*, **11**, p.1394.

Aminzadeh, F. and Dasgupta, S., 2013. Geophysics for petroleum engineers. Elsevier, pp.15-36.

Anderson, W. 1986. Wettability Literature Survey- Part 1: Rock/Oil/Brine Interactions and the Effects of Core Handling on Wettability. *Journal of Petroleum Technology*, **38**, pp.1125-1144.

Austad, T., RezaeiDoust, A. and Puntervold, T., 2010. Chemical Mechanism of Low Salinity Water Flooding in Sandstone Reservoirs. *Society of Petroleum Engineers*, pp.1-17.

Austad, T., Shariatpanahi, S., Strand, S., Black, C. and Webb, K., 2011. Conditions for a Low-Salinity Enhanced Oil Recovery (EOR) Effect in Carbonate Oil Reservoirs. *Energy & Fuels*, **26**, pp.569-575.

Basheer, C., 2013. Application of Titanium Dioxide-Graphene Composite Material for Photocatalytic Degradation of Alkylphenols. *Journal of Chemistry*, **2013**, pp.1-10.

Bagnell, A., 2018. What Is Micro-CT? An Introduction | Micro Photonics. [online] Micro Photonics Inc. Available at: <https://www.microphotonics.com/what-is-micro-ct-an-introduction/> [Accessed 31 December 2020].

Bartels, W., Rücker, M., Berg, S., Mahani, H., Georgiadis, A., Brussee, N., Coorn, A., van der Linde, H., Fadili, A., Hinz, C., Jacob, A., Wagner, C., Henkel, S., Enzmann, F., Bonnin, A., Stampanoni, M., Ott, H., Blunt, M. and Hassanizadeh, S., 2016. Micro-CT Study of the Impact of Low Salinity Waterflooding on the Pore-Scale Fluid Distribution During Flow. *International Symposium of the Society of Core Analysts*, pp.1-12.

Bartels, W., Rücker, M., Berg, S., Mahani, H., Georgiadis, A., Fadili, A., Brussee, N., Coorn, A., van der Linde, H., Hinz, C., Jacob, A., Wagner, C., Henkel, S., Enzmann, F., Bonnin, A., Stampanoni, M., Ott, H., Blunt, M. and Hassanizadeh, S., 2017. Fast X-Ray Micro-CT Study of the Impact of Brine Salinity on the Pore-Scale Fluid Distribution During Waterfooding. *Petrophysics*, pp.36–47.

Bernard, G., 1967. Effect of Floodwater Salinity on Recovery of Oil from Cores Containing Clays. SPE California Regional Meeting, pp.1-8.

Bhui, U. and Sanyal, S., 2017. Wettability Alteration Of Kaolinte During Low Saline Water Flooding: A Study Based On Scanning Electron Microscopy. [ebook] EMSI 2017 Proceedings XXXVIII Annual Meeting of EMSI, pp.1-3. Available at:

<https://www.researchgate.net/profile/Saheli_Sanyal2/publication/319207666_Wettability_alteration_of_kaolinite_during_low_saline_water_flooding_A_study_based_on_Scanning_Electron_Microscopy/links/599bd3ff0f7e9b892bad240d/Wettability-alteration-of-kaolinite-during-low-saline-water-flooding-A-study-based-on-Scanning-Electron-Microscopy.pdf> [Accessed 31 December 2020].

Binnig, G., Quate, C. and Gerbe, C., 1986. Atomic Force Microscope. Physical Review Letters, pp.930-933.

Boerckel, J., Mason, D., McDermott, A. and Alsberg, E., 2014. Microcomputed tomography: approaches and applications in bioengineering. *Stem Cell Research & Therapy*, **5**, p.1-12.

2019. BP Energy Outlook 2019 Edition. [ebook] © BP p.l.c. 2019, p.15. Available at: <https://www.bp.com/content/dam/bp/business-sites/en/global/corporate/pdfs/energy-economics/energy-outlook/bp-energy-outlook-2019.pdf> [Accessed 30 December 2020].

Brindley, G., 1981. Clays, Clay Minerals. 1st ed. Boston, MA.: Encyclopedia of Earth Science. Springer.

Buckman JO, Todd AC, Hill PI., 2000. Observations on reservoir rock wettability using an environmental scanning electron microscope. *Microsc Anal*, p.35–37

Burruss, R., 1991. Practical Aspects Of Fluorescence Microscopy Of Petroleum Fluid Inclusions. Society for Sedimentary Geology: Luminescence Microscopy and Spectroscopy: Qualitative and Quantitative Applications.

Chau, T. (2009). A review of techniques for measurement of contact angles and their applicability on mineral surfaces. *Minerals Engineering*, **22**, pp.213-219.

Chavan, M., Dandekar, A., Patil, S. and Khataniar, S., 2019. Low-salinity-based enhanced oil recovery literature review and associated screening criteria. *Petroleum Science*, **16**, pp.1344-1360.

Chisholm, K., 2015. 144 Products Made From Petroleum And 4 That May Shock You. [online] Available at: <https://innovativewealth.com/inflation-monitor/what-products-made-from-petroleum-outside-of-gasoline/> [Accessed 10 February 2021].

Cockcroft, P., Anli, J. and Duignan, J., 1988. EOR Potential of Indonesian Reservoirs. *Indonesian Petroleum Association*, **2**, pp.73-108.

Cpb-us-e1.wpmucdn.com., 2019. Basic Operating Principles Scanning Electron Microscope User Training. [online] Available at: https://cpb-us-e1.wpmucdn.com/wp.wwu.edu/dist/d/1295/files/2014/01/sem-training-2.pdf [Accessed 22 Oct. 2019].

Craig, J., Gluyas, J., Laing, C. and Schofield, P., 2013. Hardstoft-Britain's First Oil Field. *Petroleum History Institute*, **14**, pp.97-116.

C&I Co., Ltd., n.d. What Is Waveguide-Mode Technology ?. [online] Technology. Available

at: <https://www.candi-wgm.com/technology/index.html#technology05> [Accessed 31 December 2020].

Dennis, H., Baillie, J., Holt, T. and Wessel-Berg, D., 2000. Hydrodynamic activity and tilted oil-water contacts in the North Sea. *Elsevier*, **9**, pp.171-185.

Desmond, J., Juhl, K., Hassenkam, T., Stipp, S., Walsh, T. and Rodger, P., 2017. Organic-Silica Interactions in Saline: Elucidating the Structural Influence of Calcium in Low-Salinity Enhanced Oil Recovery. *Scientific Reports*, **7**, pp.1-14.

Digimsolution.com. (2019). DigiM - Digital Microstructure - Micro-CT Imaging Platform. [online] Available at: https://digimsolution.com/services/microct-imaging-platform/ [Accessed 28 Oct. 2019].

Duboué, J., Bourrel, M., Dusautoir, T., Santanach Carreras, E., Klimenko, A., Agenet, N., Passade-Boupat, N. and Lequeux, F., 2020. Fundamental Investigation of Auto-Emulsification of Water in Crude Oil: An Interfacial Phenomenon and its Pertinence for Low Salinity EOR. Society of Petroleum Engineers, pp.1-17.

Fang, Z., Cao, R., Zhang, F., Ma, Z., Dong, G. and Qiu, J., 2014. Efficient spectral conversion from visible to near-infrared in transparent glass ceramics containing Ce3+–Yb3+codoped Y3Al5O12nanocrystals. *J. Mater. Chem. C*, **2**, pp.2204-2211.

Fears, D. and Clement, S., 2019. Americans would rather reduce oil and gas exploration than 'drill, baby, drill'. [online] Available at: <https://www.washingtonpost.com/climate-environment/2019/10/25/americans-would-rather-reduce-oil-gas-exploration-than-drill-baby-drill/> [Accessed 16 February 2021].

Fındık, S., 2018. Treatment of petroleum refinery effluent using ultrasonic irradiation. *Polish Journal of Chemical Technology*, **20**, pp.20-25.

Fines Migration - Schlumberger Oilfield Glossary. [online] Available at: https://www.glossary.oilfield.slb.com/en/Terms/f/fines_migration.aspx [Accessed 1 December 2020].

Flowers, P., Theopold, K., Langley, R. and Blauch, D., 2020. 24.7: Color and the Colors of Complexes. [online] Chemistry LibreTexts. Available at: <https://chem.libretexts.org/Bookshelves/General_Chemistry/Map%3A_General_Chemistry_(Petrucci_et_al.)/24%3A_Complex_Ions_and_Coordination_Compounds/24.07%3A_Color_and_the_Colors_of_Complexes> [Accessed 18 February 2021].

Forster, A., Mclnnes, J., Skingle, D. and Symons, R., 1985. Non-radioactive hybridization probes prepared by the chemical labelling of DNA and RNA with a novel reagent, photobiotin. *Nucleic Acids Research*, **13**, pp.745-761.

Grim, R., 1953. Clay Mineralogy. New York: McGraw-Hill.

Gbadamosi, A., Junin, R., Manan, M., Agi, A. and Yusuf, A., 2019. An overview of chemical enhanced oil recovery: recent advances and prospects. *International Nano Letters*, **9**, pp.171–202.

Han, T., Hong, Y., Xie, N., Chen, S., Zhao, N., Zhao, E., Lam, J., Sung, H., Dong, Y., Tong, B. and Tang, B., 2013. Defect-sensitive crystals based on diaminomaleonitrile-functionalized Schiff base with aggregation-enhanced emission. *Journal of Materials Chemistry C*, **1**, p.7314-7320.

Hassenkam, T., Mitchell, A., Pedersen, C., Skovbjerg, L., Bovet, N. and Stipp, S., 2012. The low salinity effect observed on sandstone model surfaces. Colloids and Surfaces A: *Physicochemical and Engineering Aspects*, **403**, pp.79-86.

Hassenkam, T., Pedersen, C., Dalby, K., Austad, T. and Stipp, S., 2011. Pore scale observation of low salinity effects on outcrop and oil reservoir sandstone. Colloids and Surfaces A: *Physicochemical and Engineering Aspects*, **390**, pp.179-188.

Hilner, E., Andersson, M., Hassenkam, T., Matthiesen, J., Salino, P. and Stipp, S. (2015). The effect of ionic strength on oil adhesion in sandstone – the search for the low salinity mechanism. *Scientific Reports*, **5**, pp.1-12.

Honarvar, B., Rahimi, A., Safari, M., Rezaee, S. and Karimi, M., 2020. Favorable attributes of low salinity water aided alkaline on crude oil-brine-carbonate rock system. Colloids and Surfaces A: *Physicochemical and Engineering Aspects*, **585**, pp.1-12.

Huggett, J., 2015. Clay Minerals. Elsevier Inc, pp.1-8.

Horwath, W. and Liang, Y., 2011. Variations of Chemical Composition and Band Gap Energies in Hectorite and Montmorillonite Clay Minerals on Sub-Micron Length Scales. [online] Available at: <http://kearney.ucdavis.edu/NEW%20MISSION-LIVE/2009FINALReports/2009_008_Horwath_FINAL-rad.pdf> [Accessed 23 February 2021].

Hosmane, N., 2007. Advanced Inorganic Chemistry Chapter 1 - Electronic Structure: Quantum Theory Revisited. *Academic Press*, pp.3-13.

Huhtamäki, T., Tian, X., Korhonen, J. and Ras, R., 2018. Surface-wetting characterization using contact-angle measurements. *Nature Protocols*, **13**, pp.1521-1538.

Hui, S., 2020. Welcome To Stephen Hui Geological Museum. [online] Earthsciences.hku.hk. Available at: <https://www.earthsciences.hku.hk/shmuseum/earth_mat_1_2_6.php> [Accessed 18 September 2020].

Hurt, R. (2016). Electron emission mechanisms.svg. [online] En.wikipedia.org. Available at: https://en.wikipedia.org/wiki/File:Electron_emission_mechanisms.svg [Accessed 12 Nov. 2019].

Ibrahim, I., Lenčéš, Z., Šajgalík, P., Benco, L. and Marsman, M., 2015. Electronic structure and energy level schemes of RE3+:LaSi3N5 and RE2+:LaSi3N5−xOx phosphors (RE=Ce, Pr, ND, Pm, Sm, Eu) from first principles. Journal of Luminescence, 164, pp.131-137.

Iino, R., 2012. 全反射照明蛍光顕微鏡 [Total Internal Reflection Fluorescence

Microscopy]. [online] Available at: <https://groups.ims.ac.jp/organization/iino_g/pdf/2012TIRFM_IINO.pdf> [Accessed 23 November 2020].

Ito, A. and Wagai, R., 2017. Global distribution of clay-size minerals on land surface for biogeochemical and climatological studies. *Scientific Data*, **4**, pp.1-11.

Ito, M., Okamoto, M., Suzuki, K., Shibata, M. and Sasaki, Y., 1994. Mineral Composition Analysis of Bentonite. *Journal- Atomic Energy Society of Japan*, **36**, pp.1055-1058.

Jackson, M., Vinogradov, J., Hamon, G. and Chamerois, M., 2016. Evidence, mechanisms and improved understanding of controlled salinity waterflooding part 1: Sandstones. *Fuel*, **185**, pp.772-793.

Kakati, A., Kumar, G. and Sangwai, J., 2020. Oil Recovery Efficiency and Mechanism of Low Salinity-Enhanced Oil Recovery for Light Crude Oil with a Low Acid Number. *ACS Omega*, 5, pp.1506-1518.

Kareem, R. 2016. Nano geochemistry of Low Salinity Enhanced Oil Recovery. *Department of Earth Science, Durham University, United Kingdom*, pp.1-376.

Kargarpour, M., 2016. Investigation of reservoir temperature in a gas reservoir in Middle East: case study. *Journal of Petroleum Exploration and Production Technology*, **7**, pp.531-541.

Katende, A. and Sagala, F., 2019. A critical review of low salinity water flooding: Mechanism, laboratory and field application. *Journal of Molecular Liquids*, **278**, pp.627-649.

King, H., 2020. Fluorescent Minerals And Rocks: They Glow Under UV Light!. [online] Geology.com. Available at: <https://geology.com/articles/fluorescent-minerals/> [Accessed 27 August 2020].

Kogel, J., Trivedi, N., Barker, J. and Krukowski, S., 2006. Industrial Minerals & Rocks: Commodities, Markets, and Uses. 7th ed. *Society for Mining, Metallurgy and Exploration Inc*., p.384.

Kristian, M., 2013. File:Afmsetup.Jpg - Wikimedia Commons. [online] Commons.wikimedia.org. Available at: <https://commons.wikimedia.org/wiki/File:AFMsetup.jpg> [Accessed 23 July 2020].

Lancashire, R., 2020. Crystal Field Theory. [online] Chemistry LibreTexts. Available at: <https://chem.libretexts.org/Bookshelves/Inorganic_Chemistry/Modules_and_Websites_(Inorganic_Chemistry)/Crystal_Field_Theory/Crystal_Field_Theory> [Accessed 18 February 2021].

Landis, E. and Keane, D., 2010. X-ray Microtomography. *Materials Characterization*, **61**, pp.1305-1316.

Lange, D., Jennings, H. and Shah, S., 1993. Analysis of surface roughness using confocal microscopy. *Journal of Materials Science*, **28**, pp.3879-3884.

Lager, A., Webb, K. and Black, C., 2007. Impact of Brine Chemistry on Oil Recovery. European Association of Geoscientists & Engineers,.

Lager, A., Webb, K., Black, C., Singleton, M. and Sorbie, K., 2008. Low Salinity Oil Recovery - An Experimental Investigation1. *Society of Petrophysicists and Well-Log Analysts*, **49**, pp.28-35.

Law, K., 2014. Definitions for Hydrophilicity, Hydrophobicity, and Superhydrophobicity: Getting the Basics Right. *The Journal of Physical Chemistry Letters*, **5**, pp.686-688.

Ligthelm, D., Gronsveld, J., Hofman, J., Brussee, N., Marcelis, F. and Linde, H., 2009. Novel Waterflooding Strategy by Manipulation of Injection Brine Composition. *Society of Petroleum Engineers*, pp.1-22.

Li, X., Li, F., Yang, C. and Ge, W., 2001. Photocatalytic activity of WOx-TiO2 under visible light irradiation. *Journal of Photochemistry and Photobiology A: Chemistry*, *141*, pp.209-217.

Lovering, T. and Goode, H., 1963. Measuring Geothermal Gradients In Drill Holes Less Than 60 Feet Deep. Washington: U.S. Govt. Print. Off.

Ma, A., 2016. Kinetics of oil-cracking for different types of marine oils from Tahe Oilfield, Tarim Basin, NW China. *Journal of Natural Gas Geoscience*, **1**, pp.35-43.

Mahani, H., Berg, S., Ilic, D., Bartels, W. and Joekar-Niasar, V., 2015. Kinetics of Low-Salinity-Flooding Effect. *Society of Petroleum Engineers*, **20**, pp.008-020.

Mahani, H., Keya, A., Berg, S. and Nasralla, R., 2017. Electrokinetics of Carbonate/Brine Interface in Low-Salinity Waterflooding: Effect of Brine Salinity, Composition, Rock Type, and pH on ζ-Potential and a Surface-Complexation Model. *Society of Petroleum Engineers*, **22**, pp.053-068.

Martin, J., 1959. The Effects of Clay on the Displacement of Heavy Oil by Water. *Society of Petroleum Engineers*, pp.1-23.

Marshak, S., 2007. Earth: Portrait of a Planet. 3rd ed. W. W. Norton & Company.

Maskari, N., Sari, A., Hossain, M., Saeedi, A. and Xie, Q., 2019. Response of Non-Polar Oil Component on Low Salinity Effect in Carbonate Reservoirs: Adhesion Force Measurement Using Atomic Force Microscopy. *Energies*, **13**, p.77.

Matthiesen, J., Bovet, N., Hilner, E., Andersson, M., Schmidt, D., Webb, K., Dalby, K., Hassenkam, T., Crouch, J., Collins, I. and Stipp, S., 2014. How Naturally Adsorbed Material on Minerals Affects Low Salinity Enhanced Oil Recovery. *Energy & Fuels*, **28**, pp.4849-4858.

McGuire, P., Chatham, J., Paskvan, F., Sommer, D. and Carini, F., 2005. Low Salinity Oil Recovery: An Exciting New EOR Opportunity for Alaska's North Slope. Society of Petroleum Engineers, pp.1-15.

Millemann, R., Haynes, R., Boggs, T. and Hildebrand, S. (1982). Enhanced oil recovery: Environmental issues and state regulatory programs. *Environment International*, **7**, pp.165-177.

Mjaavatten, A., Aasheim, R., Saelid, S. and Groenning, O., 2008. A Model for Gas Coning and Rate-Dependent Gas/Oil Ratio in an Oil-Rim Resevoir. *SPE Reservoir Evaluation & Engineering*, **11**, pp.842-847.

Mousavi Moghadam, A. and Baghban Salehi, M., 2019. Enhancing hydrocarbon productivity via wettability alteration: a review on the application of nanoparticles. *Reviews in Chemical Engineering*, **35**, pp.531-563.

Mokhtari, R. and Ayatollahi, S., 2018. Dissociation of polar oil components in low salinity water and its impact on crude oil–brine interfacial interactions and physical properties. *Petroleum Science*, **16**, pp.328-343.

Morishita, R., Matsuyama, R., Ishiwata, T., Tsuchiya, Y., Giang, P. and Takahashi, S., 2020. Oil and Water Interactions during Low-Salinity Enhanced Oil Recovery in Water-Wet Porous Media. *Energy & Fuels*, **34**, pp.5258-5266.

Moses, A., 1968. Analytical Chemistry Of The Actinide Elements. Oxford, New York: Pergamon Press.

Moghadam, A. and Baghban Salehi, M., 2019. Enhancing hydrocarbon productivity via wettability alteration: a review on the application of nanoparticles. *Reviews in Chemical Engineering*, **35**, pp.531-563.

Mugele, F., Bera, B., Cavalli, A., Siretanu, I., Maestro, A., Duits, M., Cohen-Stuart, M., van den Ende, D., Stocker, I. and Collins, I., 2015. Ion adsorption-induced wetting transition in oil-water-mineral systems. *Scientific Reports*, **5**, pp.1-8.

M-Dish 35 Mm, High Glass Bottom | High Quality Imaging | Ibidi., 2020 [online] Available at: <https://ibidi.com/dishes/176--dish-35-mm-high-glass-bottom.html> [Accessed 30 July 2020].

Nair, S., Gao, J., Otto, C., Duits, M. and Mugele, F., 2020. In-situ observation of reactive wettability alteration using algorithm-improved confocal Raman microscopy. *Journal of Colloid and Interface Science*, **584**, pp.551-560.

Nasralla, R. and Nasr-El-Din, H., 2014. Double-Layer Expansion: Is It a Primary Mechanism of Improved Oil Recovery by Low-Salinity Waterflooding?. *SPE Reservoir Evaluation & Engineering*, **17**, pp.49-59.

Nassau, K., 2021. Energy bands. [online] Encyclopedia Britannica. Available at: <https://www.britannica.com/science/color/The-perception-of-colour> [Accessed 17 February 2021].

Nguyen, N., Dang, C., Gorucu, S., Nghiem, L. and Chen, Z., 2020. The role of fines transport in low salinity waterflooding and hybrid recovery processes. Fuel, 263, pp.1-12.

Nguyen, P., Fadaei, H. and Sinton, D. (2014). Pore-Scale Assessment of Nanoparticle-Stabilized CO2 Foam for Enhanced Oil Recovery. *Energy & Fuels*, **28**, pp.6221-6227.

Noy, A., Vezenov, D. and Lieber, C., 1997. Chemical Force Microscopy. *Annual Review of Materials Science*, **27**, pp.381-421.

Ockenga, W., 2012. Total Internal Reflection Fluorescence (TIRF) Microscopy. [online] Available at: <https://www.leica-microsystems.com/science-lab/total-internal-reflection-fluorescence-tirf-microscopy/> [Accessed 23 November 2020].

Oxy.com. 2020. Enhanced Oil Recovery. [online] Available at: <https://www.oxy.com/OurBusinesses/OilandGas/Technology/Pages/Enhanced-Oil-Recovery.aspx#:~:text=CO2%20EOR%20benefits%20the,reduces%20land%20and%20habitat%20disturbance.> [Accessed 19 October 2020].

Patel, K., Shah, M. and Sircar, A. (2018). Plasma Pulse Technology: An uprising EOR technique. *Petroleum Research*, **3**, pp.180-188.

Pawley, J., 2010. Handbook Of Biological Confocal Microscopy. New York, NY: Springer.

Pershad, H, Durusut, E, Alan, C, Black, D, Mackay, EJ & Olden, P 2012, Economic Impacts of CO2-Enhanced Oil Recovery for Scotland: Final report. *Scottish Enterprise*, Glasgow.

Pierce, M., Stuart, J., Pungor, A., Dryden, P. and Hlady, V., 1994. Adhesion Force Measurements Using an Atomic Force Microscope Upgraded with a Linear Position Sensitive Detector. *Langmuir*, **10**, pp.3217-3221.

Pietzsch, A., Nisar, J., Jämstorp, E., Gråsjö, J., Århammar, C., Ahuja, R. and Rubensson, J., 2015. Kaolinite: Defect defined material properties – A soft X-ray and first principles study of the band gap. *Journal of Electron Spectroscopy and Related Phenomena*, **202**, pp.11-15.

Pinerez T, I., Austad, T., Strand, S., Puntervold, T. and Wrobel, S., 2016. Linking Low Salinity EOR Effects in Sandstone to pH, Mineral Properties and Water Composition. Society of Petroleum Engineers, pp.1-17.

Pouryousefy, E., Xie, Q. and Saeedi, A., 2016. Effect of multi-component ions exchange on low salinity EOR: Coupled geochemical simulation study. *Petroleum*, **2**, pp.215-224.

Pu, H., Xie, X., Yin, P. and Morrow, N., 2010. Low-Salinity Waterflooding and Mineral Dissolution. *Society of Petroleum Engineers*, pp.1-17.

Quigley, T. and Mackenzie, A., 1988. The temperatures of oil and gas formation in the sub-

surface. *Nature*, **333**, pp.549-552.Renpu, W., 2011. Advanced Well Completion Engineering, Third Edition. 3rd ed. Waltham, Mass.: Gulf Professional Pub.

Rezaeidoust, A., Puntervold, T. and Austad, T., 2010. A Discussion of the Low-Salinity EOR Potential for a North Sea Sandstone Field. *Society of Petroleum Engineers*, pp.1-12.

Robbana, E., Buikema, T., Mair, C., Williams, D., Mercer, D., Webb, K., Hewson, A. and Reddick, C., 2012. Low Salinity Enhanced Oil Recovery - Laboratory to Day One Field Implementation - LoSal EOR into the Clair Ridge Project. *Society of Petroleum Engineers*, pp.1-15.

Ross, S., Schwartz, S., Fellers, T. and Davidson, M., n.d. Total Internal Reflection Fluorescence (TIRF) Microscopy.[online] Available at: <https://www.microscopyu.com/techniques/fluorescence/total-internal-reflection-fluorescence-tirf-microscopy> [Accessed 23 November 2020].

Rost, F., 1995. Fluorescence Microscopy. Cambridge: Cambridge University Press.

Rugar, D. and Hansma, P., 1990. Atomic Force Microscopy. [ebook] American Institution of Physics, pp.23-30. Available at: <https://www.if.ufrj.br/~tclp/estadosolido/phystoday23(90).pdf> [Accessed 31 December 2020].

Russell, P., Batchelor, D. and Thornton, J., 2001. SEM and AFM: Complementary Techniques for High Resolution Surface Investigations. *Veeco Instruments, Inc*, pp.1-11.

Ryder, A., 2005. Analysis of Crude Petroleum Oils Using Fluorescence Spectroscopy. *Reviews in Fluorescence*, pp.169-198.

Samanta, A., Ojha, K. and Mandal, A., 2011. Interactions between Acidic Crude Oil and Alkali and Their Effects on Enhanced Oil Recovery. *Energy & Fuels*, **25**, pp.1642-1649.

Sarkar, A. and Sharma, M., 1990. Fines Migration in Two-Phase Flow. *Journal of Petroleum Technology*, **42**, pp.646-652.

Santha, N., Cubillas, P., Collins, I., Carteret, C. and Greenwell, H., n.d. Adsorption of oil compounds on kaolinite and pyrophyllite as studied by thermal gravimetric analysis – mass spectrometry (TGA-MS). pp.1-26.

Santha, N., Cubillas, P. and Greenwell, C., 2019. The Effect of Salinity and pH on Wettability Alteration of Kaolinite Films Studied by Contact Angle Measurement. *European Association of Geoscientists & Engineers*, **2019**, pp.1-17.

Santha, N., 2019. Understanding Clay-Oil-Brine Interactions at the Nano-scale: Implications for Low-Salinity Enhanced Oil Recovery. Department of Earth Science, Durham University, United Kingdom, pp.1-255.

Schneider, S., 2011. Collecting Fluorescent Minerals. 2nd ed. Schiffer.

Seccombe, J., Lager, A., Jerauld, G., Jhaveri, B., Buikema, T., Bassler, S., Denis, J., Webb,

K., Cockin, A., Fueg, E. and Paskvan, F., 2020. Demonstration of Low-Salinity EOR at Interwell Scale, Endicott Field, Alaska. *Society of Petroleum Engineers*, pp.1-12.

Semwogerere, D. and Weeks, E., 2005. Confocal Microscopy. [ebook] Emory University, Atlanta, Georgia, U.S.A: *Semantic Scholar*, pp.1-10.Available at:<http://www.physics.emory.edu/faculty/weeks//lab/papers/ebbe05.pdf> [Accessed 31 December 2020].

Shabaninejad, M., Middlelton, J. and Fogden, A., 2018. Systematic pore-scale study of low salinity recovery from Berea sandstone analyzed by micro-CT. *Journal of Petroleum Science and Engineering*, **163**, pp.283-294.

Shariatpanahi, S., Strand, S. and Austad, T., 2010. Evaluation of Water-Based Enhanced Oil Recovery (EOR) by Wettability Alteration in a Low-Permeable Fractured Limestone Oil Reservoir. *Energy & Fuels*, **24**, pp.5997-6008.

Sharma, M. and Filoco, P., 2000. Effect of Brine Salinity and Crude-Oil Properties on Oil Recovery and Residual Saturations. *Society of Petroleum Engineers*, **5**, pp.293-300.

Shen, C., 2002. Limitations and Potentials of In-Situ Combustion Processes for Heavy Oil Reservoirs. *Petroleum Society of Canada*, pp.1-14.

Shende, S., Pendharker, S., Jacob, Z. and Nazemifard, N. (2016). Total Internal Reflection Fluorescence Microscopy To Investigate the Distribution of Residual Bitumen in Oil Sands Tailings. *Energy & Fuels*, **30**, pp.5537-5546.

Siretanu, I., Ebeling, D., Andersson, M., Stipp, S., Philipse, A., Stuart, M., van den Ende, D. and Mugele, F., 2014. Direct observation of ionic structure at solid-liquid interfaces: a deep look into the Stern Layer. *Scientific Reports*, **4**, pp.1-7.

Song, W. and Kovscek, A., 2016. Direct visualization of pore-scale fines migration and formation damage during low-salinity waterflooding. *Journal of Natural Gas Science and Engineering*, **34**, pp.1276-1283.

Souto, E. and Bazin, B., 1993. Ion Exchange Between Hydrogen and Homoionic Brines Related to Permeability Reduction. *Society of Petroleum Engineers*, pp.491-500.

Sposito, G., 2004. The Surface Chemistry Of Natural Particles. Cary, NC, USA: Oxford University Press.

Stosur, G., Hite, J., Carnahan, N. and Miller, K., 2003. IOR and EOR: Effective Communication Requires a Definition of Terms. *Journal of Petroleum Technology*, **55**, pp.16-16.

Takeya, M., Shimokawara, M., Elakneswaran, Y., Nawa, T. and Takahashi, S., 2019. Predicting the electrokinetic properties of the crude oil/brine interface for enhanced oil recovery in low salinity water flooding. *Fuel*, **235**, pp.822-831.

Tang, G. and Morrow, N., 1999a. Influence of brine composition and fines migration on

crude oil/brine/rock interactions and oil recovery. *Journal of Petroleum Science and Engineering*, **24**, pp.99-111.

Tang, G. and Morrow, N., 1999b. Oil Recovery by Waterflooding and Imbibition - Invading Brine Cation Valency and Salinity. *Society of Core Analysts*, pp.1-12.

Tertiary recovery - Schlumberger Oilfield Glossary. [online] Available at: <https://glossary.oilfield.slb.com/en/Terms/t/tertiary_recovery.aspx> [Accessed 10 February 2021].

Thermofisher.com. (2019). Physical Properties That Define Fluorescence | Thermo Fisher Scientific - UK. [online] Available at: https://www.thermofisher.com/uk/en/home/life-science/cell-analysis/cell-analysis-learning-center/molecular-probes-school-of-fluorescence/imaging-basics/fundamentals-of-fluorescence-microscopy/physical-properties-that-define-fluorescence.html [Accessed 6 Nov. 2019].

Thomas, S. (2007). Enhanced Oil Recovery - An Overview. Oil & Gas Science and Technology - *Revue de l'IFP*, **63**, pp.9-19.

TIE-36: Fluorescence Of Optical Glass. [ebook] Schott Glass Made of Ideas, pp.1-12. Available at: <https://www.schott.com/d/advanced_optics/18bb0d12-b7d7-4af9-b25d-f0cdae363a2c/1.0/schott-tie-36-fluorescence-of-optical-glass-august-2010-english.pdf> [Accessed 31 December 2020].

Tisler, J., Balasubramanian, G., Naydenov, B., Kolesov, R., Grotz, B., Reuter, R., Boudou, J., Curmi, P., Sennour, M., Thorel, A., Börsch, M., Aulenbacher, K., Erdmann, R., Hemmer, P., Jelezko, F. and Wrachtrup, J., 2009. Fluorescence and Spin Properties of Defects in Single Digit Nanodiamonds. *ACS Nano*, **3**, pp.1959-1965.

Ultrawave Precision Ultrasonic Cleaning Equipment, 2004. Instruction Manual For Bench-Top Cleaning Baths. [online] 1 Oxford Street, Cardiff, CF24 3WY United Kingdom, p.3. Available at: <http://www.frankshospitalworkshop.com/equipment/documents/surgical_instruments/user_manuals/US_cleaner/Ultrawave%20Cleaning%20Bath%20-%20User%20manual.pdf> [Accessed 4 August 2020].

USGS, 2020. Saline Water And Salinity. [online] USGS Science for a changing world. Available at: <https://www.usgs.gov/special-topic/water-science-school/science/saline-water-and-salinity?qt-science_center_objects=0#qt-science_center_objects> [Accessed 25 June 2020].

Valdya, R. and Fogler, H., 1992. Fines Migration and Formation Damage: Influence of pH and Ion Exchange. *Society of Petroleum Engineers*, **7**, pp.325-330.

WAG Schlumberger Oilfield Glossary. [online] Available at: https://www.glossary.oilfield.slb.com/en/Terms/w/wag.aspx [Accessed 9 Nov. 2019].

Wang, H., Zhao, E., Lam, J. and Tang, B., 2015. AIE luminogens: emission brightened by

aggregation. *Materials Today*, **18**, pp.365-377.

Warwick, T., 2017. Micro-CT in Geology and Geoscience. [online] Available at: <https://www.blue-scientific.com/micro-ct-in-geology-and-geoscience/> [Accessed 5 November 2020].

Webb, K., Black, C. and Edmonds, I., 2005a. Low Salinity Oil Recovery – The Role of Reservoir Condition Corefloods. European Association of Geoscientists & Engineers,.

Webb, K., Black, C. and Tjetland, G., 2005. A Laboratory Study Investigating Methods for Improving Oil Recovery in Carbonates. *International Petroleum Technology Conference*, pp.1-7.

Wei, B., Lu, L., Li, Q., Li, H. and Ning, X., 2017. Mechanistic Study of Oil/Brine/Solid Interfacial Behaviors during Low-Salinity Waterflooding Using Visual and Quantitative Methods. *Energy & Fuels*, **31,** pp.6615-6624.

Winoto, W., Loahardjo, N., Xie, X., Yin, P. and Morrow, N., 2012. Secondary and Tertiary Recovery of Crude Oil from Outcrop and Reservoir Rocks by Low Salinity Waterflooding. *Society of Petroleum Engineers*, pp.1-13.

Xie, Q., Saeedi, A., Pooryousefy, E. and Liu, Y., 2016. Extended DLVO-based estimates of surface force in low salinity water flooding. *Journal of Molecular Liquids*, **221**, pp.658-665.

Yang, G., Chen, T., Zhao, J., Yu, D., Liu, F., Wang, D., Fan, M., Chen, W., Zhang, J., Yang, H. and Wang, J., 2015. Desorption Mechanism of Asphaltenes in the Presence of Electrolyte and the Extended Derjaguin–Landau–Verwey–Overbeek Theory. *Energy & Fuels*, **29**, pp.4272-4280.

Yousef, A., Al-Saleh, S., Al-Kaabi, A. and Al-Jawfi, M., 2011. Laboratory Investigation of the Impact of Injection-Water Salinity and Ionic Content on Oil Recovery From Carbonate Reservoirs. *SPE Reservoir Evaluation & Engineering*, **14**, pp.578-593.

Yu, M., Hussain, F., Arns, J., Bedrikovetsky, P., Genolet, L., Behr, A., Kowollik, P. and Arns, C., 2018. Imaging analysis of fines migration during water flow with salinity alteration. *Advances in Water Resources*, **121**, pp.150-161.

ZEISS LSM 800 With Airyscan Your Compact Confocal Power Pack., 2015. [online] Available at: <https://www.unige.ch/medecine/bioimaging/files/4914/2771/7087/LSM_800_Confocal_Power_Pack.pdf> [Accessed 8 May 2020].

Zerkalov, G., 2015. Steam Injection For Enhanced Oil Recovery. [ebook] Stanford University. Available at: <http://large.stanford.edu/courses/2015/ph240/zerkalov2/> [Accessed 30 December 2020].

Zhang, Y. and Morrow, N., 2006. Comparison of Secondary and Tertiary Recovery With Change in Injection Brine Composition for Crude-Oil/Sandstone Combinations. *Society of*

Petroleum Engineers, pp.1-14.

Zhang, Y., Xie, X. and Morrow, N., 2007. Waterflood Performance By Injection Of Brine With Different Salinity For Reservoir Cores. *Society of Petroleum Engineers*, pp.1-12.

Appendix

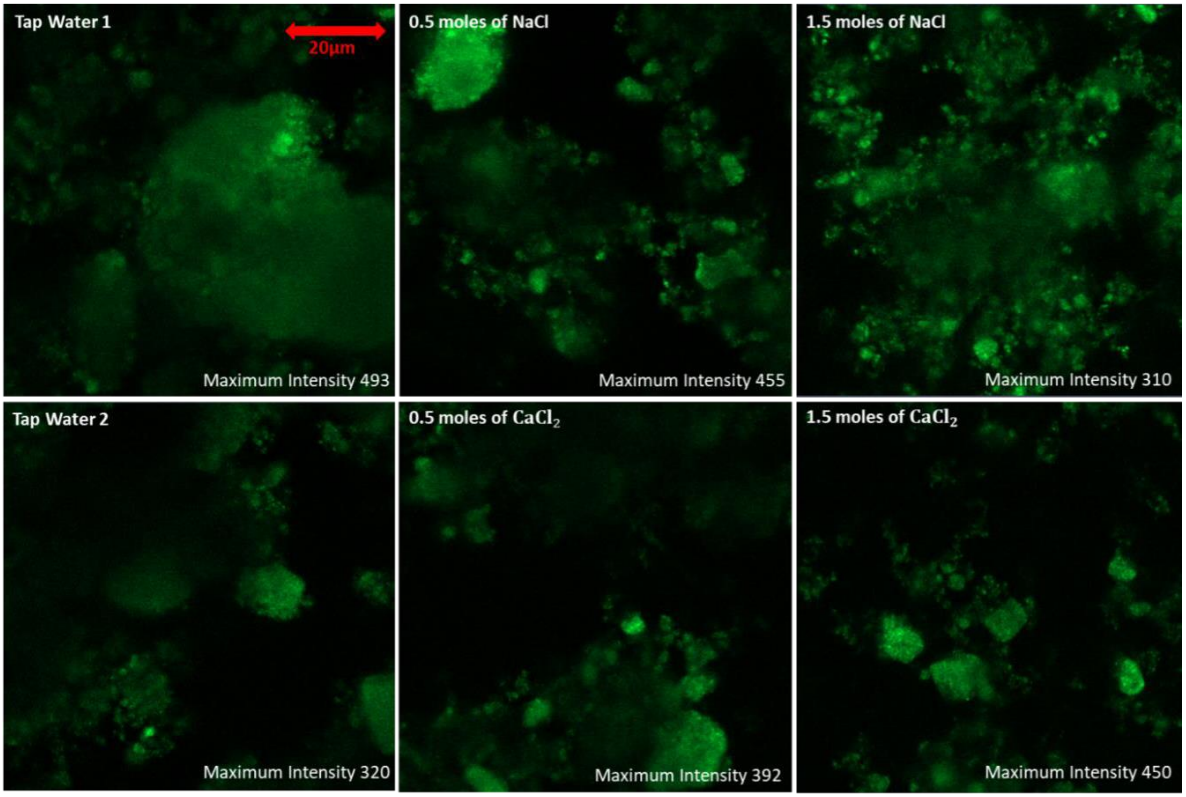

Appendix 1: Exhibiting fluorescence of Kaolin with different salinity levels of brines. The maximum intensity each image are fit in the range of 300 and 500; these images are also show that difference in salinity levels does not make noticeable changes in terms of quality of images (fluorescence of clay minerals) and strength of maximum intensities.

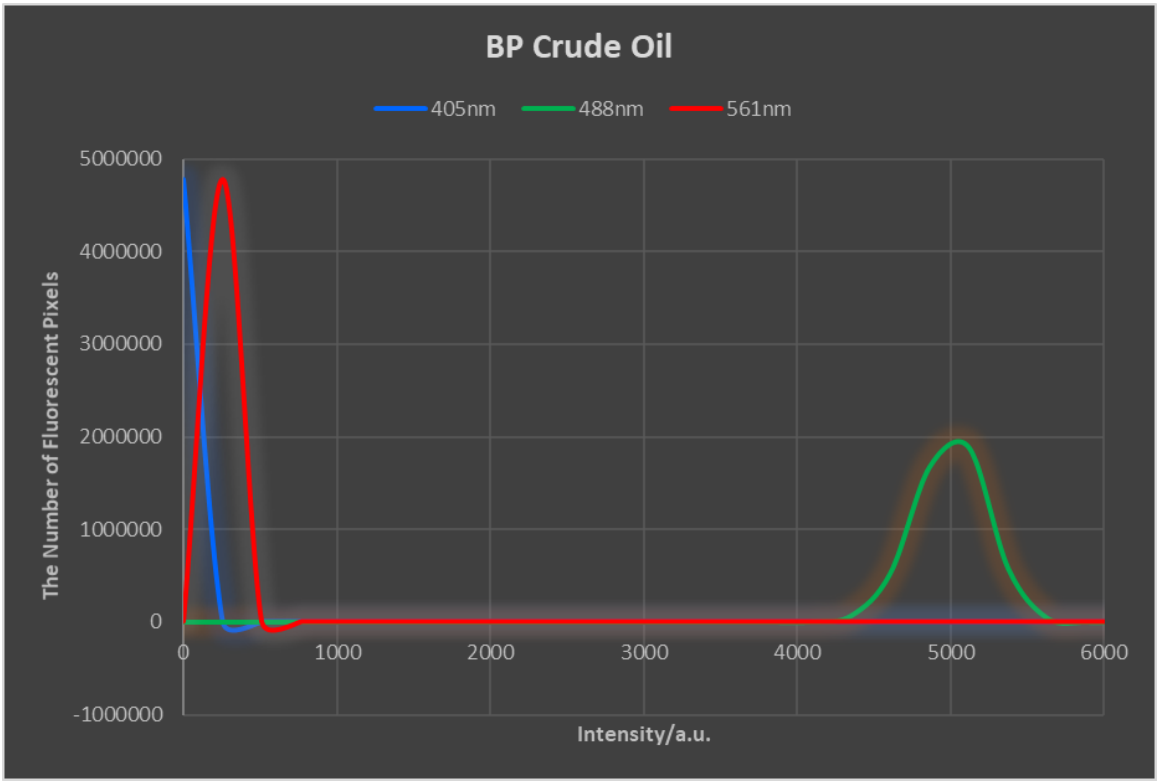

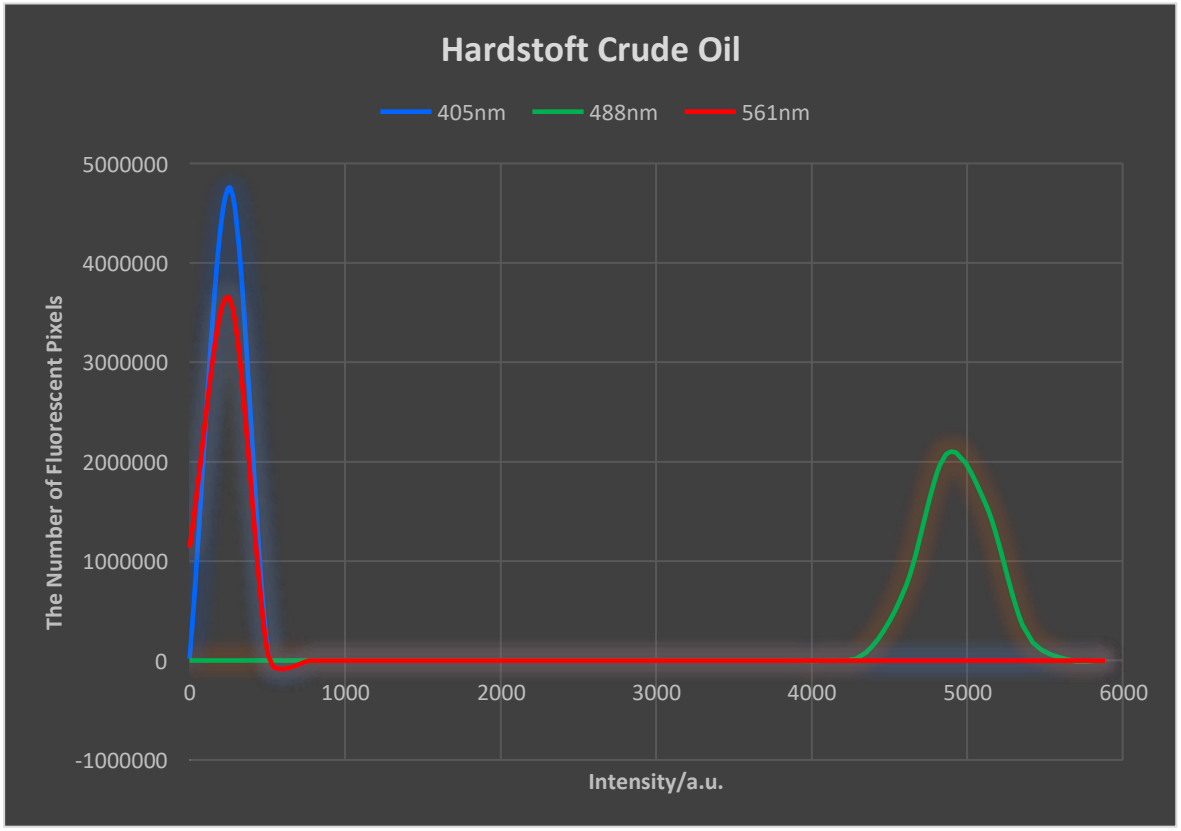

Appendix 2: For the purpose of finding the best fluorescent images, three different laser wavelengths were utilsed simultaneously: 405nm, 488nm, and 561nm. Both crude oil types are more sensitive to the 488nm laser wavelength. A similar test was conducted with clay samples with the result that the 488nm laser wavelength is the most effective for use in all the experiments for this project.

Model Polar Crude Oil	Sample 1	Sample 2	Sample 3
Maximum Intensity/ a.u.	100	131	136

Model Non-Polar Crude Oil	Sample 1	Sample 2	Sample 3
Maximum Intensity/ a.u.	201	107	112

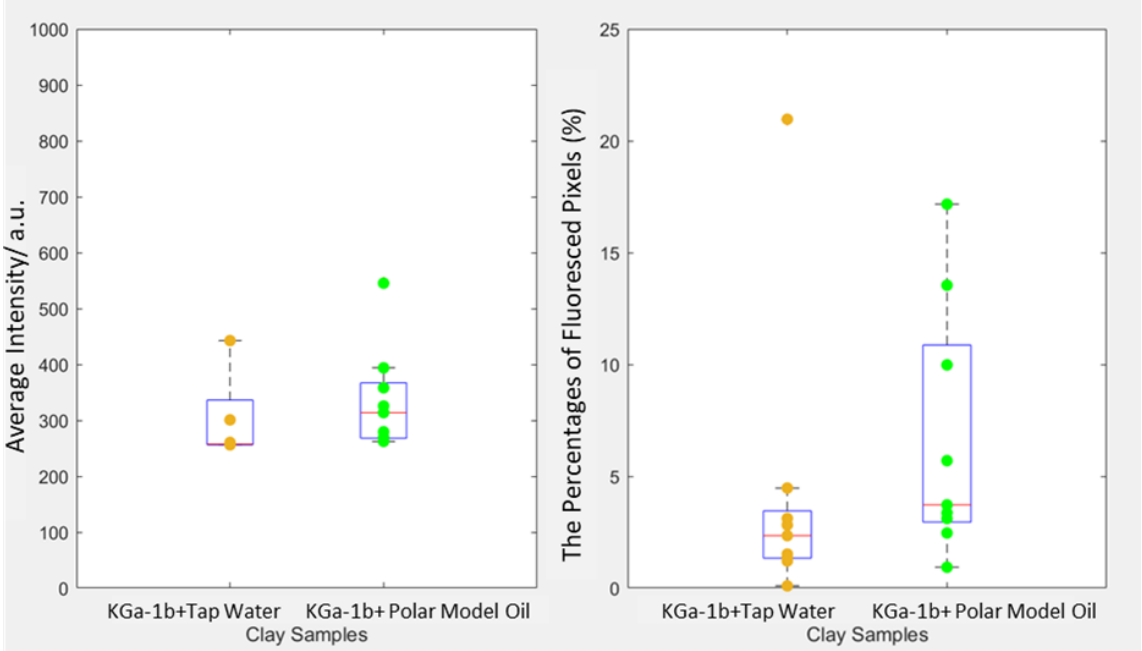

Appendix 3: [Table] The maximum intensity of polar model crude oil and non-polar model crude oil are shown in the tables; since most of the pixels in each fluorescent images did not fluoresce, compared their maximum intensity to manifest that even their fluorescent intensity is negligible. [Box plots] The left-hand side of the box plot shows approximate fluoresced intensity range based on tested nine images; each dots shows the average fluorescent intensity of each image. The right-hand-side of the box plot shows the fluoresced scope of each image. For the test of KGa-1b (Kalonite) with tap water and KGa-1b with polar model crude oil, the average intensity of two samples are comparatively homogeneous. Although KGa-1b with polar model oil showed broader fluoresced scope, it would be due to detecting of a more significant amount of clay minerals from the sample of KGa-1b +Polar model oil; this can be assumed from the results based upon the fluorescent intensity of model crude oil itself and average fluorescent intensity of KGa-1b with tap water and with polar model crude oil.

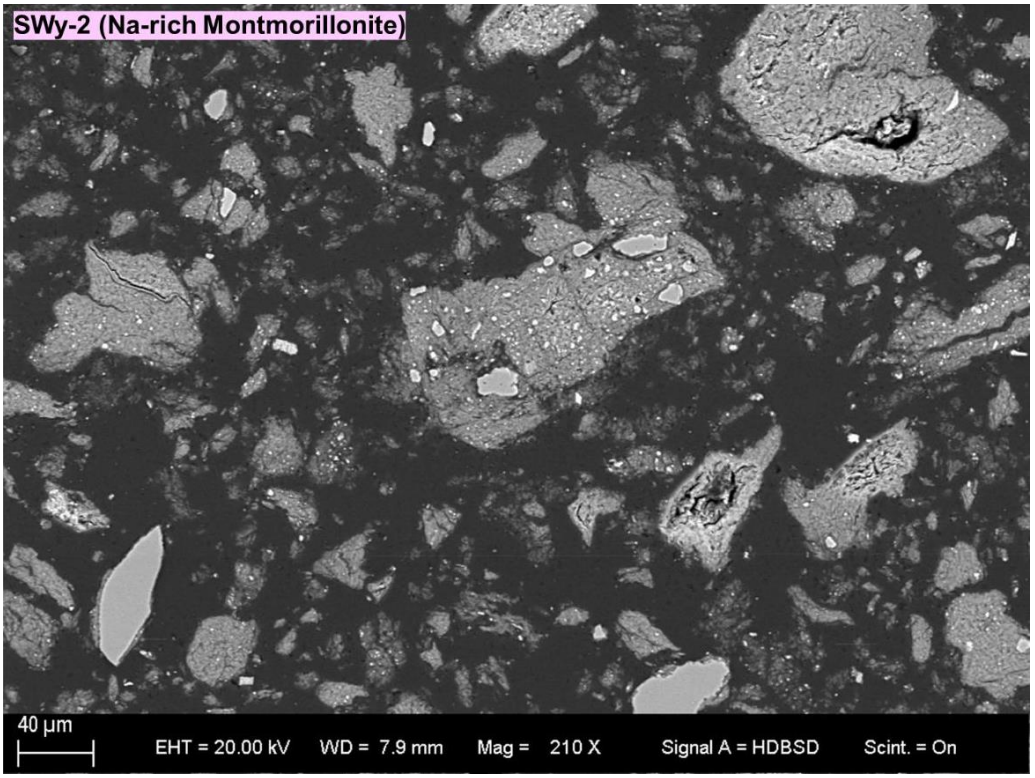

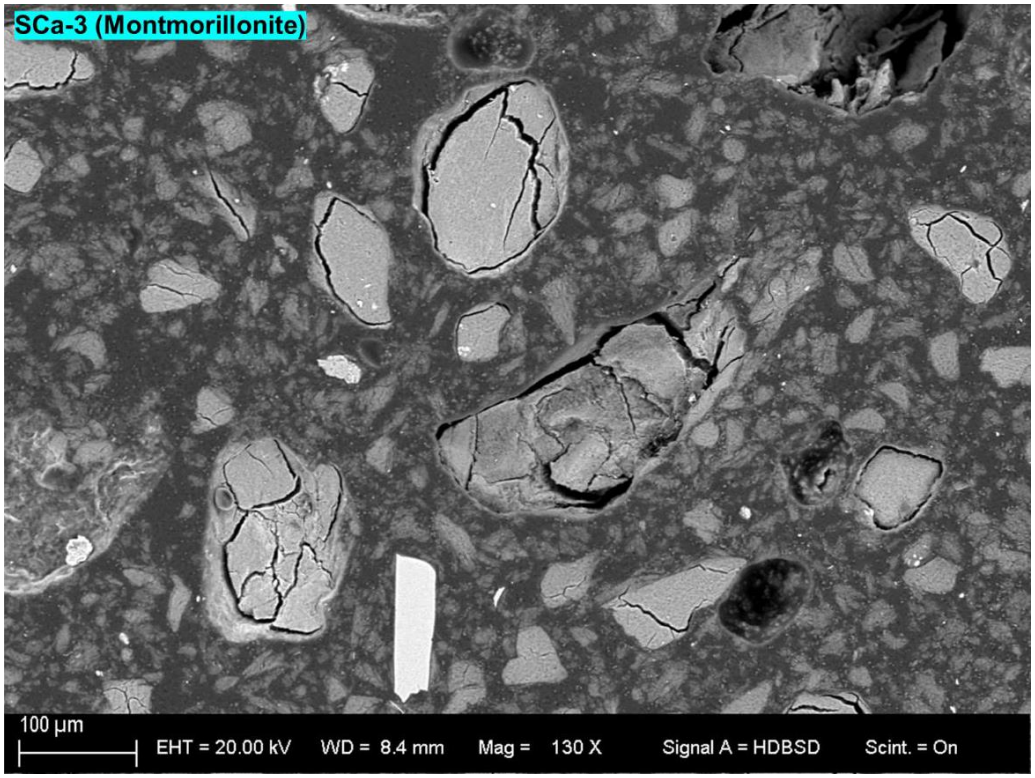
SCa-3 (Montmorillonite)
100 µm
EHT = 20.00 kV
WD = 8.4 mm
Mag = 130 X
Signal A = HDBSD
Scint. = On

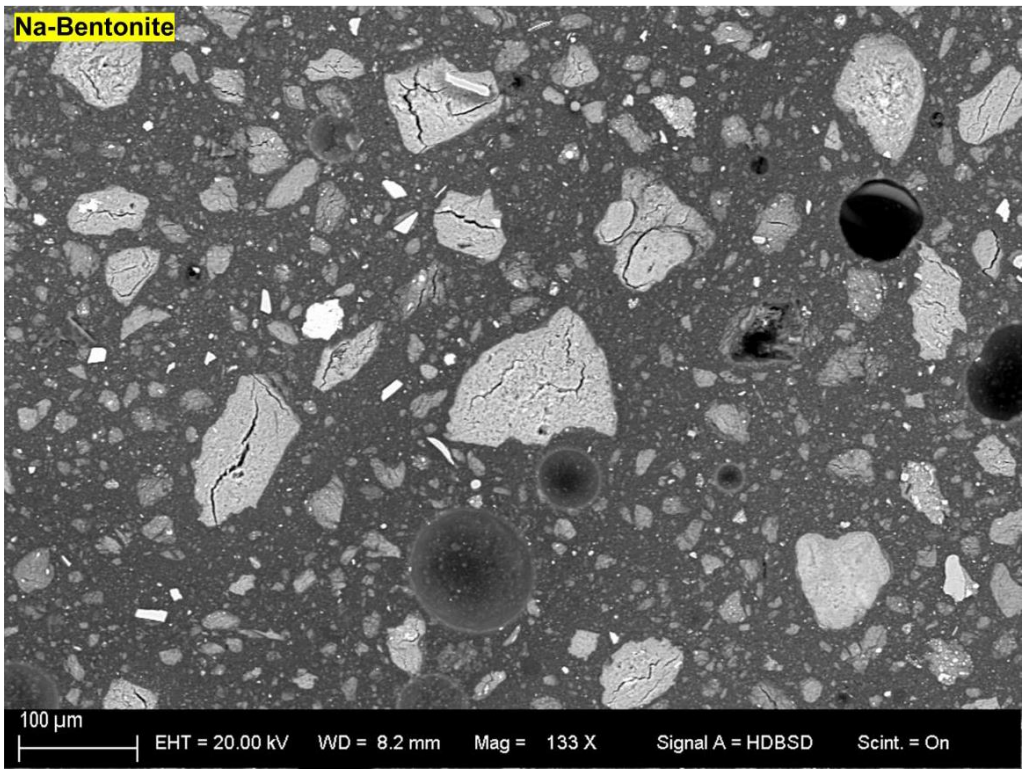
Na-Bentonite
100 µm
EHT = 20.00 kV
WD = 8.2 mm
Mag = 133 X
Signal A = HDBSD
Scint. = On

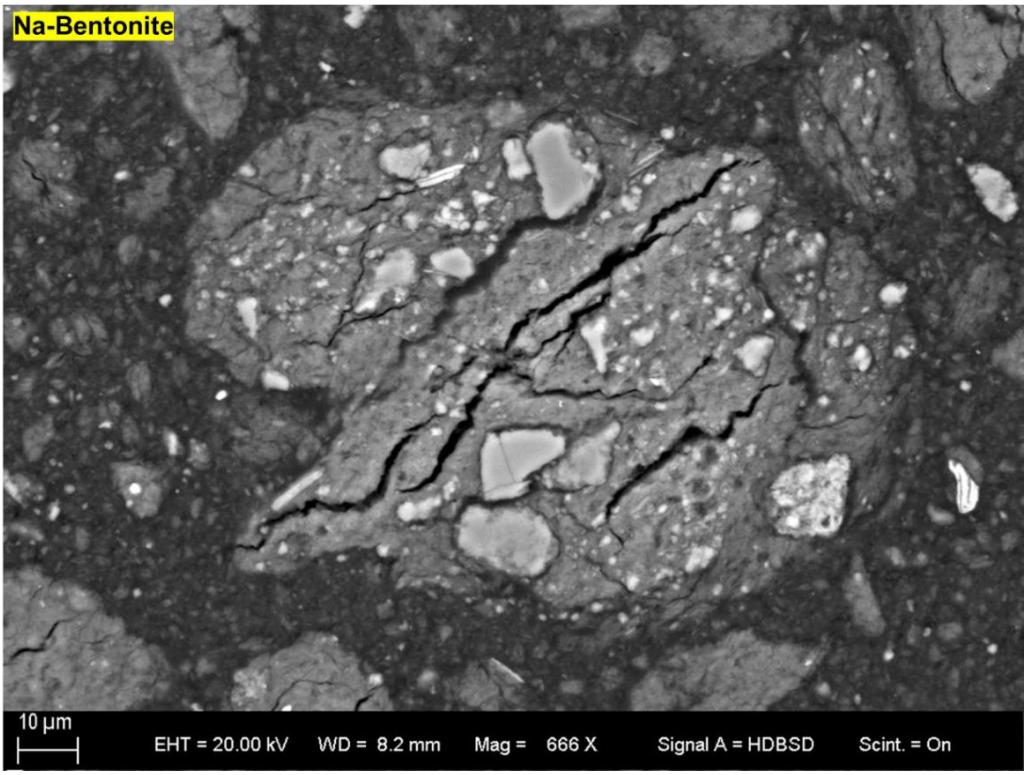

Appendix 4: The SEM images of SWy-2, SCa-3, and Na-Bentonite shows impurity; this is easy to identify by comparing to the scale bar which is located on the left, along the bottom. As the compassion implies, the size of mineral grains are more than 2µm. The size of clay particles is widely accepted as less than 2µm (Innocent, Fagel and Hillaire-Marcel, 2000; Soil properties, 2013; Tan *et al*., 2017).

Offical Names	Origin	Group	CEC (meq/100g)	SiO2 (%)	Al2O3	TiO2	Fe2O3	FeO	MnO	MgO	CaO	Na2O	K2O	F	P2O5	S	LOI	Total(%)	Distributor
Na-bentonite DGM	Wyoming, USA	2:1 Smectite Group	No Data	-	-	-	-	-	-	-	-	-	-	-	-				Steetley Na-bentonite & Absorbents Ltd,
SWy-2	Wyoming, USA	2:1 Smectite Group	76.4 (principle exchange cations are Na and Ca)	62.9	19.6	0.09	3.35	0.32	0.006	3.05	1.68	1.53	0.53	0.111	0.049			93.216	The clay mienrals society
SCa-3	Otay San Diego Country, California, USA	2:1 Smectite Group	No Data	52.8	15.7	0.181	1.06	-	-	-	-	-	-	-	-			69.741	The clay mienrals society
Kga-1b	Washington Country,Georgia, USA	1:1 Kaolinite	20	44.2	39.7	1.39	0.13	0.08	0.002	0.03	n.d.	0.013	0.05	0.013	0.034			85.642	The clay mienrals society
STx-1	County of Gonzales, State of Texas, USA	2:1 Smectite Group	84.4	70.1	16	0.22	0.65	0.15	0.009	3.69	1.59	0.27	0.078	0.084	0.026	0.04		92.907	The clay mienrals society
IMt-2	Silver Hill, Montana, USA	2:1 Micas	No Data	49.3	24.25	0.55	7.32	0.55	0.03	2.56	0.43	0	7.83	-	0.08	-	8.02	100.92	The clay mienrals society
CCa-2	Flagstaff Hill, El Dorado County, California, USA	2:1 Chrolite	No Data	26.0	20	0.476	26.6	20.8	0.1	17.2	0.25	-	-	-	-	-	-	85.426	The clay mienrals society
Offical Names	Origin	Group	CEC (meq/100g)	SiO2 (%)	Al2O3	TiO2	Fe2O3	FeO	MnO	MgO	CaO	Na2O	K2O	F	P2O5	S	LOI	Total(%)	
KGa-1b	Washington Country,Georgia, USA	1:1 Kaolinite	20	44.2	39.7	1.39	0.13	0.08	0.002	0.03	n.d.	0.013	0.05	0.013	0.034			85.642	The clay mienrals society
KGa-2	Warren, State of Georgia, USA	1:1 Kaolinite	3.3	43.9	38.5	2.08	0.98	0.15	n.d	0.03	n.d	<0.005	0.065	-	0.045	0.02		85.77	The clay mienrals society

Appendix5: Clay minerals data provided from the clay minerals society (http://www.clays.org/sourceclays_data.html). According to Moses and Rost (Moses, 1963; Rost, 1995), [Red] Presence of the element might enhance fluorescence (Al), [Blue] Presence of the elements quenches fluorescence (Fe, Mn, and Mg), and [Purple] presence of the elements could both enhance and quench fluorescence (Ca). In general, quenches occur due to an excess amount of activators. The details of Na-Bentonite were not provided from the distributor, Steetley Na-bentonite & Absorbents Ltd.

Property	Kaolinite	Illite	Montmorillonite	Chlorite
Structure	1:1	2:1	2:1	2:1:1
Surface area (m^2/gm)	15-25	50-110	30-80	140
Surface charge	No charge	Negative	Negative	Positive
CEC (meq/100g)	3-15	10-40	80-150	10-40
Particle size (micron)	5-0.5	Large sheets to 0.5	2-0.1	5-0.1

Appendix 6: clay properties of most common clay minerals in sandstone reservoir. (Meunier,2005), (Kareem, 2016)

Reference

Innocent, C., Fagel, N. and Hillaire-Marcel, C., 2000. Sm–Nd isotope systematics in deep-sea sediments: clay-size versus coarser fractions. *Marine Geology*, **168**, pp.79-87.

Kareem, R., 2016. Nano geochemistry of Low Salinity Enhanced Oil Recovery. Department of Earth Science, Durham University, United Kingdom.

Meunier, A., 2005. Clay. Springer Science &Business Media, Berlin; New York,.

Moses, A., 1968. Analytical Chemistry Of The Actinide Elements. Oxford, New York: Pergamon Press.

Rost, F., 1995. Fluorescence Microscopy. Cambridge: Cambridge University Press.

Science Learning Hub. 2013. *Soil Properties*. [online] Available at:

<https://www.sciencelearn.org.nz/resources/957-soil-properties> [Accessed 30 August 2020].

Tan, X., Liu, F., Hu, L., Reed, A., Furukawa, Y. and Zhang, G., 2017. Evaluation of the particle sizes of four clay minerals. *Applied Clay Science*, **135**, pp.313-324